Encode

R.M. Colijn

Encode

Improving reaction wheel performance using a capacitive sensing encoder

by

R.M. Colijn

to obtain the degree of Master of Science
at the Delft University of Technology,
to be defended publicly on Monday May 23, 2022 at 13:00.

An electronic version of this thesis is available at `http://repository.tudelft.nl/`.

TUDelft

Preface

Before you lies the MSc thesis: "Encode: Improving reaction wheel performance using a capacitive sensing encoder", which is the result of two years of work during one of the strangest periods in recent times. It was written to fulfill the requirements for obtaining a MSc in Aerospace Engineering from the faculty of Aerospace Engineering at the Delft University of Technology. The period in which this thesis was written was from March 2020 until May 2022.

The project was undertaken at the request of Hyperion Technologies, where I have worked both as an intern and eventually as a full-time employee during the execution of this graduation. The challenge of combining a full-time job, a global pandemic and this research has been a tough one, however I am proud of the work I have done and am happy that I was able to see the project through beginning-to-end, developing an actually functioning prototype which can be taken as the starting point for a fully integrated design.

I would like to thank my supervisor Stefano Speretta for having an incredible amount of patience with me, helping me whenever I got stuck and always being positive and providing a path forwards. Second I would like to thank Bert and Steven from Hyperion Technologies to not only give me the opportunity to do my research with them, but also gain experience working as a full-time Design Engineer in the space industry. We have gone through some difficult times together, but the atmosphere in the office or on Zoom has always been great and I wouldn't have been able to do it without their continuous support, clever insights and motivational pushes every now and then.

I would like to highlight in particular my parents and two grandmothers, oma Almere and oma Stella for supporting me throughout my entire bachelor and master programs. Without them I would not have been able to afford myself the luxury of 'peeking over the fence' every now and then, pursuing other interests, partaking in Formula Student and getting the most out of my time in Delft. These experiences have greatly enriched my time as a student and I would not have wanted it any other way. Finally, without them asking me at every occasion 'When will you finally graduate?' I believe it would have probably taken even longer.

I hope that you will enjoy reading this thesis.

R.M. Colijn
Delft, May 2022

iii

Abstract

Cubesats, a colloquial term for small satellites approximately the size of a milk carton have become popular over the past 20 years as a cost-effective method of putting a payload into space. With the maturization of the market, the requirements for finer control over the satellite attitude drives the development of higher performance Attitude Determination and Control Systems.

Attitude Determination and Control Systems consist of sensors such as: sun sensors, startrackers, gyroscopes, and actuators such as: magnetorquers, reaction wheels and thrusters. The performance of an these systems is limited on both the sensing and actuation side and both need to function together to accurately point the satellite. To improve over-all ADCS performance, each individual component must be improved, which this research contributes to through improving the state estimation of the RW400 series of reaction wheels.

Brushless DC motors are a reliable option for reaction wheels. They make use of a separate rotor and stator where the stator magnetic field is continuously rotated whilst the rotor attempts to chase it, causing rotation. Brushless motors utilise a separate controller to rotate the stator field, as opposed to physical brushes. This external controller observes the rotor position and appropriately rotates the stator field such that the rotor will spin.
There are various control methods to rotate the stator magnetic field and the method selected affects the performance of the reaction wheels. Hyperion has noted two main performance limitations with their reaction wheels: a ripple on the output torque and poor control at low velocities. Both of these limitations can be mitigated through improved control methods, which require more accurate knowledge of the rotor position, also known as state estimation.

This MSc thesis presents the design of a capacitive sensing encoder which will improve the state estimation of the reaction wheels and thus will allow for the reaction wheel controller to be improved, improving reaction wheel performance. A prototype of this encoder was built and performance was evaluated through measurements. The encoder performance was measured and has an accuracy of $0.101°(1\sigma)$, which is a 300x improvement over the method of state estimation currently used by the Hyperion Technologies reaction wheels.

Contents

List of Figures

List of Tables

List of Symbols

A	Area
A_{amp}	Amplifier gain
A_{ac}	Amplitude of ac coupled signal
B	Bandwidth
C	Capacitance
d	Distance
δ_{elec}	Rotor-Stator PCB spacing (electrode spacing)
κ	Relative permittivity
ε	Permittivity
ε_0	Permittivity of vacuum
κ_{air}	Relative permittivity of air
κ_{FR4}	Relative permittivity of FR4
$f_{carrier}$	Carrier frequency/ Excitation frequency
g	Command torque
I	Current
i_q	Quadtrature current
i_d	Direct current
N	Number of repetitions (of a pattern)
N_{poles}	Number of poles in electric motor
N_{phases}	Number of phases in electric motor
ω_{rw}	Reaction wheel speed
ϕ_R	Phase angle
φ_δ	Magnetic flux
$\vec{P}$	Point P (x,y)
$\vec{P}_n$	Point P (x,y) value n (index in array)
φ_{abs}	Absolute collection electrode separation angle
φ_{inc}	Incremental collection electrode separation angle
R	Resistance
R_n	Radial value n (index in array)
R_{nom}	Nominal radius
R_{REL}	Relative component radius
R_{ABS}	Absolute component radius
$\vec{R}_{outer}$	Outer radius array
$\vec{R}_{inner}$	Inner radius array
S_{ac}	AC coupled signal
S_{dc}	DC coupled signal
S_q	Quadrature signal (real component)
S_i	Quadrature signal (imaginary component)
σ	Standard deviation
T_{cogg}	Cogging torque
T_R	Commutation torque ripple
$t_{PCB,rotor}$	Rotor PCB thickness
$\vec{\theta}$	Angles from 0 to 2π
θ_r	Rotor position
V	Voltage
w	Pattern width
$w_{t,min}$	Minimum thickness
W_{REL}	Relative component width
W_{ABS}	Absolute component width

Acronyms

AC   Alternating Current
ADC   Analog to Digital Converter
ADCS   Attitude Determination and Control System
AM   Amplitude Modulation

BLAC   Brushless AC
BLDC   Brushless DC

DC   Direct Current
DDS   Direct Digital Synthesis

ECSS   European Cooperation for Space Standardization

IC   Integrated Circuit

LED   Light Emitting Diode
LUT   Look-Up Table

NIA   Non-Inverting Amplifier

PCB   Printed Circuit Board
PMSM   Permanent Magnet Synchronous Motor
PSU   Power Supply

RMS   Root-Mean-Square

SNR   Signal-to-Noise Ratio
SPDT   Single Pole Double Throw
STD   Standard Deviation

TIA   Trans-Impedance Amplifier

1

Introduction

Cubesats, a colloquial term for small satellites approximately the size of a milk carton have become popular over the past 20 years as a cost-effective method of putting a payload into space. As of August 2021 approximately 1600 cubesats have been launched, belonging to 76 different countries in the world[24]. Hyperion Technologies, now part of AAC Clyde Space is a player in the global small-sat market, providing everything from gyroscopes to fully fledged Attitude Determination and Control Systems. With the maturization of both the cubesat and cubesat payload markets the requirements for finer control over the satellite attitude drive the development of higher performance Attitude Determination and Control Systems.

The Attitude Determination and Control System (ADCS) is one of the core systems of any satellite. It allows the satellite to orient itself, performing manoeuvrers such as payload-tracking, sun-tracking and orbit maintenance. Without an ADCS a satellite would not be able to perform any tasks other than transmitting omni-directional radio signals. Performance of these systems is driven by new payload developments, such as for example laser-communication terminals, which are also being developed at Hyperion Technologies.

Attitude Determination and Control subsystems, as the name implies have two main functions. Attitude Determination, through the use of sun sensors, startrackers, gyroscopes and magnetometers, and Attitude Control, through actuators such as reaction wheels, magnetorquers and thrusters.

The performance of an ADCS is limited on both the sensing and actuation side and both need to function together to accurately point the satellite in a desired direction. In order to improve the performance of Hyperion ADCS systems, each individual component must be improved, which this research will contribute to through improving the state estimation of the RW400 and RW200 series of reaction wheels.

This chapter will elaborate how reaction wheel performance can be characterised, highlight two main influences on performance of the RW400 reaction wheels, followed up by a main research question with five sub-questions.

Chapter 2 will provide a background on electric motors, which will analyse the performance of reaction wheels from the perspective of the electric motor. This will explain what state estimation is, how it affects reaction wheel performance and how it can be improved.

Chapter 3 will present a set of requirements provided by Hyperion Technologies, followed by a trade-off between various sensor feedback methods.

Chapter 4 will present the design of a capacitive sensing amplifier specifically designed to be used in RW400 class cubesat reaction wheels. This design is then realised through the development of a prototype in Chapter 5. This prototype is used to verify whether the requirements specified in Chapter

3 are met. The result of this verification can be seen in Chapter 6.

Finally, the report is concluded in Chapter 7 and some recommendations are made and potential future work is highlighted.

1.1. Performance of CubeSat Reaction Wheels

There are many ways to quantify the performance of an attitude determination and control system, depending on the mission-specific requirements some are more important than others. The current problems found with the range of Hyperion reaction wheels compound themselves in the pointing precision of the ADCS, which specifies how precisely the ADCS can point at a target. Due to the fact that cubesats are small and have low inertia, small perturbations in the control actuators of the ADCS will directly affect the spacecraft pointing precision. Hyperion Technologies has indicated two problems with their current offering of reaction wheels that influence the performance of their ADCS. These two problems are:

1. There is a ripple on the output torque produced by the reaction wheel.
2. The reaction wheel is unable to operate properly at near-zero velocities

This section will describe the principles behind both effects and elaborate how they affect reaction wheel performance.

1.1.1. Commutation Torque Ripple

Commutation torque ripple in brushless motors is a well documented topic and is a major contributor to vibrations in small reaction wheels. Torque ripple can occur due to inaccurate control, non-smooth transient curves when commutating, cogging torque, discontinuities caused by dead-zone insertion and variations in Lorentz force due to non-constant magnetic flux densities[34][41].

The amplitude of commutation torque ripple is directly proportional to the torque commanded to the reaction wheel through equation (1.1). Where T_R is the commutation torque ripple, C_R the commutation torque ripple coefficient, g the commanded torque and ϕ_R an arbitrary phase angle. Due to the fact that commutation torque ripple is directly related to command torque, it's contribution is largest during manoeuvres and minimal during inertial pointing [4]. The European Cooperation for Space Standardization (ECSS) specifies that the torque ripple is typically 14.3% of the peak-to-peak nominal motor torque.[16]

$$T_R = C_R g sin(N_{poles}N_{phases}\omega_r w + \phi_R) \qquad (1.1)$$

Figure 1.1 plots the z-axis torque disturbances measured on the RW400 reaction wheel during a constant acceleration ramp. This wheel has two pole pairs, thus $N_{poles} = 4$ and uses a three-phase motor. This means that the frequency at which the torque ripple occurs is 12 times higher than the rotational velocity. From this it can be concluded that the relatively flat white line represents the commutation torque ripple, the others mostly represent different modes of bearing vibrations [17].
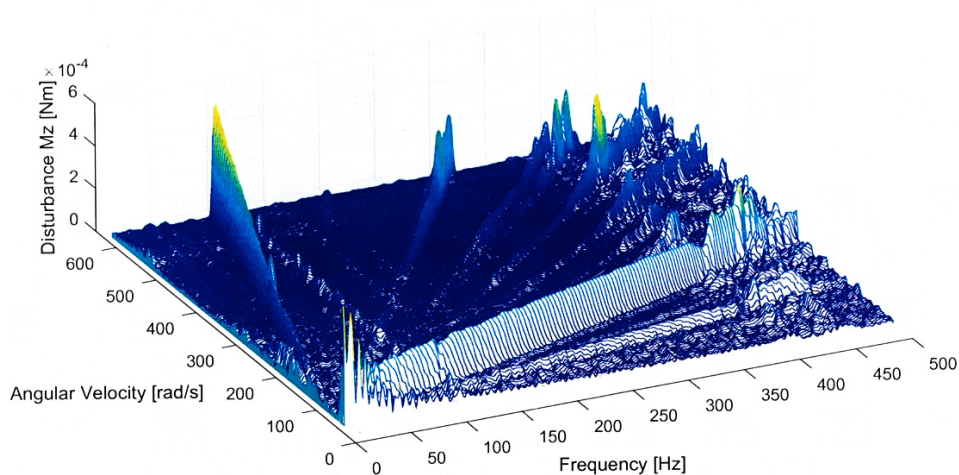
Figure 1.1: Measured z-axis vibrations the RW400 reaction wheel [17]

Due to the fact that there are vibrations in the reaction wheel, the pointing precision of the ADCS is affected.

1.1.2. Low-Velocity Operation

When operating, a reaction wheel controller requires knowledge of the current rotor position. Without this knowledge the controller does not know which one of the Brushless DC (BLDC) phases to actuate in order to make the wheel spin. Figure 1.2 highlights the torque box (maximum available reaction wheel torque at a given wheel velocity/momentum) for the 10 mNms reaction wheel sold by Sinclair Interplanetary[37]. From this torque box one can deduce that at low velocities (low momentum) the controller is unable to accurately control the output torque of the reaction wheel.
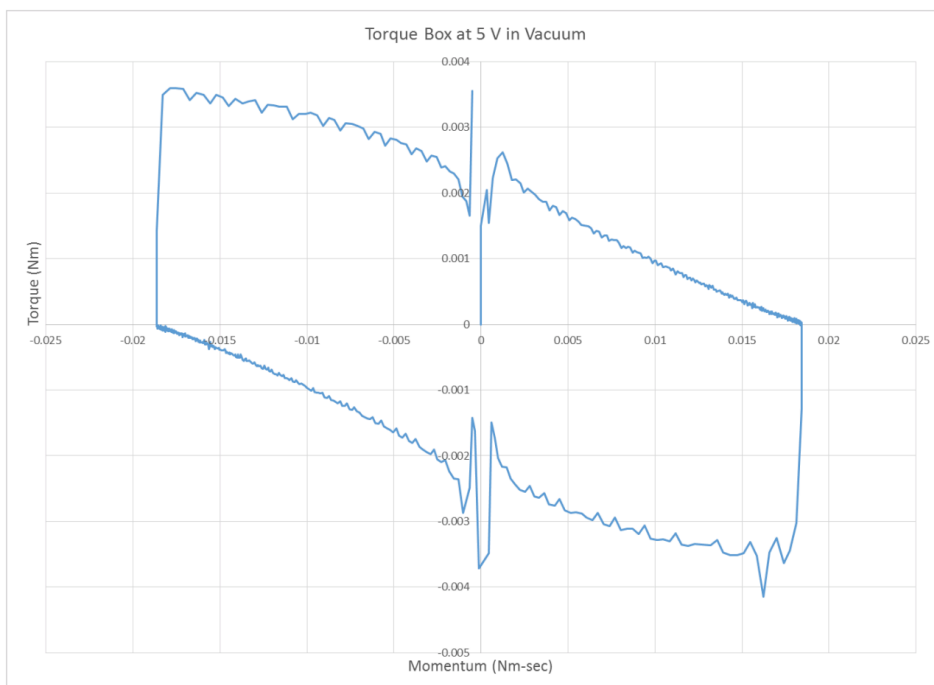
Figure 1.2: Torque Box of the 10 mNms reaction wheel [37]

The inability to provide accurate output torque at low speeds is caused by a lack of information. At low speeds the hall-effect sensors utilised in these motors simply do not update the controller often enough

on the wheel position, meaning that extrapolation of previous data is required to keep this information up to date. The lower the velocity becomes, the less accurate this extrapolation becomes due to varying bearing friction coefficients, timing errors and noisy measurements. Feedback through sensored methods can solve this issue by providing constant, accurate position feedback, independent of rotor speed.

Traditionally this problem is circumvented by not operating reaction wheels near zero rpm. However recent clients of Hyperion Technologies have requested such an operational mode to be possible, further coupled by the fact that when low rpm operation is possible the momentum envelope effectively doubles in size, because the wheel can go from +5000 rpm to -5000 rpm without issue, which is currently not possible.

1.2. Research Objective & Questions

The introduction to the problem given in the previous section justifies the work to be performed in this research. There are two highlighted issues with the reaction wheels, which this research will try to provide a solution for. This work will present a common source for these issues (poor state estimation) and provide a solution in the form of sensored feedback. Why this common source exists and why sensored feedback is a solution will be elaborated upon in Chapter 2. In order to define this research a main research question is proposed:

>   **MQ**: How can reaction wheel state estimation be improved in order to improve reaction wheel performance?

In order to answer this research question, five sub-questions are defined:

RQ1 Can improving the state estimation improve the performance of the reaction wheel?

RQ2 Does sensor feedback improve reaction wheel state estimation?

RQ3 What type of sensor feedback can be implemented within the constraints of a CubeSat reaction wheel?

RQ4 What would a design of sensor feedback on the reaction wheel entail?

RQ5 What is the resulting improvement of state estimation?

Answering these research questions will occur throughout the rest of this work.Chapter 2 will provide background information on the operating principles of reaction wheels and electric motors in order to provide answers to research questions **RQ1** and **RQ2**.

Chapter 3 will provide the requirements of the sensor feedback as requested by Hyperion Technologies and with these requirements a trade-off is made between the various sensored feedback methods, answering question **RQ3**.

Chapter 4 will elaborate upon the design cycle of the sensor feedback and show the final design, answering **RQ4**.

Finally, Chapter 6 will verify the output of the design and determine the improvement of the reaction wheel state estimation and answer **RQ5**.

2

Electric Motors

Electric motors date back to the 1740s[27]. Contrary to internal combustion engines, electric motors do not use fuel, but rather use electrical energy to produce rotational energy. This chapter will cover the topic of electric motors. The general working principle is explained, the concepts of state estimation and actuation are covered and finally, two research questions are answered.

2.1. Working principle of electric motors

When treating the subject of electric motors one can distinguish between two types of motors, AC (alternating current) motors, requiring alternating current to run and DC (direct current) motors, running on direct current. On Earth alternating current motors are common and are used in products such as compressors, pumps, conveyor systems and lifting gear. This is due to the fact that AC power is readily available and these motors are rugged [14]. In space however DC power is more readily available because batteries naturally produce direct current and all other spacecraft components such as micro-controllers, sensors etc. also use DC power. Thus for reaction wheels DC motors are the dominant kind.
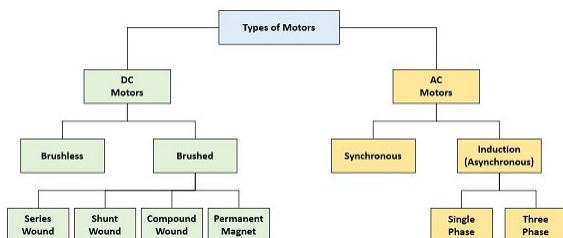
Figure 2.1: Different types of Electrical Motors [14]
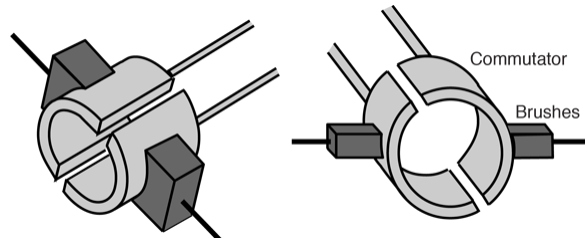
Figure 2.2: Brushed DC Motor Commutation [33]

The left branch of Figure 2.1 shows the types of DC motors that are available. In general two types are distinguished, brushed and brushless. In brushed DC motors the commutation (generation of alternating currents through the armature coils) is achieved through mechanical brushes that alternate the conducting path between terminals. These brushes touch positive and negative terminals of the commutator in an alternating fashion, keeping the rotation going.(Figure 2.2) The fact that these brushes slip over the surface of the commutator causes mechanical wear and is thus not a long-term solution.

Brushless motors alleviate this issue by not having brushes that can wear out, resulting in a longer lifespan, making them ideal for applications such as reaction wheels. For brushless DC motors there is no physical commutator and current commutation is achieved by a controller. Figure 2.3 shows the internal workings of a brushless DC motor. The rotor contains permanent magnets and its field has a certain direction. The stator consists of coils that generate magnetic fields based on currents flowing

through them. The controller will continuously alternate the stator field between the coils shown. The rotor will chase this stator field and thus the motor starts rotating.
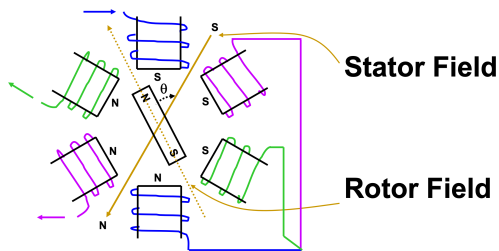
Figure 2.3: Brushless DC Motor Operation [28]
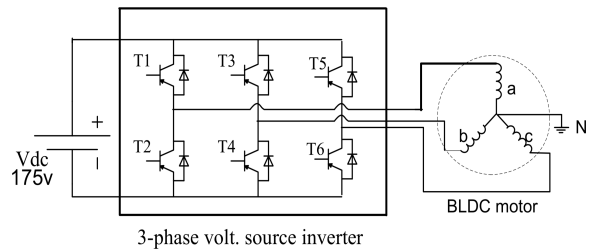
Figure 2.4: Brushless DC Motor Schematic & Controller [32]

There are many possible topologies for a brushless DC motor controller. The most commonly used one makes use of three half-bridges, seen in Figure 2.4. The stator phase currents are controlled by triggering the inverter switches $T_1 - T_6$ sequentially[32]. Due to the fact that there are three stator phases in a brushless DC motor there are six total commutation modes. These can be found in Table 2.1. By rotating through these six modes the magnetic field is spun.

θ	T1	T2	T3	T4	T5	T6	Active Phases
$0 - 60°$	C	-	-	C	-	-	ab
$60 - 120°$	C	-	-	-	-	C	ac
$120 - 180°$	-	-	C	-	-	C	bc
$180 - 240°$	-	C	C	-	-	-	ba
$240 - 300°$	-	C	-	-	C	-	ca
$300 - 360°$	-	-	-	C	C	-	cb

Table 2.1: Block Commutation logic for a three phase diode bridge inverter (C = Conducting, - = closed)

The timing of this commutation sequence and its exact implementation will be elaborated upon in Sections 2.2 and 2.3.

2.2. State Estimation in Electric Motors

The commutation of the currents in a brushless DC motor is based on the current state (angular position) of the rotor. Due to the requirement of knowing the rotor position the topic of state estimation is broad and many published works attempt to develop better methods. In general one can divide state estimation into two categories. *Sensored* and *Sensorless*.

2.2.1. Sensorless State Estimation

Sensorless control strategies are very sought after due to the fact that they greatly reduce design complexity. Sensorless control strategies perform rotor state estimation based on the back electromotive forces (or back-emf)[18]. In star-wound motors the back-emf is sensed in the currently non-conducting phase. (see Table 2.1) Methods for detecting this back-emf signal can be separated into several categories [18].

- **Direct back-emf detection methods**

    - Back-EMF Zero Crossing Detection/ Terminal Voltage Sensing
    - PWM Strategies

- **Indirect back-emf detection methods**

    - Back-EMF Integration
    - Third Harmonic Voltage Integration
    - Free-wheeling diode conduction/ Terminal Current Sensing

Throughout the years many researchers have made attempts at improving these estimation methods. For example using flux linkage based algorithms [32] or signal injection at lower speeds [45]. Whilst the results of these developments is promising, there is still a large ripple in the output torque and at low speeds there is not sufficient information available to make proper estimates of the rotor position at any time.

2.2.2. Sensored State Estimation

Opposed to sensorless methods, sensored methods utilise separate sensors to measure the rotor position, which has the downside of added complexity, but the upside of getting much finer knowledge of the rotor position. Two types of sensors are generally used, encoders and hall-effect sensors.

2.3. Actuation of Electric Motors

When positional knowledge of the rotor is available, either through sensored or sensorless methods, the next step is to commutate the current between the coils in the motor. Three methods of current commutation will be treated in this section: block commutation, sinusoidal commutation and Field Oriented Control.

2.3.1. Block Commutation

Block commutation is the simplest form of commutation and was described in Table 2.1. The advantage to this method is the simplicity. Switches simply need to be opened or closed to drive the motor. For this reason brushless *DC* motors were developed with a trapezoidal back-emf shape. (will be elaborated upon in Section 2.4) The ideal switching mode for these types of motors is with square block waves. Figure 2.5 shows the perfect block commutation scheme for a typical BLDC motor.
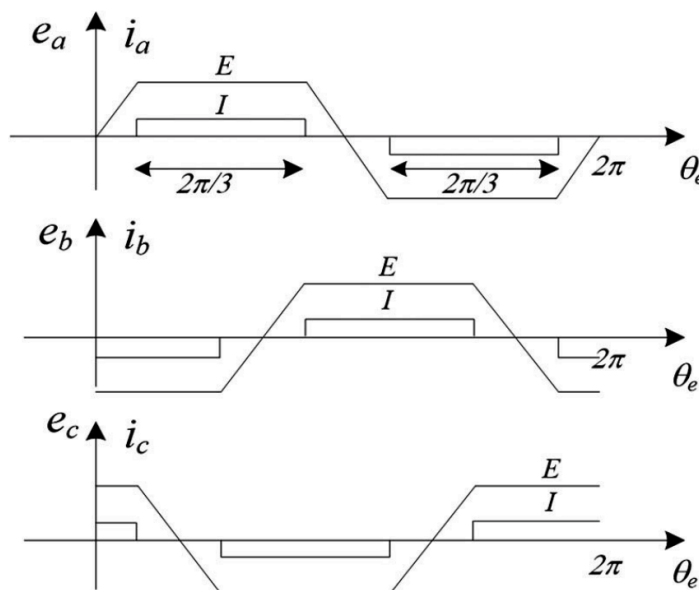
Figure 2.5: Block Commutation and Trapezoidal Back-EMF[5]

In reality the phase inductance of the stator coils slow down the rise and fall of the phase currents, meaning a perfect square wave is not possible, introducing imperfections in the output torque of the motor.

2.3.2. Sinusoidal Commutation

Given that the back-emf shape of some motors is sinusoidal it is beneficial to develop a method of controlling the phase current in a sinusoidal manner. This is not only beneficial for pure sinusoidal motors. Some trapezoidal motors are only trapezoidal on paper, in reality their emf shape is much more sinusoidal. Particularly at higher speeds the difference between the two types of back-emf becomes smaller. Bertoluzzo [5] demonstrated that it is possible to reduce the torque ripple in trapezoid-ally shaped motors by utilising a sinusoidal controller.

Sinusoidal drive is generated by utilising a microcontroller that is capable of generating PWM signals. These signals can then be input into the H-bridge shown in Figure 2.4, allowing for more complex signals to be created. One example involves the utilisation of a look-up table for a very simplified sinusoidal control algorithm [3]. Figure 2.6 demonstrates how sinusoidal commutation can be applied to a BLDC motor.
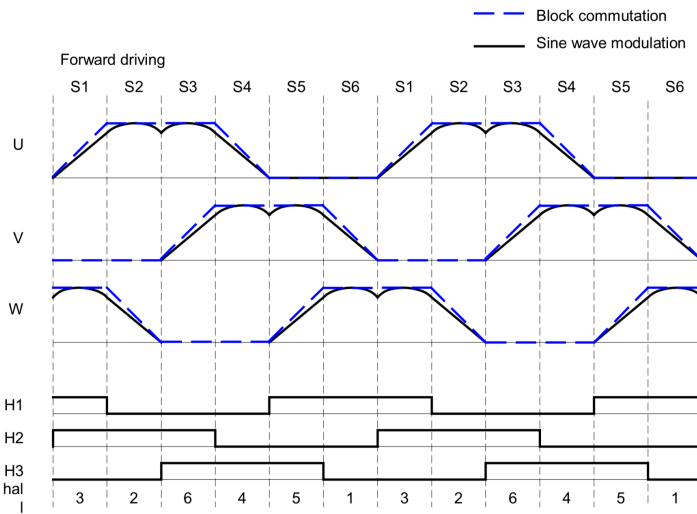
Figure 2.6: Sinusoidal Commutation[3]

2.3.3. Field Oriented Control

The output of field oriented control is, similarly to sinusoidal control a sinusoidally shaped control signal. The method of generating these signals however is very different. Controlling the sinusoidal shape is typically done by a PI controller. These controllers have limited gain and frequency response, which causes the control to break down at higher rotation speeds [10].

In order to solve this problem Field Oriented Control uses smart transformations (Clarke and Park) to modify the parameter being controlled by the PI controller to one that is time invariant and much more stable. This makes it simpler to control the motor at higher speeds[10].

Field Oriented control works under the assumption that the motor is a balanced system, meaning $i_a + i_b + i_c = 0$, which is true for the motor seen in Figure 2.4. By first utilising the **simplified Clarke transformation**, seen in equation (2.1), the three-phase system is transformed into a two-phase system in the $[\alpha, \beta]$ reference frame, which is attached to the stationary stator. (Figure 2.8)

$$\begin{bmatrix} i_\alpha \\ i_\beta \end{bmatrix} = \frac{2}{3} \begin{bmatrix} 1 & -\frac{1}{2} & -\frac{1}{2} \\ 0 & \frac{\sqrt{3}}{2} & -\frac{\sqrt{3}}{2} \end{bmatrix} \begin{bmatrix} i_a \\ i_b \\ i_c \end{bmatrix} \tag{2.1}$$
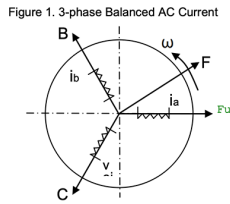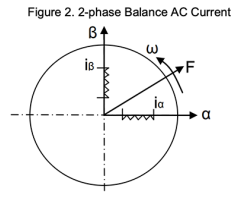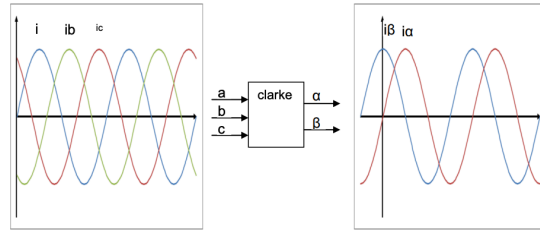
Figure 2.7: Clarke Transformation[11]   Figure 2.8: Clarke Transformation[11]

The Clarke transformation has simplified the equation from a 3-phase system to a 2-phase system. By applying a fictitious AC signal to this two-axis system and performing the inverse Clarke transform one will obtain the currents through the stators to get the motor running. This however still requires an AC current to be controlled, suffering from the problems highlighted earlier. That is why the **Park transform** is utilised to convert the system into a rotating reference frame attached to the *rotor*[11].

The Park Transform can be seen in equation (2.2). This transformation is dependent on the current rotor position θ. Figure 2.10 demonstrates the Park transformation. The phases I_d and I_q have become constant DC currents. This means that these are much simpler to control than the highly time variant AC signals.

$$\begin{bmatrix} i_d \\ i_q \end{bmatrix} = \begin{bmatrix} cos\theta & sin\theta \\ -sin\theta & cos\theta \end{bmatrix} \begin{bmatrix} i_\alpha \\ i_\beta \end{bmatrix} \tag{2.2}$$
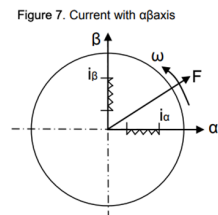
Figure 2.9: Park Transformation[11]   Figure 2.10: Park Transformation[11]
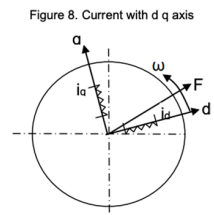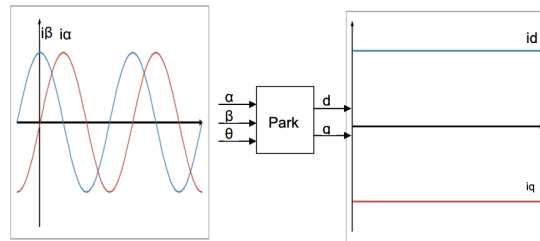
The *Quadrature Current i_q* controls the amount of torque generated by the motor and is typically optimised to maximize efficiency and performance of the motor. The *Direct Current i_d* is oriented perpendicular to the quadrature axis and is the current that does not contribute to torque. By utilising a PI controller to control the quadrature and direct currents it is possible to control a BLDC or Brushless AC (BLAC) motor with higher efficiency and at higher speeds. The trade-off is that detailed information of the rotor position θ is required, which is not true for for example block commutation.

2.4. RQ1: Can improving the state estimation improve the performance of the reaction wheel?

In Chapter 1 two main topics were covered which were to be improved in order to improve the reaction wheel performance: *commutation torque ripple* and *low-velocity operation*. This section will elaborate why improved state estimation will affect both topics and how they will be improved.

Firstly, low-velocity control will be improved greatly due to the fact that the controller currently has very poor state estimation at low speeds. The hall-effect sensors only update the rotor position every 30 degrees, meaning at low velocities the state estimator has to do a lot of interpolation to 'guess' the current rotor position. By improving the reaction wheel state estimation a more complex driving scheme can be implemented, even at lower velocities.

Second, torque ripple will be reduced by improving the control scheme of the reaction wheels, which requires better state estimation. This is elaborated below.

The following sources of torque ripple in BLDC motor drives can be distinguished:[41]

1. Cogging torque

2. Phase current vs back-EMF waveform mismatch

3. Dead-time insertion

4. Commutation of phase currents

Each of these will be briefly covered in this section in order to answer why state estimation could reduce commutation torque ripple.

Cogging Torque

Cogging torque describes the variation in output torque of a BLDC motor due to a change in magnetic conductivity due to stator teeth or poles. The cogging torque can be mathematically determined using Equation (2.3) [41]. In this equation φ_δ represents the magnetic flux crossing the airgap and R is the total reluctance through which it passes, finally θ_r is the rotor position.

$$T_{cogg} = -\frac{1}{2}\varphi_\delta^2 \frac{dR}{d\theta_r} \tag{2.3}$$

Due to the fact that the Hyperion Technologies reaction wheels (purposely) do not use a ferromagnetic stator material $\frac{dR}{d\theta_r}$ will be very small, as such cogging torque will not be further considered.

Phase Current vs Back-EMF Mismatch

In order to maximise efficiency and minimise torque ripple the shape of the currents passing through the armatures of an electric motor must match the shape of its back-emf [43]. The back-emf is generated by the induced current in the armature coils. (due to the spinning rotor) This voltage opposes the driving voltage and thus lower the efficiency and torque output of the motor. If the controller signal and back-emf shapes are mismatched the *net* (induced by controller - induced by back-emf) will fluctuate and so will the output torque of the motor, which ripples the output.

The back-emf shape can be either sinusoidal or trapezoidal, depending on the air grap flux distribution between the permanent magnet and the coils[36]. This difference is caused by either concentrated winding or distributed windings on the stator. The difference in shape can be seen in figure 2.11. Sinusoidal back-emf motors are also often referred to as BLAC or Permanent Magnet Synchronous Motor (PMSM) motors. Nomenclature however, has become confusing over the years due to different manufacturers using different labels.

Figure 2.12 shows the torque ripple that can occur due to a mismatch in the control strategy. From it it can be deduced that PMSM/BLAC motors should be controlled sinusoidally and BLDC motors using
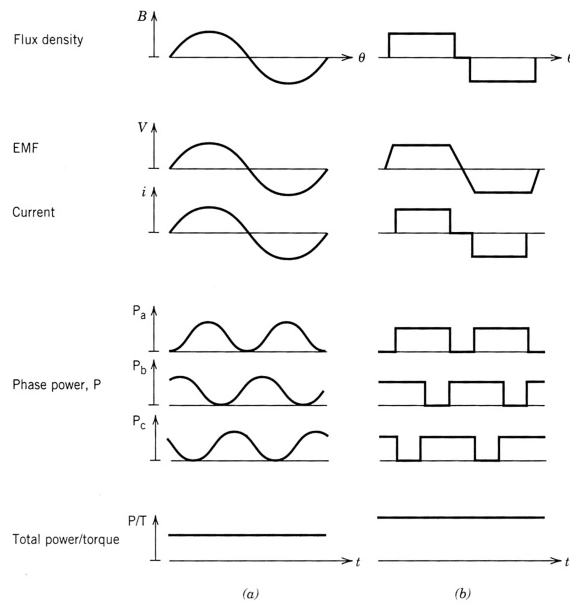
Figure 2.11: Idealised waveforms in BLDC motors. (a) Sinusoidal (b) Trapezoidal [36]

block commutation. Contrary to this, Sumega[41] highlights that the back-EMF shape for motors that are sold as 'BLDC' is very similar to that of a sinusoidal motor with additional harmonics. The back-EMF is in no way perfectly trapezoidal as theoretical models would suggest. Due to this fact it *can* be beneficial to utilise sinusoidal controllers for BLDC motors, such as demonstrated by Bertoluzzo [5].
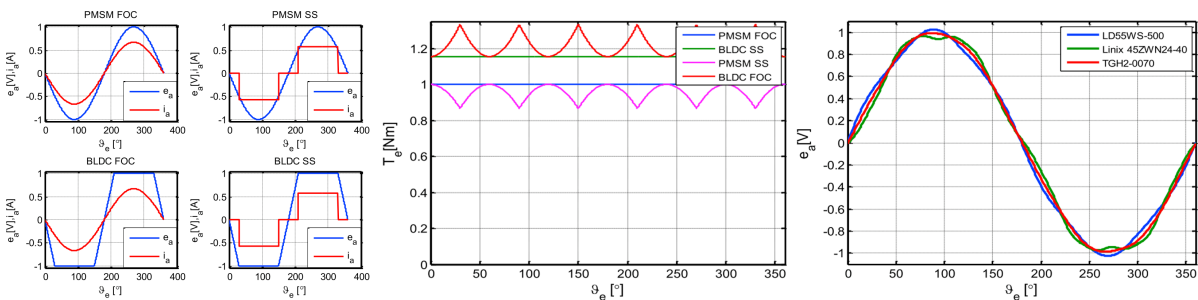
Figure 2.12: Torque Ripple due to Waveform mismatch (left,center) & Back-EMF shape of BLDC motors (LD55WS-500 & Linix 45ZWN24-40) vs PMSM/BLAC (TGH2-0070) (right) [41]

Simulations show that a waveform mismatch can have an impact of 10-20% on the output torque (see Figure 2.12), meaning it is a very large contributor to torque ripple. Shape matching of the control wave to the back-emf thus seems to have a potential of improving reaction wheel performance. It should be noted that this is under zero-load conditions. In reaction wheels there will be a load (heavy rotor) with high inertia attached to the wheel that is capable of smoothing out these vibrations. Phuoc does not even consider the ripple on the 5kg W18 wheels sold by Bradford.[34] These can be neglected because comparatively the amplitude of torque ripple on these large wheels is much lower than the amplitude of other vibrations.

In order to properly match the shape of the input signal to the back-emf shape, sufficient information on the current rotor position is required. Currently the Hyperion Technologies reaction wheels only make use of hall-effect sensors, meaning that the position of the reaction wheels is only updated every 30°, which is sufficient for a simple switching scheme like seen in Table 2.1, but generally insufficient to implement other control schemes. Furthermore, Hyperion Technologies reaction wheels make use of PMSM motors, but currently utilise a block-commutation scheme due to the lack of positional feedback. This mismatch can be solved through the implementation of improved state estimation.

Dead-Time Insertion

In order to protect the controller in Figure 2.4 against a state where both transistors in one branch short-circuit, dead-time is inserted between commutation cycles. This causes discontinuities in the driving signal, and as such causes torque ripple. Due to the fact that dead-time is inherent to the system and cannot be simply removed, this will not be considered further.

Commutation of Phase Current

Finally, the commutation of phase currents can cause ripples on the output current. This problem is most prevalent in block-commutation schemes where the control signal switches immediately but the current lags behind due to actual inductances of the phase coils. At low speeds the lack of back-emf means the current is slow to 'rush out' of the phase causing the end (falling edge) of a conduction interval to become distorted. At high speeds the back-emf is very high and gives the controller great difficulty of injecting a current at the beginning (rising edge) of the conduction interval [5].

Conclusion

Concluding, improving state estimation on the RW400 reaction wheel will allow for lower-velocity operation due to the increased positional awareness of the rotor. Furthermore, for the four sources of torque ripple the following statements can be made:

1. **Cogging torque**
   This problem is already solved in Hyperion reaction wheels by not utilising a ferrous material for the motor core.
2. **Phase current vs back-EMF waveform mismatch** This source of noise is great in the Hyperion wheels due to the fact that the wrong switching scheme is utilised with lacking positional sensing.
3. **Dead-time insertion**
   This problem cannot be overcome and is an inherent limit of real systems.
4. **Commutation of phase currents**
   Similar to dead-time insertion, this is simply a fact of nature and cannot be solved.

Based on these four statements one can conclude that Hyperion Technologies already takes steps to minimise the torque ripple through removing cogging torque, however the mismatch between the phase currents and back-emf waveforms is still present. Without improving the state estimation it is difficult to incorporate a more advanced controller, (particularly at lower velocities), hence improving state estimation will yield improvements in reaction wheel performance.

2.5. RQ2: Does sensor feedback improve reaction wheel state estimation?

Section 2.2 highlighted two methods of state estimation: sensored and sensorless. Sensorless state estimation is greatly dependant on the magnitude of the back-emf of the reaction wheel, which scales with reaction wheel speed. This means that at lower speeds the Signal-to-Noise Ratio (SNR) of this back-emf signal will go down, making the measurements unreliable. Furthermore, the update rate of detecting the zero-crossings of the back-emf signal, similar to Hall-Effect sensors is dependant on reaction wheel velocity and thus unreliable at low velocities.

By implementing sensored feedback a constant update rate, of which the accuracy does not depend on reaction wheel velocity can be provided. Therefore, implementing sensor feedback, improves reaction wheel state estimation.

3

Sensor Feedback: Requirements & Selection

The purpose of this chapter is to answer the third research question:

What type of sensor feedback can be implemented within the constraints of a CubeSat reaction wheel?

Section 3.1 will elaborate upon the constraints provided by Hyperion Technologies in the form of five requirements, to which the reaction wheel sensor feedback must comply. Section 3.2 will elaborate upon three methods of sensor-feedback and a trade-off is made in Section 3.3 to select the type of sensor feedback that is suitable for implementation on the RW400 reaction wheel.

3.1. Requirements provided by Hyperion Technologies

In communication with Hyperion Technologies a series of requirements have been discovered and set for the reaction wheel encoder. The purpose of this section is to present these requirements and provide the reasoning behind them. An overview of the requiremenents is provided at the end of this section.

3.1.1. HT_ENC_01: Accuracy

The encoder shall have an accuracy that is greater than the control accuracy of the controller implemented by Hyperion Technologies. The controller has a 9-bit resolution with two electrical rotations per mechanical rotation, meaning the system has an effective required resolution of 10-bit. In reality, 10-bit Analog to Digital Converters (ADCs) often do not provide actual 10-bit accuracy due to non-linearities, quantisation noise etc. In order to account for these factors an engineering margin of 2-bit is added. This means that this requirement will be set to 12-bit (1 σ), which is $0.087°$.

3.1.2. HT_ENC_02: Update Frequency

The reaction wheel has a maximum rotational velocity of 5000 rpm, which is 83 Hz. In order for the encoder to remain useful throughout the entire operational range of the reaction wheel, its update rate must always stay above that of the Hall effect sensors. The Hall effect sensors update 12 times per mechanical rotation, meaning the update frequency of the encoder must be greater than or equal to 996 Hz.

3.1.3. HT_ENC_03: Output Signal

The reaction wheel encoder makes use of digital signals to provide output to the current reaction wheel controller.

3.1.4. HT_ENC_04: Power Cycle Tolerant

Due to the harsh space environment it is not unthinkable that the controller/encoder sensing components or power supply might suffer from an intermediate failure. Thus the encoder must be capable of recovering from a power cycle quickly without losing its position.

3.1.5. HT_ENC_05: Space Components

Not all electronic components are tolerant to the space environment. The exact behaviour depends on the technology, some components only occasionally fail, whilst others immediately stop functioning in space. In order to ensure that the encoder will function in the space environment, components that are known to have high failure rates and/or bad failure modes must be avoided.

3.1.6. Requirements Overview

HT_ENC_1 The reaction wheel encoder shall have an accuracy of 12-bit.

HT_ENC_2 The reaction wheel encoder shall have an update frequency of 996 Hz or greater.

HT_ENC_3 The signal output of the encoder shall be compatible with the reaction wheel controller.

HT_ENC_4 The reaction wheel encoder shall be tolerant to power cycles.

HT_ENC_5 The reaction wheel encoder shall not contain components that are known to fail in the space environment.

3.2. Sensor Feedback

Providing external sensor feedback to an electric motor can be done in two ways. The first is utilising Hall effect sensors to detect transitions of the rotor magnets. Currently, Hyperion Technologies already utilises such a feedback mechanism on the reaction wheels. In Section 2.4 it was argued that such a feedback mechanism is not sufficient for the RW400 reaction wheels due to the dependance on reaction wheel velocity.

The second method of providing reaction wheels with sensor feedback is through the use an encoder. Encoders function as fully separate devices from the electric motor. In general the distinction is made between absolute and relative encoders. Where absolute encoders are capable of providing the instantaneous position of the reaction wheel (e.g. 47°) compared to a reference point and incremental encoders are only capable of providing incremental updates (the wheel has moved 1°).

The working principle behind an encoder depends on the type of encoder that is selected. In general three types of encoders can be distinguished: Magnetic, Optical and Capacitive encoders. This section will provide a short overview of all three and perform a trade-off between them to select the type of encoder to be used on the Hyperion Technologies reaction wheel.

CAPACITIVE OPTICAL MAGNETIC
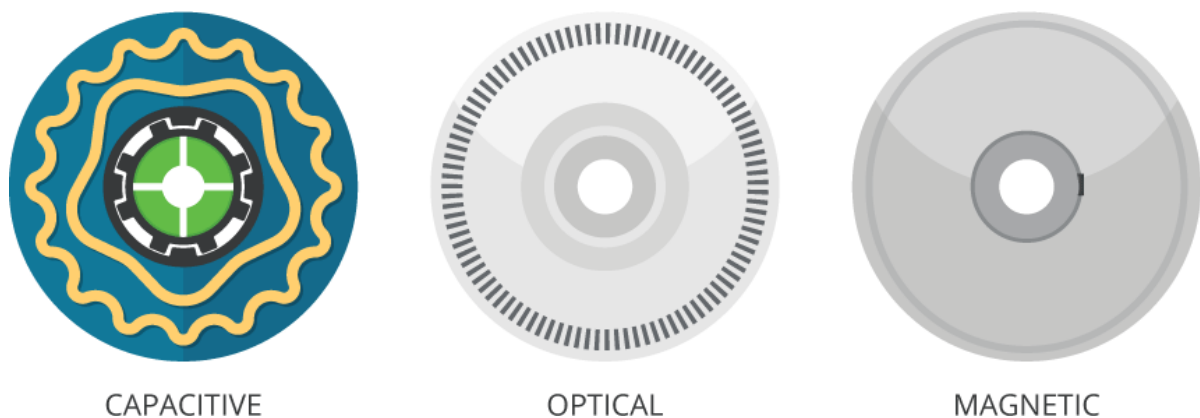
Figure 3.1: Reaction wheel encoder candidates[39]

3.2.1. Magnetic Encoders

Magnetic encoders utilise either hall-effect sensors or magneto resistive sensors to measure variations in the magnetic field. These variations are caused by an alternating evenly spaced north-south pole disk that spins along with the motor shaft. These types of sensors are often very robust because they are not subjective to contamination.[1] The simplest form of a magnetic encoder can be seen in Figure 3.2. Two hall-sensors are utilised so direction can be extracted from the output signals based on which of the two curves lags behind the other.[30]
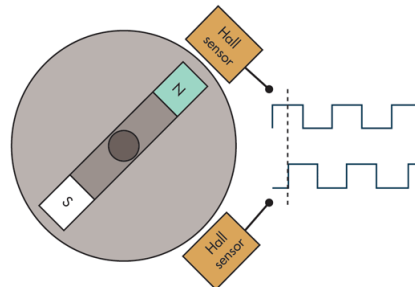
Figure 3.2: Magnetic Encoder Operating Principle [30]

If analog Hall-sensors were used it is theoretically possible to determine the absolute angular position in Figure 3.2 based on the output signal. However in practice the noise is much too great to do this. That is why digital outputs are more commonly used. In the setup visible there would be four different possible positions, giving an angular resolution of 90 °. By increasing the number of magnetic poles around the edge of the wheel the resolution will be increased.[30]

3.2.2. Optical Encoders

Optical encoders utilise a disk with a printed pattern and/or cut-out in combination with a light source. The light source shines on the disk and while the disk spins the output is registered.
The output of an incremental optical encoder is in the form of pulses. The working principle of this optical encoder can be seen in Figure 3.3. The light source shines onto a moving plate with slits in it. These slits are "compared" to a stationary plate with the same slits. By measuring the amount of light coming through on the other side of the two encoder disks one can generate a triangular signal. The peak of this triangular signal will occur when the two slits are exactly aligned. By placing a large amount of slits on an encoder wheel one can obtain small incremental step information. [15]
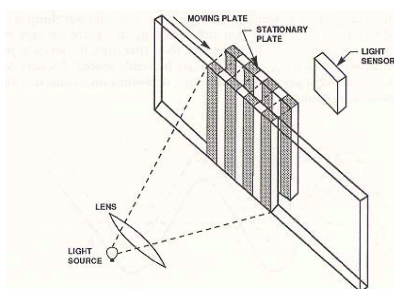
Figure 3.3: Basic Incremental Encoder [15]
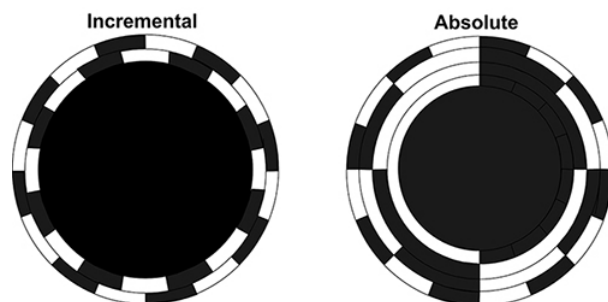
Figure 3.4: Encoder Discs[35]

Absolute optical encoders are more advanced than incremental encoders and make use of optical detectors registering a pattern on the encoder disc, such as Grey code. Figure 3.4 shows encoder discs for both incremental and absolute optical encoders. By reading the unique combination of bits for every position the encoder is capable of detecting the current orientation.

3.2.3. Capacitive Encoders

Capacitive encoders are a relatively new technology, offering resolution comparable to optical encoders and similar ruggedness to magnetic encoders. [9] Combining some of the positives from both magnetic

and optical encoders the capacitive encoder makes use of varying capacitance between plates to encode position. Figure 3.5 demonstrates the working principle of a capacitor [7]. The capacitor consists of two conductive plates with a dielictric material in the middle. The total capacitance between the plates is determined by Eq. (3.1).

$$C = \frac{\varepsilon A}{d}$$ (3.1)

In normal capacitors these factors are fixed beforehand, resulting in a capacitor of capacity C. However by varying A,ε or d depending on position positional information can be encoded. That is the principle upon which capacitive encoders are built.
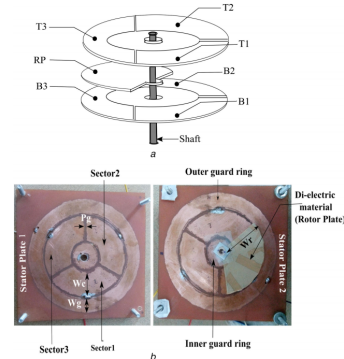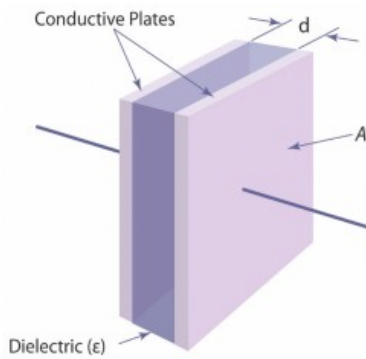
Figure 3.5: Capacitor working principle [7]   Figure 3.6: Simple Capacitive Encoder [12]

Using this method it is possible to construct both absolute and incremental encoders. Varying strategies can be applied for the design of such an encoder. Figure 3.6 demonstrates a relatively simple encoder based on the principle of varying ε. The dielectric material labelled as RP is spun around with the motor axis, whilst the other plates remain statically in place. This will vary the capacitances between $T1 - B1$, $T2 - B2$ and $T3 - B3$ from which the position of the rotor can be deduced.

Figure 3.7 demonstrates an encoder that makes use of varying A in order to vary the capacitance. It consists of four repeating pairs of transmitting electrodes (A, B, C and D). The reflecting electrode has a sinusoidal shape drawn upon it. By injecting four signals with a 90 degree phase shift into the four transmitters, by demodulating the resulting output signal on the receiving electrodes it is possible to see the position of the reflecting electrode and thus the rotor. This concept has been further refined in 2019 [20], making changes to the rotor wheel and changing the direction of the signal from four excitation signals reaching a common point to a common excitation point reaching four measurement points.
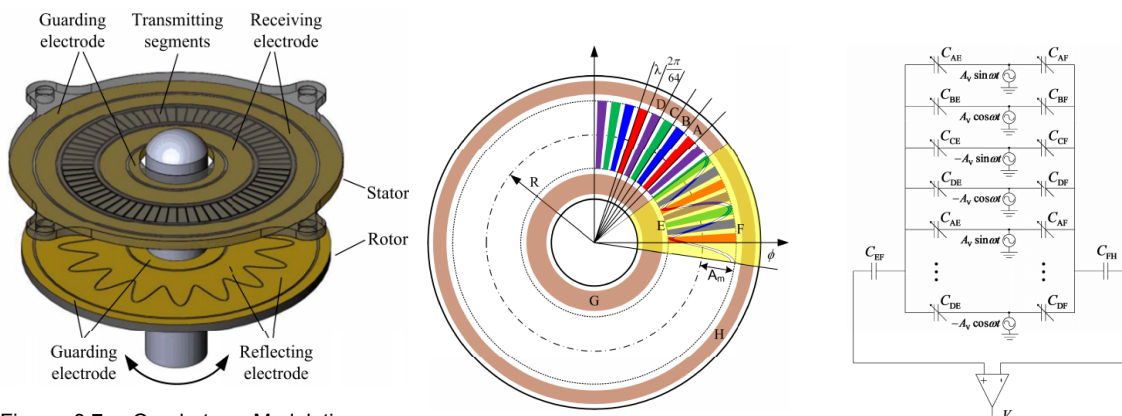
Figure 3.7: Quadrature Modulation Encoder[46]

3.3. Encoder Selection

Three candidates are identified as potential encoder types for the RW400: Magnetic, Optical and Capacitive encoding. The purpose of this section is to perform a trade-off between the three and select the type of encoder that will be used for the RW400. In order to perform this trade-off four criteria are defined based upon the requirements. (Section 3.1) Section 3.4 will perform the trade-off and conclude this chapter by answering the third research question.

Accuracy

Comparing the accuracy of the three encoder technologies at a higher level is difficult, given that with he right design all three can be made to be as accurate/inaccurate as possible. In general the optical encoder will be affected the least by EMI emitted from the motors, whilst magnetic encoders will be affected the most [39]. Capacitive encoders can achieve similar levels of performance as optical encoders [39].

Update Frequency

Due to the difference in operating modes of the three encoders a clear division can be created in regards to update frequency. The optical and magnetic encoders both depend on the rotational velocity of the rotor due to the fact that their patterns are incremental, meaning the output remains the same for short instances of time. The capacitive encoder does not suffer from this problem due to the fact that the output can be continuously sampled and the encoded pattern changes in a smooth manner.

Power Cycle Tolerance

Inherently the three technologies are all not power-cycle tolerant. However with the construction of an absolute component to the encoder it becomes possible to regain the rotor position even after losing the current position. For the capacitive and optical encoders this can be done through the implementation of an absolute pattern. The magnetic encoder however has a low magnetic immunity, making absolute measurements difficult. [39]

Space Environment Tolerance

Given the right component selection both the magnetic and capacitive encoders can be constructed to be tolerant to the space environment. The optical encoder however will face many challenges due to the requirements on a light source. The performance of Light Emitting Diodes (LEDs) in high-radiation environments is a well-documented subject and generally LEDs degrade heavily in space, making an optical encoder an unreliable option for the space environment [13].

3.4. RQ3: What type of sensor feedback can be implemented within the constraints of a CubeSat reaction wheel?

In the previous sections, three encoder types were presented: capacitive, optical and magnetic and trade-off criteria were defined. The results of the trade-off can be seen in Table 3.1. Given the requirements provided by Hyperion Technologies and the information available on the different encoder technologies the *Capacitive Encoder* is the most suitable encoder type to be used in the RW400 reaction wheel. With this conclusion **RQ3** is answered, capacitive encoding is the type of sensor feedback that can be implemented within the constraints of a cubesat reaction wheel and meets the requirements set the best.

	Capacitive	Optical	Magnetic
Accuracy	High	High	Low
Update Frequency	Fast	Velocity Dependant	Velocity Dependant
Power Cycle Tolerance	High	High	Low
Space Environment Tolerance	High	Low	High

Table 3.1: Comparison of Capacitive, Optical and Magnetic Encoders

<div style="text-align: right; font-size: 4em;">4</div>

Capacitive Encoder Design

Concluding from Chapter 3 a *capacitive* encoder was selected for the RW400 reaction wheel. This chapter will elaborate upon the design process of such an encoder, answering RQ4.

Section 4.1 will explain the general concept behind a capacitive encoder that will fit in the design constraints of the RW400. Sections 4.2, 4.3 and 4.4 will focus on the capacitive sensing aspect of the encoder, Section 4.6 will cover the AM demodulation method and Section 4.7 will present how the output of the encoder is post-processed to generate the rotor position. In Section 4.8 a sensitivity analysis is performed to determine how the encoder output is affected by irregularities. The chapter is concluded by answering RQ4 in Section 4.9.

4.1. General Concept

Capacitive encoders work upon the principle of a constantly varying parallel plate capacitor. By varying this capacitor as a function of the rotation angle θ of the reaction wheel it is possible to measure the current position of the reaction wheel.
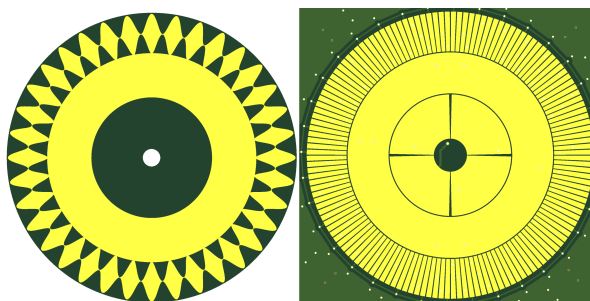
Figure 4.1: Capacitive sensing encoder. Rotor PCB (left) and stator PCB (right)

The encoder will consist of two Printed Circuit Boards (PCBs), a rotor PCB attached to the rotor of the reaction wheel and a stator PCB attached to the housing, containing all the measuring electronics, both can be seen in Figure 4.1.

The side view of this encoder can be seen in Figure 4.2. Capacitive sensing is performed through injection of an excitation signal into the excitation electrode. This high-frequency signal is transferred through to the sensitive electrode where it gets captured by the collection electrode and is fed through an amplifier to produce an output signal. By constructing a circuit that can convert the capacitance of the capacitor C_s to an output voltage, the position of the reaction wheel can be determined.

The output of turning a hypothetical capacitive encoder 360 °can be seen in Figure 4.3. Equation (4.1) describes the method in which the rotor angle can be determined based on four capacitance

<div style="text-align: center;">19</div>

measurements, $C - A$ represents the real component and $D - B$ represents the imaginary component of a rotating phasor.

$$\theta_r = atan\left(\frac{D - B}{C - A}\right) \tag{4.1}$$
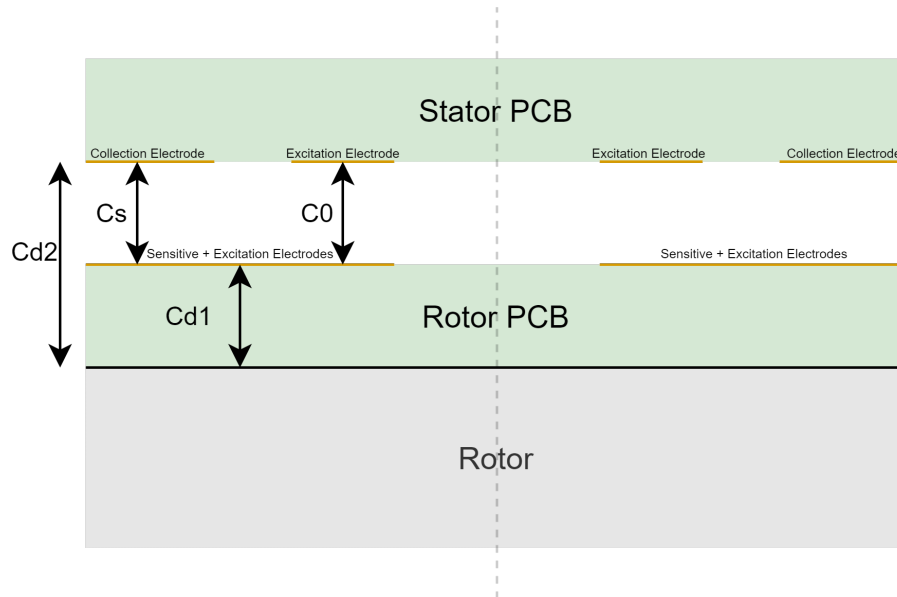
Figure 4.2: Side View of Encoder
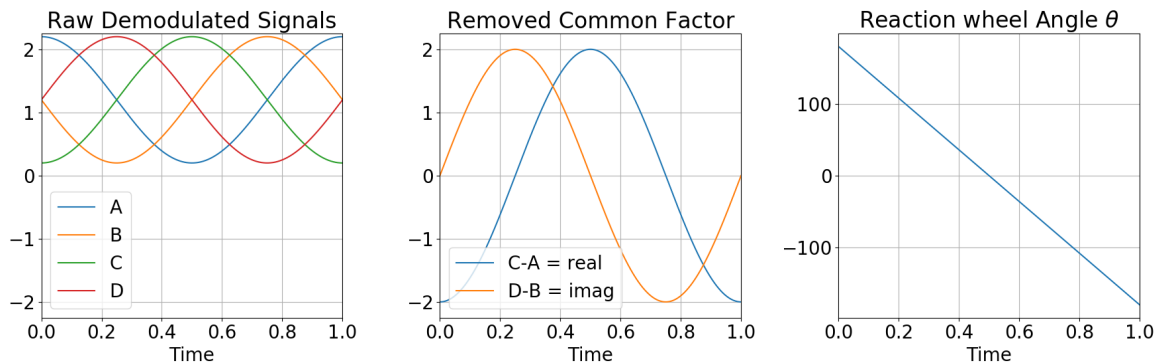
Figure 4.3: Illustrative example of converting four amplifier channels to an electrical reaction wheel angle

Reasoning from the point of view of a varying plate capacitor, there is only one general direction which the encoder circuit can go into. In order to measure capacitances, some Alternating Current (AC) signal will need to be injected, this signal will need to be converted to a voltage or current, which will eventually need to be measured. Due to the requirement of removing this "carrier" signal, AM demodulation will be required. The block diagram of a circuit which can perform this capacitance-to-reaction-wheel-position conversion can be seen in Figure 4.4. This diagram is spread out into three sections: Capacitive Sensing, AM Demodulation and Post-Processing.

Due to the fact that requirement HT_ENC_04 calls for power loss redundancy the encoder must have some form of *absolute* positional awareness in order to survive power cycles. For this reason an absolute component as well as a relative component on the encoder are used. The reasoning behind using both, instead of *just* an absolute component is presented in Section 4.5.
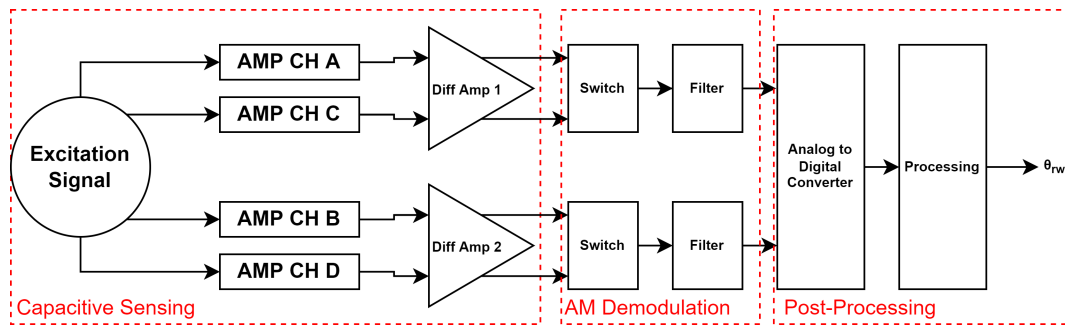
Figure 4.4: General Concept of the Encoder

Capacitive Sensing

The capacitive sensing part of the encoder chain takes the excitation signal, passes it through varying plate capacitors and converts this to a differential output voltage which scales with the amount of overlap. For this purpose four channels are utilised. In quadrature encoding (the reason this is selected will be elaborated upon in Section 4.2) two signals are required: sine and cosine. In order to remove common-mode effects such as power supply noise and a non-zero area of minimum overlap four channels are utilised, which are differentially amplified.

The reason the excitation signal is used at all is due to the fact that Direct Current (DC) voltages cannot travel through capacitively coupled circuits. Section 4.4 will elaborate upon the design of these capacitive sensing circuits.

AM Demodulation

The signals exiting the two differential amplifiers contain a high-frequency component (excitation signal) and modulated upon it a low-frequency component (amplitude variations due to a varying location of the rotor). In order to extract the low-frequency component from this signal AM demodulation will be required. Section 4.6 will elaborate on the methods used to perform this demodulation.

Post-Processing

Finally two signals are present which are the sine and cosine waves of a quadrature encoded signal. By using an ADC this signal is digitized, after which a computer can perform the calculation.

4.2. Parallel plate capacitor shape

The shape of the parallel plate capacitors will determine the method in which the location is encoded. This section will present two options for encoding this pattern and make a trade-off between them.
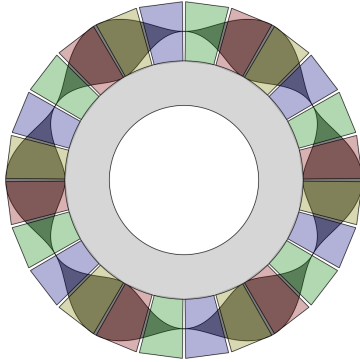
Figure 4.5: Sine Shape Encoder
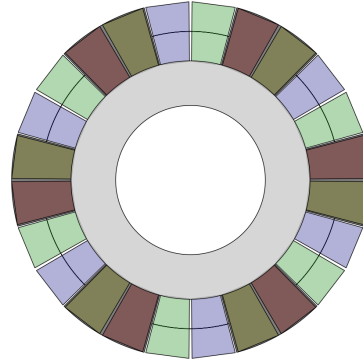
Figure 4.6: Block Shape Encoder

Sine/Quadrature

Utilising a sine wave pattern for position encoding was demonstrated by Zheng [46]. This type of encoder is based on quadrature modulation where a sine wave is sampled by four channels, two pairs of which are subtracted from one another to produce the I and Q quadrature signals that encode the position of the reaction wheel.

Block

Utilising a block-shaped pattern results in a trapezoidal output signal. This signal has rising and falling edges that can be sampled to measure the encoder position in a linear fashion.

Trade-Off

The trade-off between the two pattern shapes will be performed based on three criteria: Manufacturability, Encoding Accuracy and Encoding Capabilities. The trade-off is presented in Table 4.1. Based on this table the conclusion is that the sinusoidal pattern offers the most flexibility, is continuous and has a simpler control algorithm.

	Sinusoidal	Block
Manufacturability	More complex shape, accuracy bound by etching resolution.	Simpler shape, but very sensitive to small offsets in start/end points of the blocks.
Encoding Accuracy	Due to the continuously changing shape the sine encoder accuracy is only limited by the etching tolerances and measurement circuit.	The block shape will have dead zones in the encoding pattern due to the fact that the sensing electrodes have a non-zero gap.
Encoding Capability	The sine shape is capable of both incremental and absolute encoding and requires only very basic calculations to determine the position.	Due to the dead-zones it cannot be used for absolute encoding, furthermore the controller will be more complex.

Table 4.1: Pattern Trade-Off

4.3. Physical Model

Before modelling the electrical behaviour of the encoder, a model of the physical behaviour is set up. This section will cover the technique used to model the encoder. In Section 4.4 the electrical model is presented.

The first step in modelling the encoder is to draw its physical shape onto a canvas. The shapes are stored in the form of a polygon, which is a collection of points, that form a closed shape. In general the encoder can be divided into three components: the sensitive electrodes, the collection electrodes and the excitation electrode.

1. The sensitive electrode

2. The collection electrodes

3. The excitation electrode
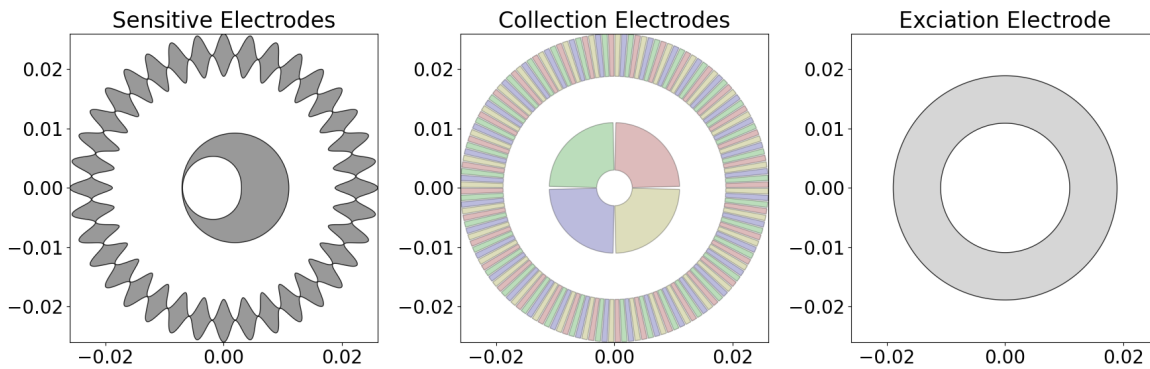
Figure 4.7: Three electrodes of the encoder

Sensitive Electrode

The sensitive electrode shape has been determined to be sinusoidal in Section 4.2. In order to generate this shape a sine wave is wrapped around a circle. First the outer and inner waves are generated utilising Eq. (4.2). R_{nom} is the nominal radius (centre line) of the shape, w is the width/amplitude of the full pattern N is the number of pattern repetitions and $w_{t,min}$ is the minimal trace width that is left in the centre. Finally, $\vec{\theta} = \{0, ..., 2\pi\}$.

$$\vec{R}_{outer} = R_{nom} + \frac{w}{4} + \frac{w}{4}cos\left(N \cdot \vec{\theta}\right) + \frac{w_{t,min}}{2} \qquad \vec{R}_{inner} = R_{nom} - \frac{w}{4} - \frac{w}{4}cos\left(N \cdot \vec{\theta}\right) - \frac{w_{t,min}}{2} \quad (4.2)$$

The sine wave is then created by converting the radial parameters R_{outer} and R_{inner} to Cartesian coordinates wrapped around a circle using Eq. (4.3)

$$\vec{P}_n = \begin{bmatrix} R_n cos\left(\vec{\theta}\right) \\ R_n sin\left(\vec{\theta}\right) \end{bmatrix} \quad (4.3)$$

by converting the two sets of points to shapes utilising a polygonal subtraction the final sensitive electrodes are generated. Figure 4.8 demonstrates this process.
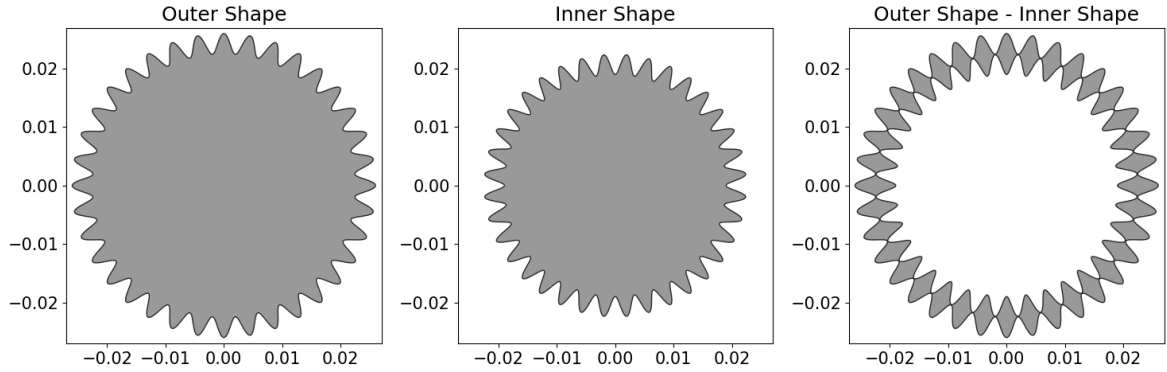
Figure 4.8: Generation of the Sensitive Electrode

Collection Electrodes

The collection electrodes are sections of an arc with a width equal to w. In order to obtain the shape of these electrodes, first a toroid shape is created which confines the radial dimensions. Second, the tangential distance is limited through a rectangle (hereafter referred to as "slice") of which the corner coordinates are provided by Eq. (4.4).

$$\vec{P} = \begin{bmatrix} (R_{inner} - a)cos(\theta_0) & (R_{inner} - a)sin(\theta_0) \\ (R_{outer} + a)cos(\theta_0) & (R_{outer} + a)sin(\theta_0) \\ (R_{outer} + a)cos(\theta_1) & (R_{outer} + a)sin(\theta_1) \\ (R_{inner} - a)cos(\theta_1) & (R_{inner} - a)sin(\theta_1) \end{bmatrix} \quad (4.4)$$

The arc over which the rectangle is drawn is from θ_0 to θ_1. The factor a is an arbitrary value such that the slice is guaranteed to have a larger radial dimension than the toroid. Finally, the intersection between the two is taken and the result is one of the collection electrodes. Figure 4.9 visually demonstrates this process. This process is repeated $4N$ times until the full set of collection electrodes is generated.
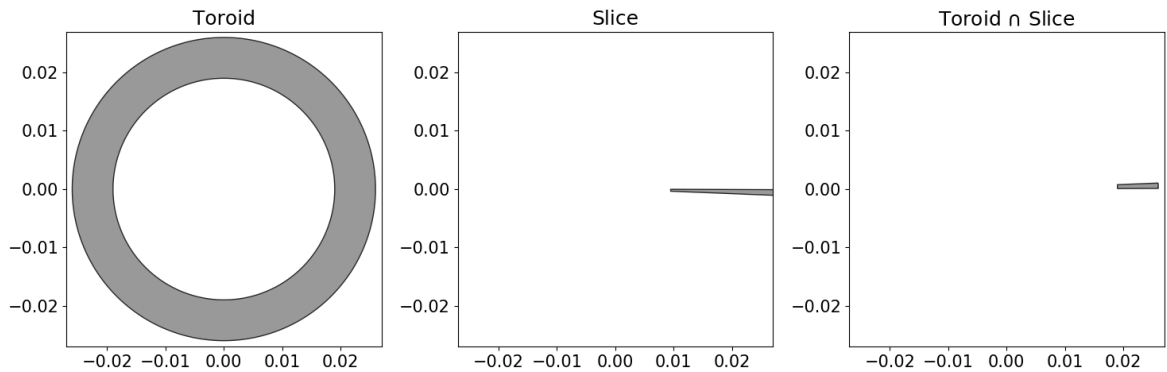
Figure 4.9: Generation of the Collection Electrode

Excitation Electrode

The excitation electrode is present on both the rotor and stator PCB. Due to the fact that it must fit in-between the sensitive electrodes, and have a constant overlapping area a toroid shape is used. The one on the stator has a fixed width of w_{exci} and is excited by excitation signal V_{sig}. The excitation electrode on the rotor side is has a width of $w_{exci} + 2o$ where o is the overlap between the excitation electrode and sensitive electrode(s). This overlap is required to conduct the signal from the excitation electrode to the sensitive electrode.

Determining the capacitances

To go from the phyisical domain to the electrical domain, the parallel plate capacitances need to be determined. Figure 4.2 contains all the capacitances that will be taken into account in the electrical

model. The value of these capacitances can be determined by taking the intersection between two polygonal shapes and calculating its area. An example of the resulting polygonal shapes of which the area is determined can be seen in Figure 4.10.
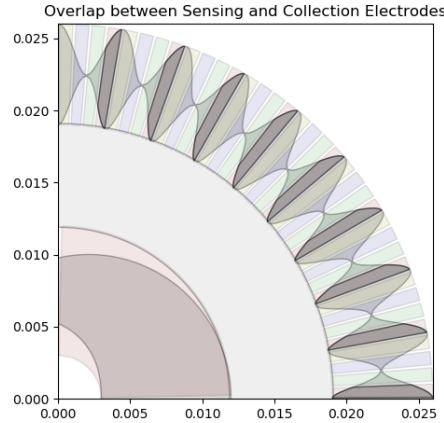
Figure 4.10: Intersection of the red channel with the relative sensitive electrode

Determining the capacitances C_0, C_{d1}, C_{d2} and C_s is done through the equations presented below. δ_{elec} represents the distance between the stator and rotor PCB, face-to-face and $t_{PCB,Rotor}$ is the thickness of the rotor PCB. The equations for C_0 and C_{d1} are the standard equation for a parallel plate capacitor, equation (4.5). The capacitance C_{d2} is a compound capacitance built up from the section of air (the gap between the stator and rotor) and a section of PCB (the rotor PCB).

$$C = \frac{\kappa \varepsilon_0 A}{d} \tag{4.5}$$

$$C_0 = \varepsilon_0 \kappa_{air} \frac{A_{EXCI}}{\delta_{elec}} \qquad C_{d1} = \varepsilon_0 \kappa_{FR4} \frac{A_{SENS} + A_{EXCI}}{t_{PCB,Rotor}} \qquad C_{d2} = \varepsilon_0 \frac{\kappa_{air} \kappa_{FR4} A_{COLL}}{\kappa_{air} t_{PCB,Rotor} + \kappa_{FR4} \delta_{elec}}$$

Fringe Capacitance

Equation (4.5) assumes that the electric field between the to plates in the parallel plate capacitor is uniform and perpendicular to the capacitor electrodes [8]. In reality this assumption is not true, in particular for capacitors where the ratio between the plate dimensions (for example the side length of a rectangular plate) and the gap between the electrodes is small (<10). The dimensions of the sensitive electrodes and collection electrodes are in the same order of magnitude as the air gap, meaning that fringing effects cannot simply be excluded.

Determining fringing effect capacitance is not a problem with a clear analytical solution. Throughout time attempts have been made, such as for example Slogett and Hutson [38][21]. The approximations for the total capacitance as a function of electrode are all in the following form:

$$C \approx C_{elem}\left(1 + \frac{2d}{\pi R} ln\left(\frac{2e\pi R}{d}\right)\right) \tag{4.6}$$

Where the factor $2e\pi R$ varies slightly between variations. These approximations all rely on assumptions in the shape of the parallel plate capacitor (being circular) and will be difficult to unify for arbitrary shapes.

Due to the difficulty of predicting fringe capacitance effects, combined with the following two arguments it will not be included in the model. The results in the verification of the encoder will show whether fringe capacitance has a large influence on the encoder performance.

1. **Fringe capacitance increases the capacitance**
   The effect of fringe capacitance *increases* the capacitance of a parallel plate capacitor. Given

that the gain of the amplifier is related to the capacitance of C_s, a higher capacitance means the signal to noise ratio improves due to a larger input signal.

2. **The effect occurs for every sensing channel**
   The encoder retrieves the position information by using both the quadrature components. Due to the fact that the fringe capacitance effect occurs in the exact same manner for each channel the effect is consistent. Furthermore, both quadrature components are calculated using differential amplification, removing common components in the signal.

4.4. Electrical Model & Amplifier Topology Selection

With the physical model and parameters established in the previous section, the electrical model will be elaborated upon in this section. In this section a single-ended amplifier topology will be used to design and optimise the electrical aspect of the encoder. Due to the fact that two of the channels are subtracted from one another (per Equation (4.1)) in reality a differential setup will be used. However, to simplify the modelling, a single-ended approach is presented in this chapter. The implications of this decision and reasoning for it are described in Section 7.2.8.

The amplifier channels will convert the varying capacitance C_s into either a voltage or a current. In order to determine the best amplifier topology for this task a trade-off is made. This section will present a model for both a trans-impedance (current to voltage) amplifier and a non-inverting (voltage to voltage) amplifier topology, followed up by a trade-off.

4.4.1. Ideal Circuit Modelling

Electrically the encoder in Figure 4.2 can be modelled using the circuit described in Figure 4.11. Two different configurations can be selected for the sensing electronics, a *Voltage-to-Voltage* encoder and a *Current-to-Voltage* encoder. The assumption is made that the rotor itself is at ground potential.
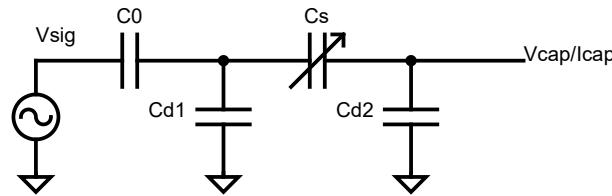
Figure 4.11: Electrical model of the capacitive encoder

Figure 4.12 contains the trans-impedance amplifier circuit which converts I_{cap} into a voltage which can be sensed. Figure 4.13 contains the non-inverting amplifier circuit which converts V_{cap} to an output voltage which can be sensed.
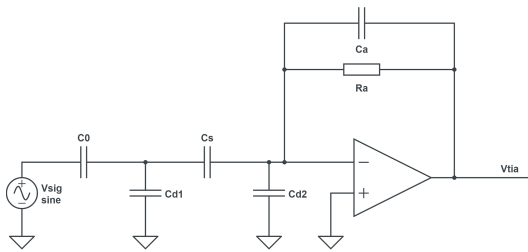
Figure 4.12: Trans-impedance Amplifier Circuit
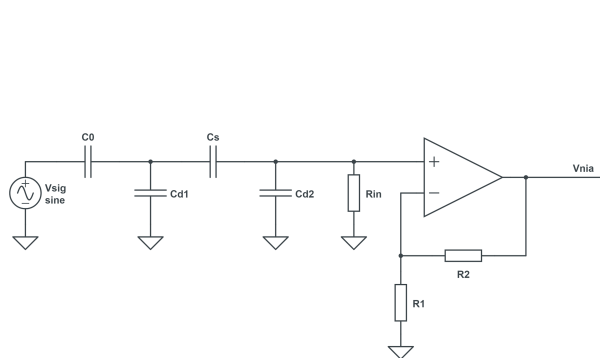
Figure 4.13: Non-inverting Amplifier Circuit

Under ideal circumstances where R_a and R_{in} are considered infinite Equation (4.7)-(4.10) analytically describe the output voltages V_{TIA} and V_{NIA} for a given input voltage V_{sig}.

Trans-Impedance Amplifier

$$I_{cap} = \frac{V_{sig}}{Z_0 + \frac{Z_0 Z_s}{Z_{d1}} + Z_s} \qquad (4.7)$$

$$V_{TIA} = -I_{cap} \frac{Z_a}{\frac{1 + Z_a/Z_{d2}}{A_{amp}} + 1} \qquad (4.8)$$

Non-Inverting Amplifier

$$V_{cap} = \frac{V_{sig} \cdot Z_{d2}}{\frac{Z_0 Z_s + Z_0 Z_{d2}}{Z_{d1}} + Z_0 + Z_s + Z_{d2}} \qquad (4.9)$$

$$V_{NIA} = V_{cap} \frac{1}{\frac{1}{A_{amp}} + \frac{1}{1 + \frac{R_2}{R_1}}} \qquad (4.10)$$

Verification

Model verification is performed by comparing it to LTSpice, an industry standard circuit simulation program. The circuits from Figures 4.12 and 4.13 were simulated in LTSpice. The physical model from Section 4.3 was used to generate a set of values for the passive components in the circuit. Comparing the two models with one another is done through a bode plot. Figures 4.14 and 4.15 contain these plots for the TIA and NIA respectively.
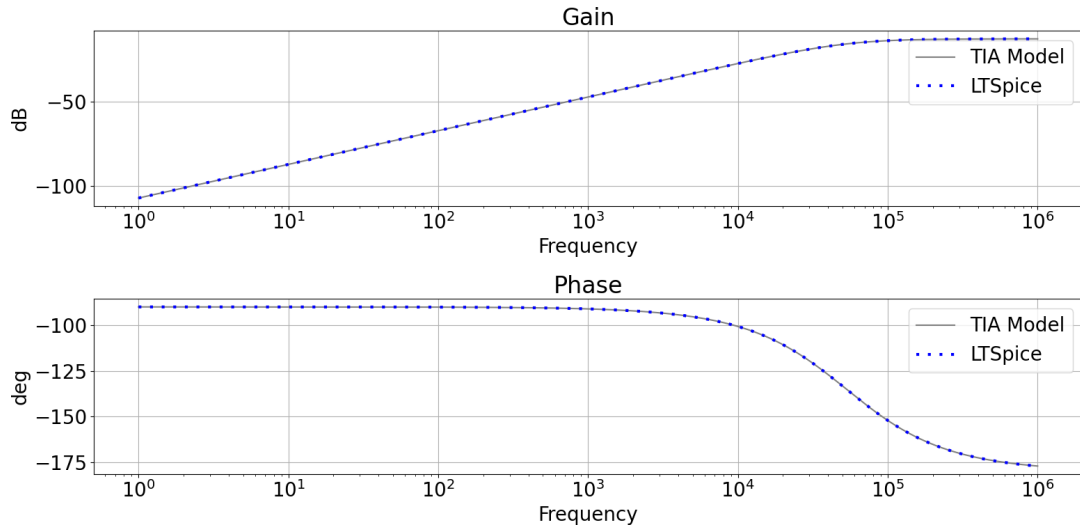
Figure 4.14: Comparison between the TIA model and LTSpice
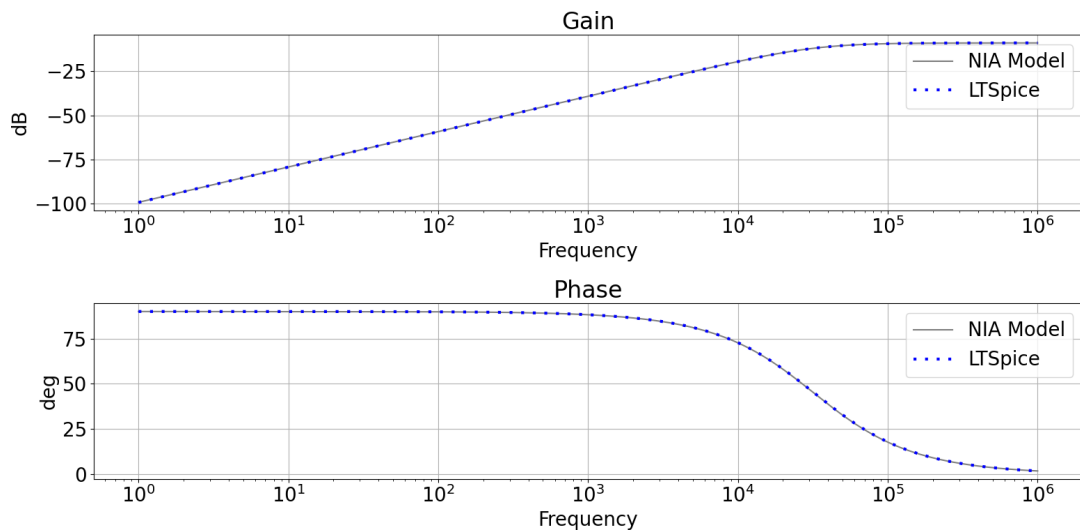
Figure 4.15: Comparison between the NIA model and LTSpice

4.4.2. Non-Ideal Circuit Modelling

In the previous section models for both the amplifier designs were provided. These can be used to create initial estimates of encoder performance, but however do not form an accurate representation of reality. The model presented in this section will contain both the influence of noise and the effect of

input resistors R_{in} and R_a.

External noise factors such as for example induction from the motors are not included in the model. This was done due to the fact that these noise factors would be similar for both designs and are not dependant on component selection but on PCB layout, thickness of the rotor, relative position of components, field strength of the motor etc.

The main physical mechanisms for noise generation for amplifier circuits are given below [31] [40].

- Thermal Noise

- Shot noise

- Excess Noise (Flicker Noise, 1/f Noise)

- Two-Port Noise

The model will include the effects of Two-Port Noise and Thermal noise, but will not include Shot Noise and Excess Noise. The reasoning behind this is briefly described below.

The current flowing through the components in the model is in the order of $20\mu A$. The Root-Mean-Square (RMS) current shot noise can be calculated using Equation (4.11) [40]. Using $I = 20\mu A$, $e = 1.6 \cdot 10^{-19}$, a bandwidth of $5000 rpm/60 * 36 * 2 = 6 kHz$ this yields an RMS shot noise of $0.19 nA$, which is five orders of magnitude smaller than the currents that flow into the amplifier stage and can thus be considered negligible.

$$I_{n,shot,rms} = (2eBI)^{1/2} \tag{4.11}$$

Excess noise will also be considered negligible in this circuit design. Figure 4.16 shows a series of noise characteristics for 10k resistors at 10.4V [29]. It demonstrates that the 1/f noise decreases rapidly with increasing frequency. Due to the fact that the encoder will make use of Metal Film or better resistors and the plot demonstrates that for these types of resistors the 1/f noise drops below the thermal noise around 10-100 Hz, this means that at excitation frequencies of 100 kHz+ is this noise is negligible. The 1/f noise in operational amplifiers is often referred to in the datasheet in the range from 0.1 to 10 Hz, and can thus safely be neglected [44].
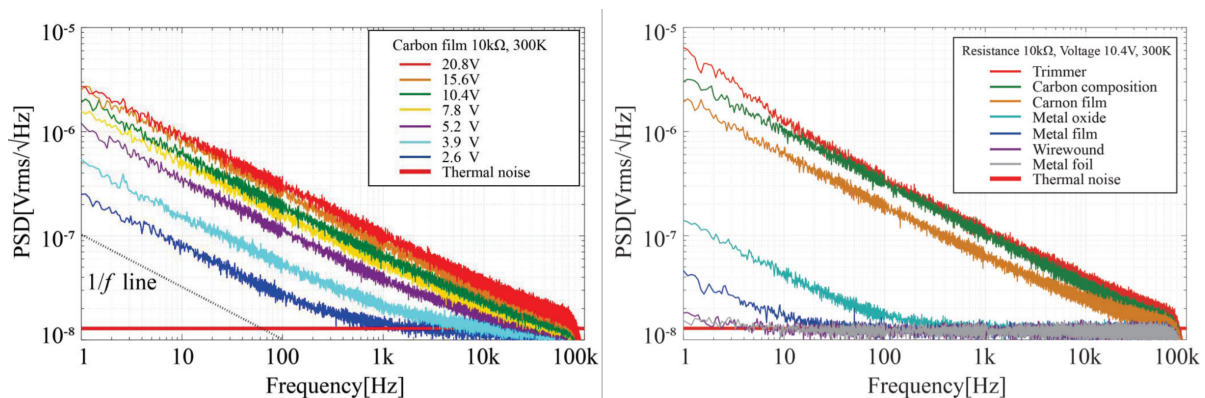
Figure 4.16: Carbon film resistor current noise (left), Current noise for various 10.4k resistors [29]

Figures 4.17 and 4.18 show the circuits from Figures 4.12 and 4.13 but in addition their noise components. Operational amplifiers specify input-referred voltage and current noise, which can be added in the method demonstrated [31].
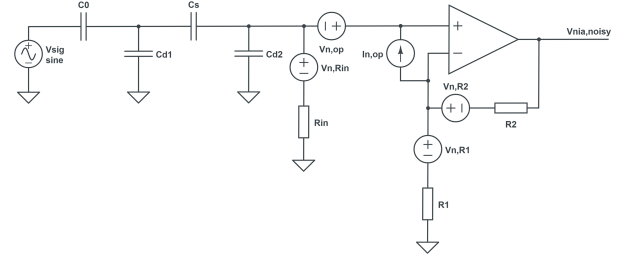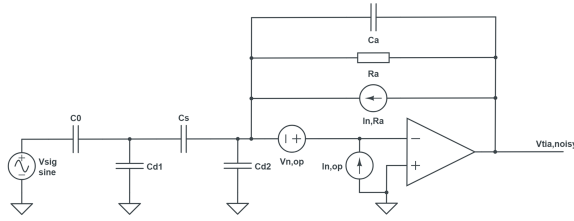
Figure 4.17: Trans-impedance Amplifier Circuit with Noise　　　Figure 4.18: Non-inverting Amplifier Circuit with Noise

Using circuit theory (KCL) to analyse the circuits in Figures 4.17 and 4.18 the following equations can be derived. Note that for this more realistic model R_a and R_{in} are no longer considered infinite. The inclusion of R_{in} in the Non-Inverting Amplifier model requires a re-definition for V_{cap}.

Trans-Impedance Amplifier

Equation (4.12) describes the behaviour of the non-ideal trans-impedance amplifier. The first term, as expected is the same as the ideal equation described in Section 4.4.1. The additional terms represent noise components. The values for $I_{n,op}$, $V_{n,op}$ and $I_{n,Ra}$ are defined as $V/\sqrt{Hz}$ meaning they will need to be multiplied by the square root of the system bandwidth. Due to the fact that all the noise components are considered white, equation (4.13) describes the total voltage noise RMS.

$$V_{TIA,noisy} = -I_{cap} \frac{Z_a}{\frac{1+Z_a/Z_{d2}}{A_{amp}} + 1} - \left(I_{n,op} \frac{Z_a}{\frac{1+Z_a/Z_{d2}}{A_{amp}} + 1} + I_{n,Ra} \frac{Z_a}{\frac{1+Z_a/Z_{d2}}{A_{amp}} + 1} + V_{n,op} \frac{Z_a/Z_{d2}+1}{\frac{1+Z_a/Z_{d2}}{A_{amp}} + 1} \right) \quad (4.12)$$

$$N_{tia,rms} = \sqrt{\left(I_{n,op} \frac{Z_a}{\frac{1+Z_a/Z_{d2}}{A_{amp}} + 1} \sqrt{B} \right)^2 + \left(V_{n,op} \frac{Z_a/Z_{d2}+1}{\frac{1+Z_a/Z_{d2}}{A_{amp}} + 1} \sqrt{B} \right)^2 + \left(\sqrt{\frac{4kTB}{R_a}} \frac{Z_a}{\frac{1+Z_a/Z_{d2}}{A_{amp}} + 1} \right)^2} \quad (4.13)$$

Non-Inverting Amplifier

Equations (4.14) and (4.15) describe the behaviour of the non-ideal non-inverting amplifier. The first term, as expected is the same as the ideal equation described in Section 4.4.1. The additional terms represent noise components. Similar to the Trans-Impedance Amplifier all the noise components are defined as $V/\sqrt{Hz}$ meaning they will need to be multiplied by the square root of the system bandwidth. Equation (4.16) describes the total voltage noise RMS.

$$V_{cap,n} = V_{sig} \frac{Z_{d1}Z_{d2}Z_{in}}{Z_{d1}Z_{d2}(Z_{in} + Z_s + Z_0) + Z_{d1}Z_{in}(Z_s + Z_0) + Z_{d2}Z_0(Z_{in} + Z_s) + Z_{in}Z_sZ_0} \quad (4.14)$$

$$V_{NIA,noisy} = V_{cap} \frac{1}{\frac{1}{A_{amp}} + \frac{1}{1+\frac{R_2}{R_1}}} + \left(\frac{V_{n,op}}{\frac{1}{A_{amp}} + \frac{1}{1+\frac{R_2}{R_1}}} + \frac{I_{n,op}R_2}{\frac{1+R_2/R_1}{A_{amp}}+1} + \frac{V_{n,R_{in}}}{\frac{1}{A_{amp}} + \frac{1}{1+\frac{R_2}{R_1}}} - \frac{V_{n,R_1}\frac{R_2}{R_1}}{\frac{1+R_2/R_1}{A_{amp}}+1} - \frac{V_{n,R_2}}{\frac{1+R_2/R_1}{A_{amp}}+1} \right) \quad (4.15)$$

$$N_{nia,rms} = \sqrt{\left(\frac{V_{n,op}}{\frac{1}{A_{amp}} + \frac{1}{1+\frac{R_2}{R_1}}} \sqrt{B} \right)^2 + \left(\frac{I_{n,op}R_2}{\frac{1+R_2/R_1}{A_{amp}}+1} \sqrt{B} \right)^2 + \left(\frac{1}{\frac{1}{A_{amp}} + \frac{1}{1+\frac{R_2}{R_1}}} \sqrt{4kTBR_{in}} \right)^2 + \left(\frac{\frac{R_2}{R_1}}{\frac{1+R_2/R_1}{A_{amp}}+1} \sqrt{4kTBR_1} \right)^2 + \left(\frac{1}{\frac{1+R_2/R_1}{A_{amp}}+1} \sqrt{4kTBR_2} \right)^2} \quad (4.16)$$

4.4.3. Trade-Off

The two amplifier topologies were compared with similar input conditions. Due to the dependence of the noise figures on the used amplifier (which can be optimised for both topologies) and passive

components the direct comparison between the two topologies will require an optimisation process for both. However in simulations of both topologies a deal-breaker became immediately obvious for the non-inverting amplifier.
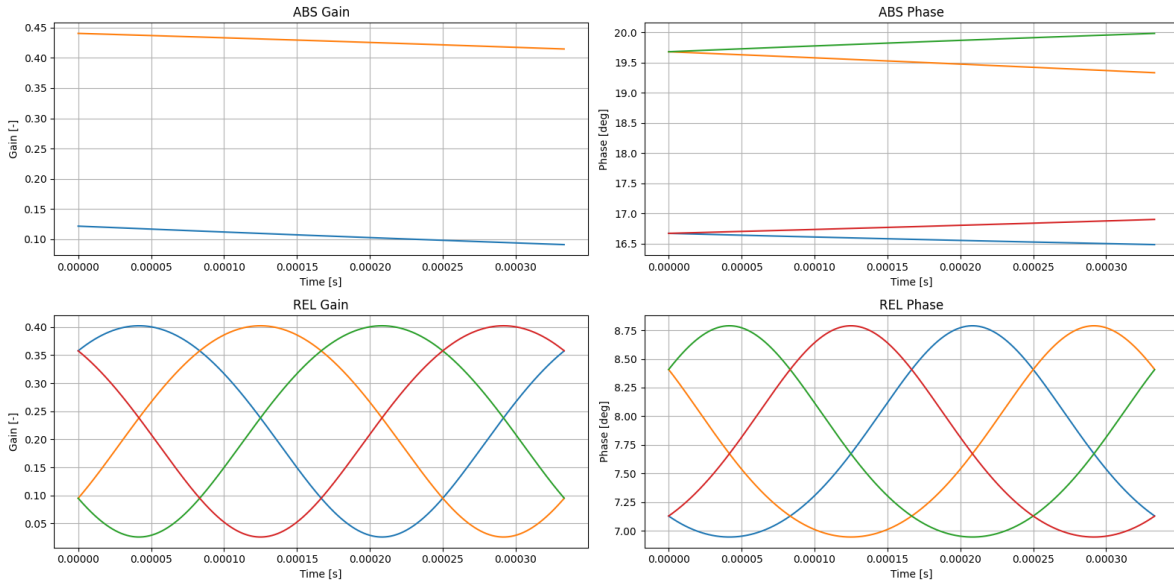
Figure 4.19: Non-Inverting Amplifier Gain & Phase for a rotation of 10 °

The phase shift between the input signal V_{sig} and output signal V_{NIA} or V_{TIA} is consistent for the TIA, but for the NIA it is dependant on the value of C_s. This means that the output signal of the NIA is constantly changing phase w.r.t. the input signal, making decoding the signal with an AM demodulator impossible. Furthermore a quick comparison showed that the noise figures for both amplifiers under similar conditions were similar. Thus the **trans-impedance amplifier** is the superior topology and will be used in the final design.

4.4.4. Stability
In order to assess whether an amplifier topology is stable and will not oscillate a Bode plot of the loop gain can be used. While not a full waterproof method of determining whether a given topology is stable, it does allow for an initial estimation of the amplifier stability. For an amplifier topology to be stable states that the loop gain of the amplifier topology must be below unity once a phase shift of 180 deg is reached. If this is not the case, the output signal, through the feedback path is injected on the input signal and causes constructive interference, causing oscillation[6].

$$G_{cl} = \frac{A}{1 + A\beta} \quad => \quad A\beta \neq -1 \tag{4.17}$$

Equation (4.17) demonstrates this oscillation condition. The loop gain bode plot can be seen in Figure 4.20. From this plot it can be concluded that the amplifier is always stable due to the fact that the phase shift never even reaches 180 deg. Furthermore if a unity gain stable op-amp is selected it will add a dominant pole to the system to ensure it remains stable [6].
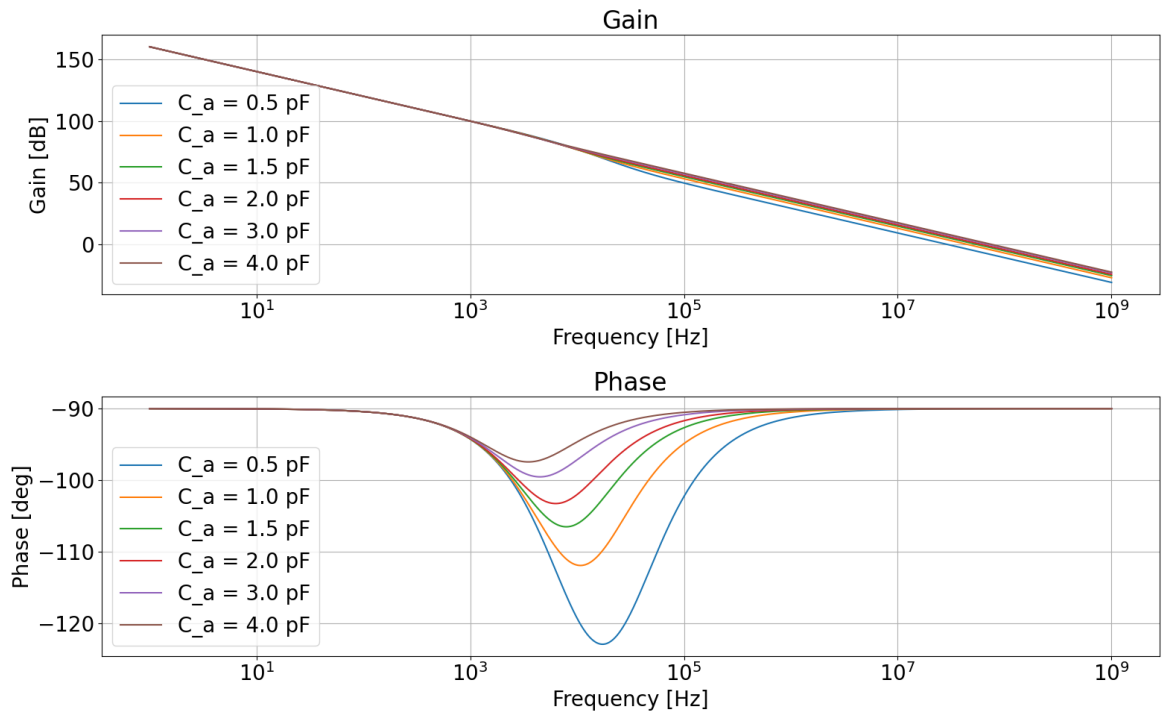
Figure 4.20: TIA loop gain bode plot for various values of C_a

4.5. Dimension Optimisation

The dimensions of the sine shaped pattern determine the size of the capacitances in the model. Larger areas will result in larger capacitances, which are simpler to measure and are less prone to manufacturing tolerances. When comparing a single revolution pattern (such as R_1 in Figure 4.21) to a more repeating pattern (R_2) the repeating area is less prone to external disturbances. This is due to the fact that the disturbances are averaged out over many separate sensing electrodes.

Hou et al. [20] suggests that it is possible to utilise an analog (single) part for a coarse, analog measurement and an incremental part around it for finer position control. Due to the fact that the encoder must be capable of handling momentary power losses this solution will also be used for this encoder. The accuracy of this absolute component does not have to be the same as that of the full encoder. In order to ensure that it is always known 'which' of the N repetitions of the relative component the encoder is in, the accuracy must be at least $2N$. In order to pick a value to start with, 8-bit (1/256°) is assumed. Because the system is optimised, unless this requirement on the internal component is deemed not strict enough, this will not need to be changed. This leaves the dimensions in Figure 4.21 and the repetition factor N to be determined.
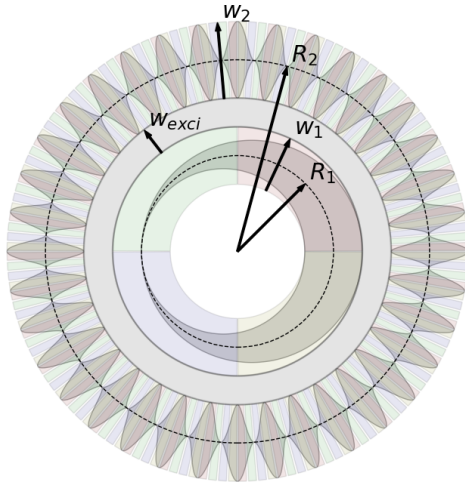
Figure 4.21: Dual Encoder Dimensions   Figure 4.22: Collection Electrode Separation Angle
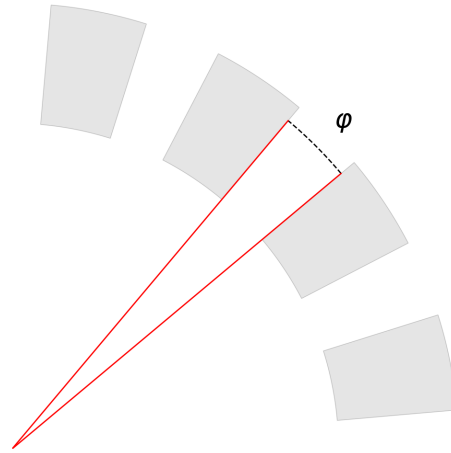
Optimisation of the encoder pattern will occur by maximising the $\delta V/\delta\theta$ for the smallest rotation that shall be detectable. This maximises the signal to noise ratio of the encoder and ensures proper operation. Should $\delta V/\delta\theta$ drop below the noise floor of the trans-impedance amplifier then this signal can never be recovered.

$$\frac{\delta V_{out}}{\delta\theta} = \frac{\delta V_{abs}}{\delta\theta} + N\frac{\delta V_{inc}}{\delta\theta} \tag{4.18}$$

The optimisation process for the encoder pattern will consist of two components. The first is N, the number of repetitions in the incremental encoder. The second is the physical layout of the encoder, meaning R_1, R_2, w_1, w_2 and w_{exci}. (see Figure 4.21) Table 4.2 contains the parameters that were fixed before performing this optimisation. Some of the parameters are subject to change in the future.

Parameter	Value	Comment
$R_{outer} = R_2 + \frac{w_2}{2}$	$26mm$	Limited by prototype test wheel size.
$R_{inner} = R_1 - \frac{w_1}{2}$	$3mm$	Limited by prototype bolt mount.
φ_{inc}	$0.45°$	Restricted by minimal pad spacing on PCB.
φ_{abs}	$2.5°$	Restricted by minimal pad spacing on PCB.
Required Accuracy (Relative)	12-bit	Flows from requirement
Required Accuracy (Absolute)	8-bit	Assumption
Amplifier Topology	TIA	
Amplifier	LTC6268-10	Selected for its low current noise, subject to change.
Component Values	$R_a = 3M\Omega, C_a = 1pF$	Values used in development, subject to change/further optimisation in the future.
δ_{elec}	1mm	Value used in development, subject to change/further optimisation in the future.
$t_{PCB,Rotor}$	1.6mm	Value used in development, subject to change/further optimisation in the future.
$V_{sig,amplitude}$	$3.3V$	Value used in development, can be generated by MCU.
$f_{carrier}$	250 kHz	Value used in development, subject to change/further optimisation in the future.

Table 4.2: Pre-determined parameters for pattern optimisation of the encoder

Both optimisations will be determining the δV for a rotation of $\delta\theta = \frac{360}{2^{12}}$ for the relative component and $\frac{360}{2^8}$ for the absolute encoder. These values are captured at the location where the $\frac{\delta V}{\delta_\theta}$ is expected to be minimal, which results in the location where the sin-shape is at its peak, because here the derivative is at its minimum.

In order to achieve 12-bit resolution for the relative component and 8-bit resolution for the absolute component, the noise injected into the signal must be less than half of the LSB. Due to the fact that later stages in the encoder chain might add more noise (although this effect is assumed to be minimal thanks to Friis formula for cascaded amplifiers) for now a safety margin is taken where the noise RMS must be less than 1/4th of the LSB value.

Optimising the number of repetitions

The number of repetitions N, has a large contribution to the total δV_{out} for the encoder. Figure 4.23 documents the results from a simulation where N is varied from 1 to 200. The trend is that a larger N generally increases $\frac{\delta V}{\delta \theta}$ up until a maximum is reached at $N = 134$. The separation angle between the electrodes, φ, can be seen in Figure 4.22.

Due to the restriction on φ, which is a fixed parameter flowing from manufacturing constraints, the width of the collection electrodes becomes so small that the decreasing physical size becomes a limiting factor. Going past 200 is physically impossible due to the fact that zero space is remaining for the collection electrodes.
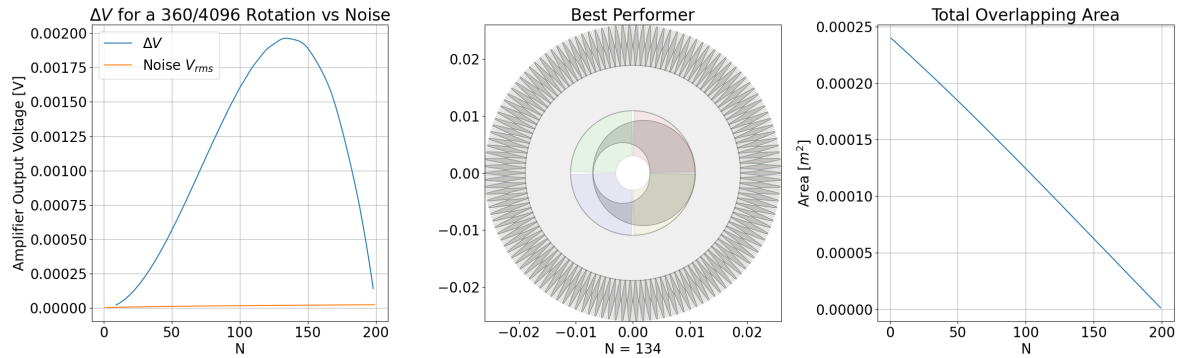
Figure 4.23: Channel 1 Amplifier Response vs N

Whilst selecting the maximum of $N = 134$ seems like an optimal solution, in reality this is not possible due to practical limits. In order to restrict the model further and obtain useful values for N, a limit is imposed. The physical width of the collection electrodes may not be smaller than the minimum via size, which is 0.45mm [22]. In order not to push the initial prototype to the absolute limit and account for factors such as the via size influencing the overlapping area, the minimum via width is set to 0.6mm. The result of this simulation is presented in Figure 4.24.
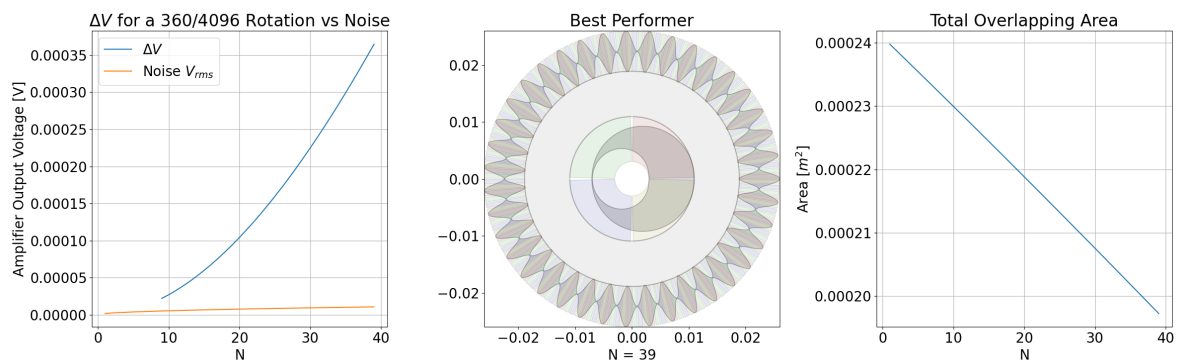
Figure 4.24: Channel 1 Amplifier Response vs N, restricted to practical limits.

The result from this is that the closest one can come to the optimum is with $N = 39$. In order to ease integration of the encoder with Hall effect sensor data it makes sense to make N a multiple of 12, which results in $N = 36$.

Optimising the dimensions

Optimising the pattern dimensions is performed utilising the same method, maximising Eq. (4.18). Optimisation occurs in two stages:

1. **Check if the encoder design is valid**
   This means that the inner and outer dimensions are validated to fit.

2. **Simulate the encoder**
   The encoder is simulated for steps of $\delta\theta$ and the difference in output is logged.

The result of this optimisation process can be seen in Figure 4.25. The δV determined here is for the incremental encoder.
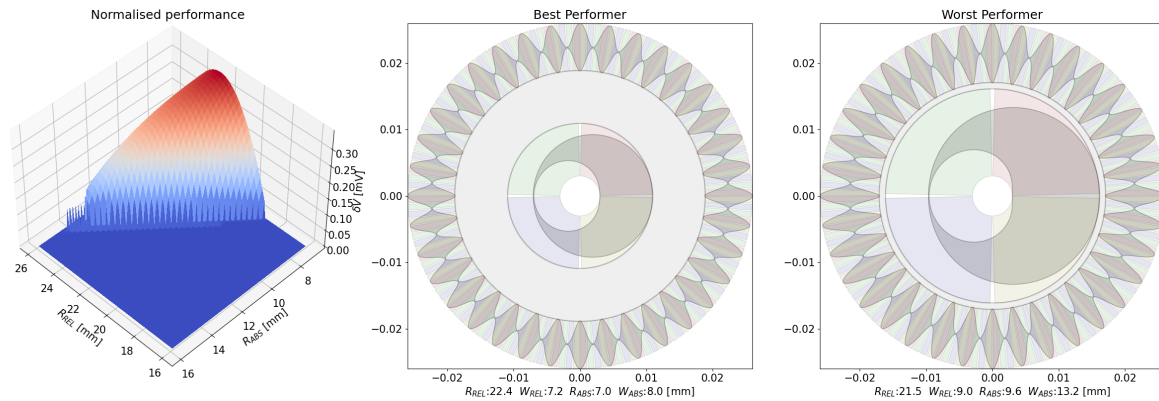
Figure 4.25: Optimal dimensions of the encoder

Conclusion

The process highlighted in this section was iteratively performed. In conclusion, the most optimised encoder design for the given input parameters can be found in Table 4.3

Parameter	Value	Unit
N	36	-
R_{REL}	22.4	mm
R_{ABS}	7.0	mm
W_{REL}	7.2	mm
W_{ABS}	8.0	mm

Table 4.3: Optimal Encoder

4.6. Amplitude Demodulation

With the encoder layout and amplifier topology selected in the previous sections, the output of the encoding channels is an amplitude modulated signal. In order to convert this signal to a signal which can be sampled by the ADC it must first be demodulated. This section will present the design of the demodulation stage of the encoder.

4.6.1. Basic Principle

In amplitude modulation the baseband signal (in this case the reaction wheel position) is shifted up to the carrier frequency. Demodulating is done by multiplying the modulated signal with the carrier signal, which will shift the modulated signal down to baseband *and* up to twice the carrier frequency. Finally by low-pass filtering the signal the $2f_c$ component is filtered out and the original baseband signal remains.

Figure 4.26 describes the AM demodulation process of the reaction wheel encoder. The *Modulated Signal* is the reaction wheel position modulated with the carrier frequency through Eq. (4.19). Here A_{DC} represents the DC offset on the signal coming from the TIA, f_c is the carrier frequency and ω_{rw} is the reaction wheel velocity.

$$V_{mod} = A_{DC} + A_{sig}sin(2\pi f_c t)sin(\omega_{rw}t) \tag{4.19}$$

In this encoder the demodulation is accomplished by using a square wave at the original carrier frequency instead of a sine wave. Why this is done is elaborated upon in Section 4.6.2.

Eq. (4.20) represents the multiplication with a square wave, where the square wave is represented by the *sign* function of a sinusoid. The result from this multiplication is the *Square Wave Multiplied Signal*. Due to the fact that a square wave is used, all the harmonics of the square wave will interact with the signal, not only shifting it to DC level and $2f_c$ like how a sine wave would, but also shifting it to all other *even* values of nf_c.

$$V_{multip} = sgn(sin(2\pi f_c t))V_{mod} \tag{4.20}$$

Finally, a low-pass filter is utilised to filter out all the high-frequency harmonics and the remaining signal is the position of the reaction wheel, which can be sampled.
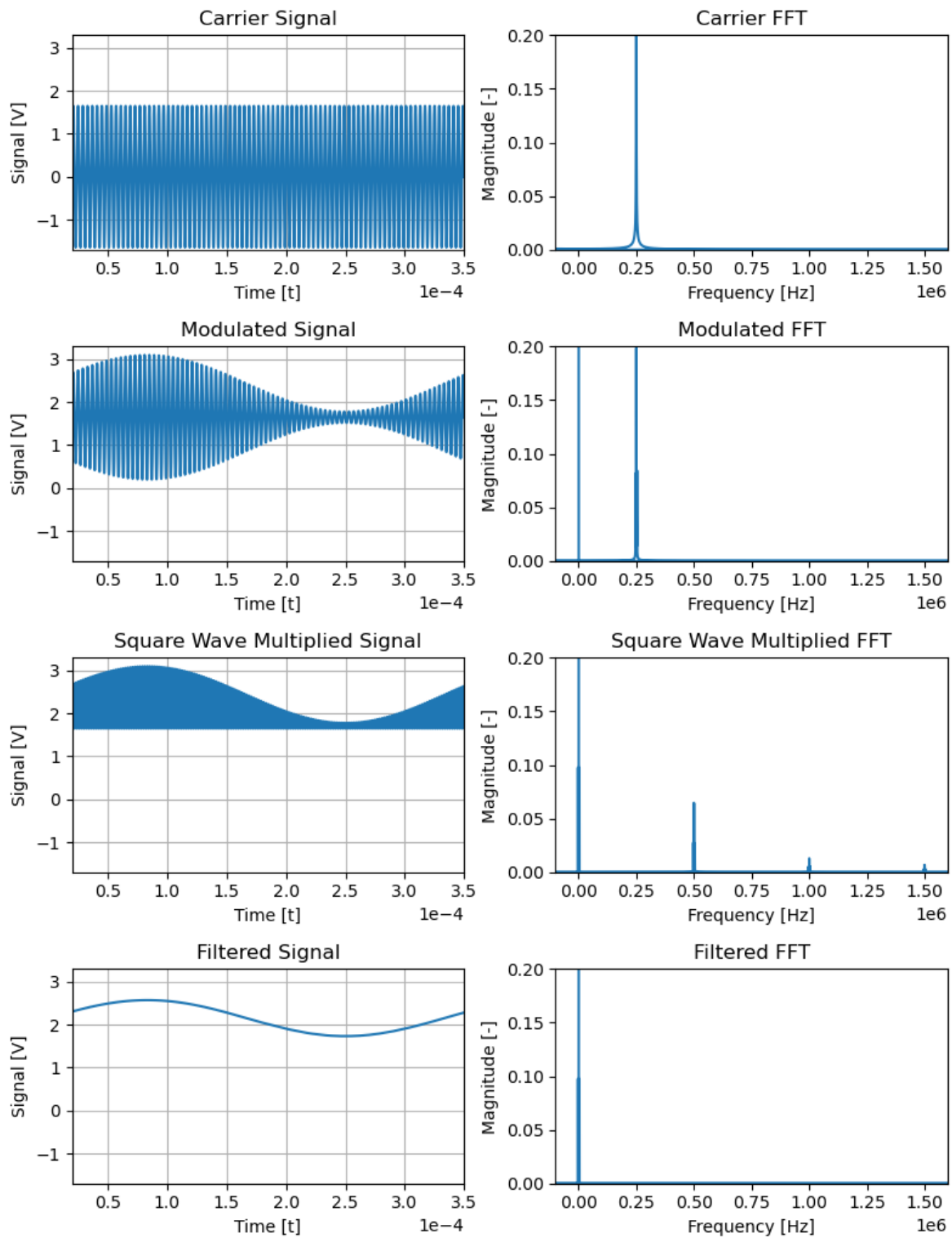
Figure 4.26: Ideal Example of AM Demodulation

4.6.2. Analog Multiplier vs Switching Device

Demodulating the AM signal can be done through the use of an analog multiplier and a switching device. This section will discuss both methods and elaborate why the switching method is selected for the encoder.

Analog Multiplier

Ideal AM demodulation makes use of an analog multiplier to perfectly multiply the incoming signal with the carrier signal. This task can be performed through the use of an analog multiplier, for which several options exist. In theory this is the most proper way of demodulating AM signals, in practice however, analog multipliers, such as the *Gilbert Cell* suffer from linearity problems. [19, p. 713]

Figure 4.27 demonstrates a standard Gilbert cell and Figure 4.28 highlights the transfer characteristics of a coupled pair of transistors, of which the Gilbert cell has three. From these two plots it can be concluded that for small input voltages V_1 or V_2 the voltage to current transfer is linear, however for larger voltages the transfer becomes non-linear. These non-linearities will distort the output of the encoder and thus harm the accuracy of the encoder.
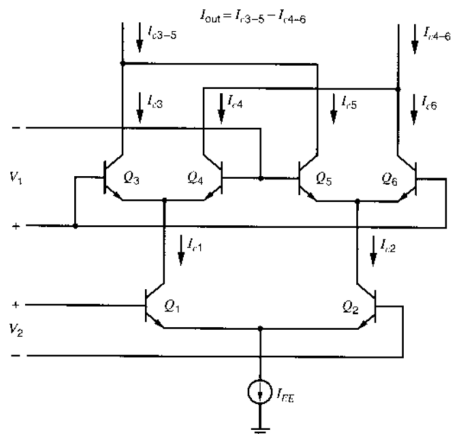
Figure 10.9 Gilbert multiplier circuit.

Figure 10.7 The dc transfer characteristic of emitter-coupled pair.

Figure 4.27: Gilbert Cell [19]   Figure 4.28: Transfer Characteristics of Coupled Pair [19]

Switching Device

In order to circumvent the non-linearity issues of an analog multiplier, a switching device can be used to instead multiply the signal with a square wave. Equation (4.21) describes the behaviour of this switch-based design. Switching devices utilising clear digital levels do not suffer from these non-linearity effects, furthermore these types of switching devices are much simpler to implement and there are more options due to the abundance of digital signals.

$$V_{out} = \begin{cases} V_{in,1} & \text{when } V_{sq} \text{ is high} \\ V_{in,2} & \text{when } V_{sq} \text{ is low} \end{cases} \tag{4.21}$$

Noise Performance

Figure 4.29 compares sine wave and square wave demodulation with one another. The main difference between the two types of modulation is the fact that not only the first harmonic of the square wave (f_c), but also the third, fifth, etc. harmonics interact with the signal, shifting information to all the even numbered frequencies of f_c.
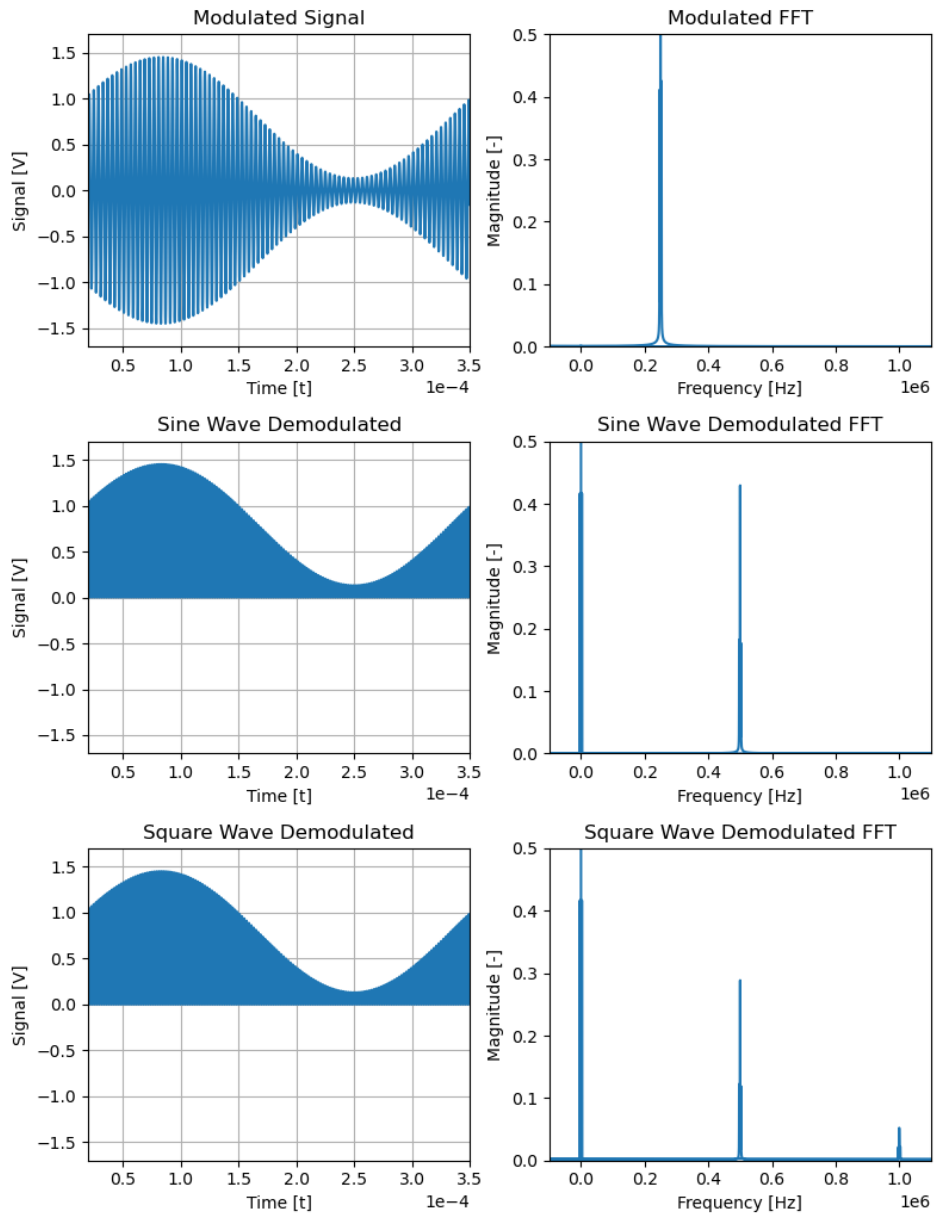
Figure 4.29: Sine Wave Demodulation vs Square Wave Demodulation

Applying a low-pass filter with a cut-off frequency below f_c removes the even numbered harmonics as well, meaning that for the *signal* there is no difference between utilising the two methods. The remaining difference to be analysed is the noise performance of the square wave method compared to the sine wave method. Figure 4.30 shows the noise spectrum and the harmonics of the square wave with the bands around each of the harmonics.
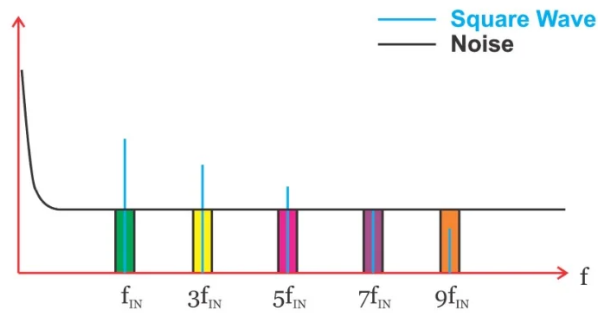
Figure 4.30: Noise PSD and bands around harmonics of f_{in} (f_c) [2]

For the sine wave demodulation scheme the band around f_c is shifted to the baseband, this includes the signal which is to be sampled. For the square wave demodulation scheme not only the f_c band is shifted back to baseband, but also all the odd harmonics of f_c. It can be proven that under the assumption that the noise power spectral density is flat (the operating frequency is sufficiently high such that flicker noise is no longer a factor) the amount of noise shifted to baseband is the exact same as that for a sine wave [2].

One thing that needs to be considered is the fact that if the PSD is not flat, extra noise *is* coupled back to baseband as compared to a sine wave multiplication. This will need to be taken into account when selecting other components in the circuit, such as switching power supplies.

4.6.3. Implementation
The implementation of the AM demodulation is described in Figure 4.31. The output from the differential amplifier (V_+,V_-) are fed into a Single Pole Double Throw (SPDT) switch. This output is then filtered, leaving only the baseband signal.
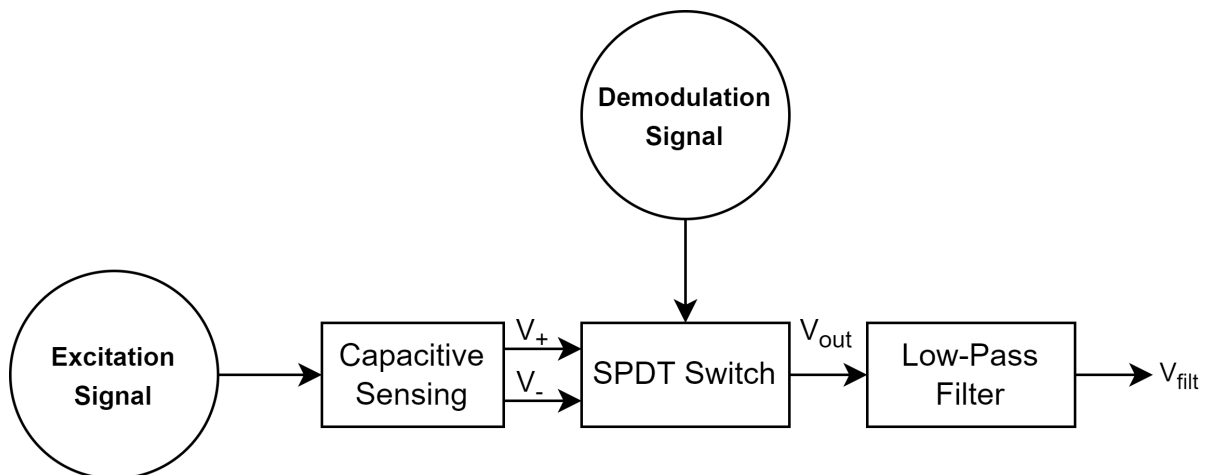
Figure 4.31: Description of the AM demodulation implementation

Generating the demodulation signal
The square wave signal with which the trans-impedance amplifier signal is demodulated will need to be generated. Due to the fact that the output has a phase shift w.r.t. the generated carrier signal, the square wave will need to take this phase shift into account. Figure 4.32 shows the filtered output signal for various relative phase shifts between the modulated signal and the square wave.

The effect of square wave phase misalignment
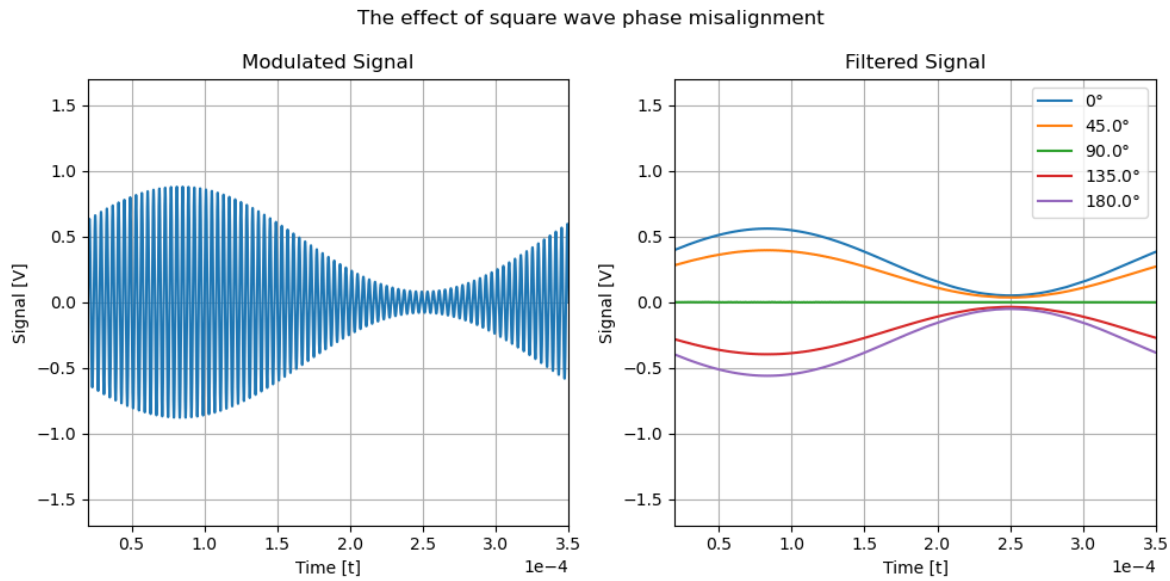
Figure 4.32: Impact of different phase shifts between the carrier and demodulation signals.

Due to the fact that the phase shift of the TIA is known for a theoretical system and can be easily determined for a real system, it is possible to generate the square wave such that this phase shift is accounted for. Generating analog sin waves and precisely phase shifted square waves is not a simple feat. For this research a commercial off-the-shelf signal generator will be utilised to generate these signals. See Section 7.3.3, where the future development plans are presented, including on-board signal generation.

Switching

In order to switch between $V_{in,1}$ and $V_{in,2}$ in equation (4.21) a single pole double throw mux can be utilised. These components are readily available and offered by a variety of manufacturers, for this design the *74LVC1G3157GV-Q10H* will be utilised.

Low Pass Filter

The low-pass filter should filter out all of the carrier frequency harmonics. The maximum frequency of the relative component will be $N\omega_{rw} = 36 \cdot \frac{5000rpm}{60} = 3000Hz$, whilst that of the absolute is 83 Hz. Filtering out the even harmonics of the carrier is done by applying a low-pass filter.

Requirement *HT_ENC_01* specifies the required accuracy of the encoder, which can be used to determine the requirements for the final low-pass filter in the demodulation chain. Tables 4.4 and 4.5 give the requirements for the low pass filter. The filters must have a cutoff frequency greater than the *maximum frequency*. The combination of phase shift and suppression of the carrier must be such that the required resolution is met.

Resolution	12	bit
Repetitions	36	-
Resolution/Repetition	114	-
Maximum Frequency	3000	Hz
Required Suppression	-41.12	dB
Maximum Phase Shift	1.58	deg

Resolution	8	bit
Repetitions	1	-
Resolution/Repetition	256	-
Maximum Frequency	83	Hz
Required Suppression	-48.17	dB
Maximum Phase Shift	0.7	deg

Table 4.4: Relative Component Filter Requirements

Table 4.5: Absolute Component Filter Requirements

In order to keep the design simple a passive filter is used. The LC Pi filter in Table 4.6 fulfills the requirements for both and consists of available components. Figure 4.33 contains the filter, with component

values in Table 4.6. The filter response can be seen in Figure 4.34.

L	1	mH
C	0.1	µF
Suppression	-49.4	dB
Phase shift	0.021	deg

Table 4.6: Component values for LC Pi Filter
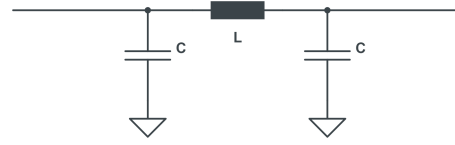
Figure 4.33: LC Pi Filter

4.7. Post-Processing

The final step in the chain of the encoder is to use an ADC to sample the four signals (two sets of two quadrature components) from both the absolute and relative components of the encoder. Before these components can be converted to a reaction wheel angle, the signals will need to be processed. This section will describe the signal processing performed.

First, the DC component of the signals is removed. Depending on the phase shift between the demodulation signal and the excitation signal the filtered output will either be above, or below the amplifiers common mode level. This DC offset will be constant for a given encoder unit and can be determined by averaging the signal over a long period of time. Equation (4.22) demonstrates this process, where S represents any of the four encoder output signals.

$$S_{ac} = S_{dc} - \overline{S_{dc}} \quad => \quad \overline{S_{dc}} = \frac{1}{n} \sum_{k=1}^{n} S_k \tag{4.22}$$

Second, the signals are remapped to $[-1, 1]$ using Equation (4.23).

$$S_{norm} = \frac{S_{ac}}{A_{ac}} \quad => \quad A_{ac} = \frac{max(S_{ac}) - min(S_{ac})}{2} \tag{4.23}$$

Finally, equation (4.24) can be used to determine the angular position of the wheel. S_q and S_i being the two channels.

$$\theta_{rw} = atan(\frac{S_q}{S_i}) \tag{4.24}$$
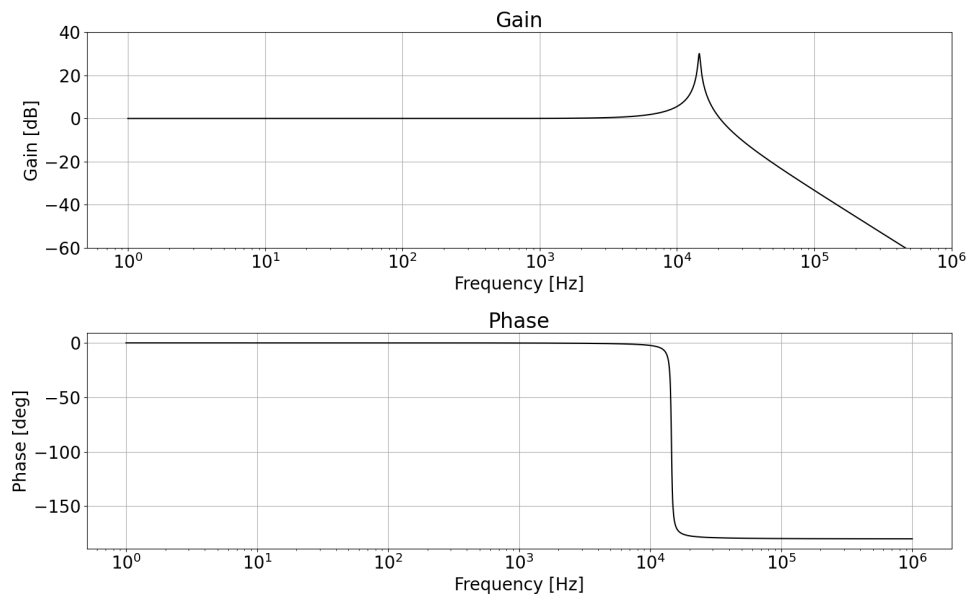
Figure 4.34: Bode plot for the AM demodulation low-pass filter

4.8. Sensitivity Analysis

With a design locked in for the capacitive sensing encoder a sensitivity analysis can be performed. The purpose of this analysis is to determine what the impact is of variations on the design due to external factors such as component variations, production tolerances and mechanical misalignments.

4.8.1. Component Variation

The circuit in Figure 4.12 contains all of the "components" present in the system. Other than the gain capacitor and resistor above the amplifier all the other components are part of the amplifier design, variations of these non-real components are treated in Section 4.8.2. This section will cover the influence of variation in the gain capacitor and resistor.

Based on Eq. (4.8), under the assumption that A_{amp} is very large, the output of the TIA scales with impedance Z_a, which is equal to $\frac{1}{1/R_a + sC_a}$. Given that the resistance of R_a will be very large, this component will eventually divide out and one is left with $\frac{1}{sC_a}$. This makes the design highly susceptible to changes in gain capacitance C_a. For the current design a value of $1pF$ is assumed, which in reality is a difficult value to attain due to stray capacitances.

When assessing the performance under variations in C_a, one can look at Eq. (4.16). The noise components and signal component scale in a similar fashion with Z_a (except for $V_{n,op}$), meaning the SNR should remain similar.

With the post-processing presented in Section 4.7 the design also allows for variations in gain between the channels due to normalisation. Given that performance is expected to remain similar and that any offsets and biases can be corrected for, this will not be investigated further.

4.8.2. Production Tolerances & Mechanical Misalignments

When producing the encoder there are various locations where production problems and misalignments will yield changes in the encoder performance. Due to the selection of a continuously varying pattern, any variations in pattern shape should have a minimal impact on the encoder performance due to the fact that data post-processing can be used to mitigate these problems. Aside from encoder production, mechanical misalignments such as positioning of the rotor PCB with respect to the stator PCB will never be perfect, meaning offsets are to be expected. In order to determine the impact of these offsets, a set of simulations were run:

1. Radial offset between rotor and rotor pcb
2. Radial offset between rotor shaft and stator pcb
3. Variance in rotor pcb - stator pcb spacing over a single rotation

In reality a combination of all of these offsets will occur, but in order to gain an understanding their effects are modeled separately. This section will present plots of the amplitude modulated outputs of the capacitive sensing amplifier. This means that they are *before* the amplitude demodulation.

Radial offset between rotor and rotor pcb

When the rotor and rotor pcb are misaligned this means the center of rotation of the rotor itself is still aligned to the stator pcb axle, but the rotor pcb is not rotating about its center. Two extreme cases of this misalignment are shown in Figures 4.35 and 4.36, where the rotor pcb is radially misaligned by 3 mm. Both of these cases were simulated and the results are presented in Figures 4.37 and 4.38. The following effects are observed:

Reduction in modulation depth

Due to the excitation electrode partially overlapping with the sensitive electrodes the 'zero-level' for the entire encoder chain is lifted, resulting in a reduction of the modulation depth.

Distortion of the output signal
Most visible in the absolute component, the partial overlap between the excitation electrode and the sensitive electrodes causes a distortion of the output signal. This is caused by the fact that under these conditions, the excitation electrode also 'moves' instead of just rotating around it center. The relative component suffers from this distortion less due to the fact that its channels are 'averaged' over many surfaces, whilst for the absolute encoder there is only a single surface per channel.

Signal Rounding
Figures 4.39 and 4.40 compare the output for a single channel. The output signal of the encoder is 'carried' on top is this channel. From this one can deduce that the output signal has some rounding in the bottom.
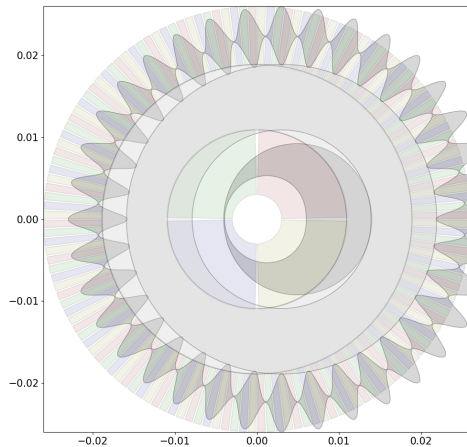
Figure 4.35: Encoder radially shifted by 3mm
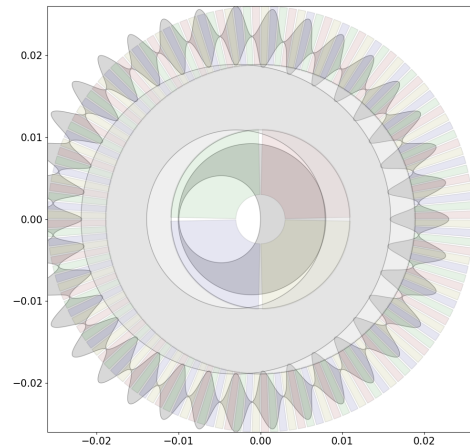
Figure 4.36: Encoder radially shifted by -3mm
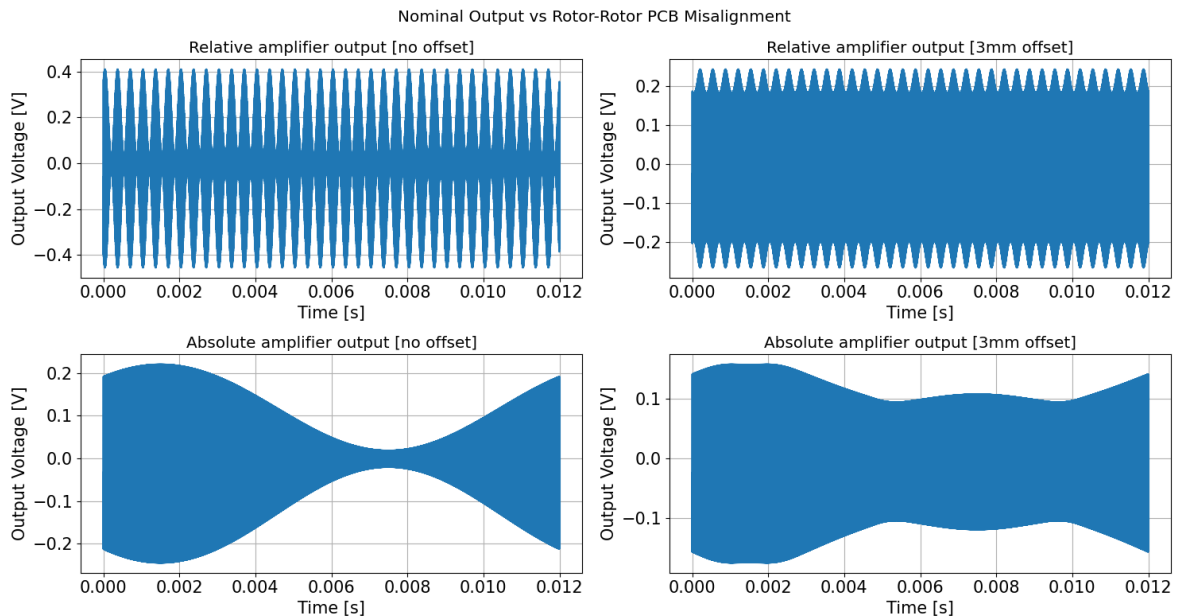
Figure 4.37: Capacitive sensing amplifier output for a rotor pcb - rotor misalignment of 3mm
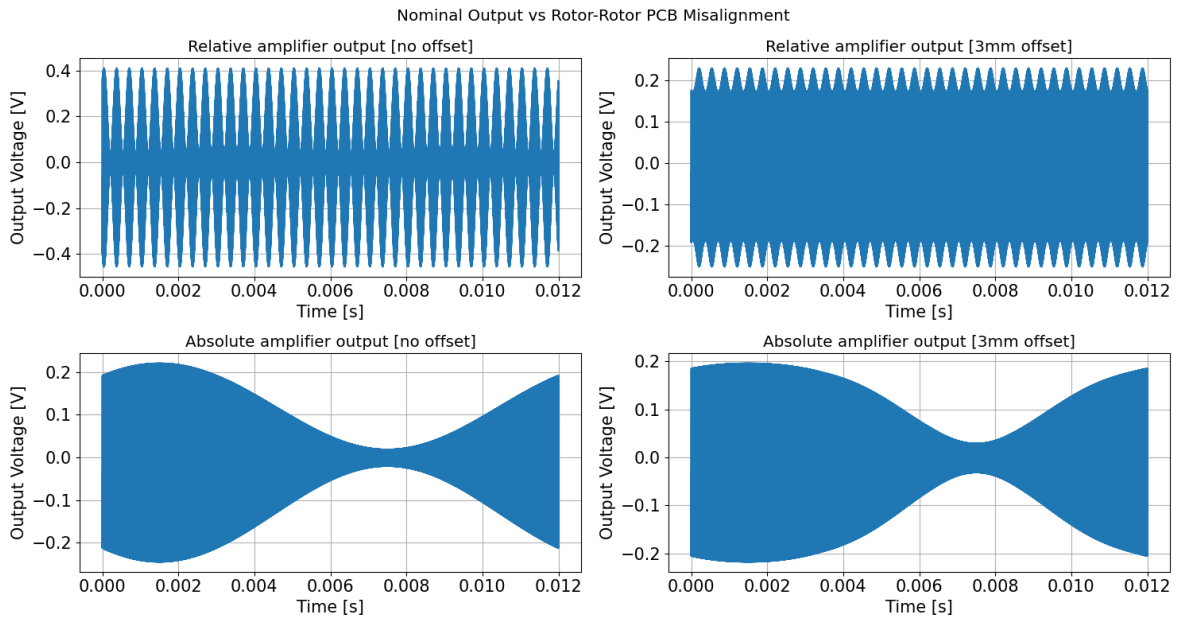
Figure 4.38: Capacitive sensing amplifier output for a rotor pcb - rotor misalignment of -3mm
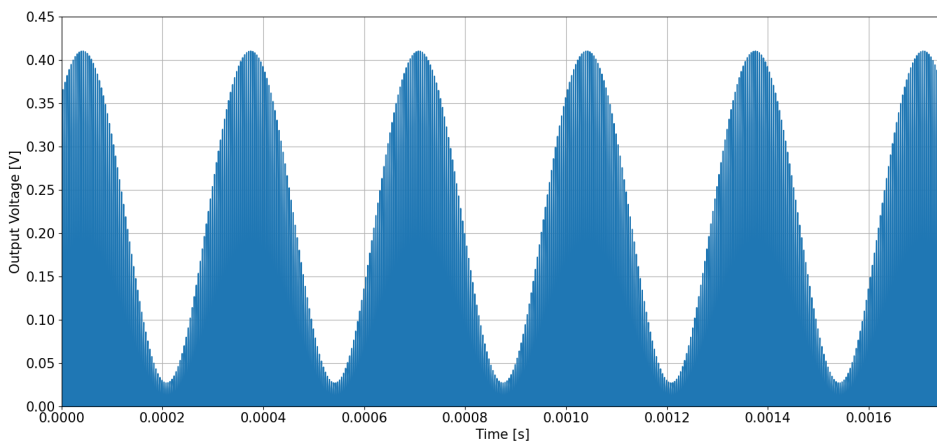
Figure 4.39: Relative encoder channel AM output
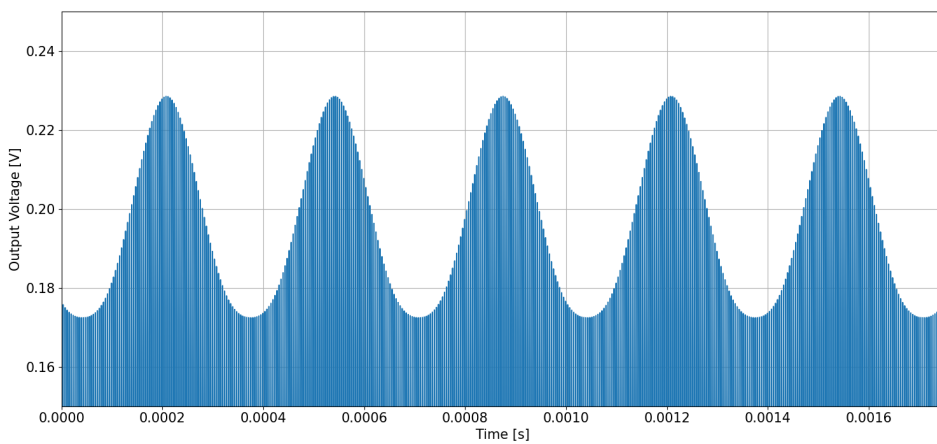
Figure 4.40: Relative encoder channel AM output with rounding due to offset

Radial offset between rotor and stator

When the rotor and stator are misaligned the axes of rotation are not in the same location. This displacement appears the same as Figure 4.35 or 4.36, but instead of rotating around the origin, the rotor PCB will rotate about its center (offset by 3mm from the stator). This effect is simulated in Figure 4.41. The following effects are observed:

Reduction in modulation depth

Due to the exact reason as in Section 4.8.2 the modulation depth is reduced.

Gain variance over a single rotation in the relative channel

Gain variance in the encoder output is expected, it is the main principle of operation for the encoder. However for the relative component one would expect that the gain variations for every $1/36^{th}$ of a rotation are the same. With this type of radial misalignment however this is not the case. The root cause of this is the fact that part of the absolute encoder *sensitive electrode* now overlaps with the excitation electrode. This causes C_0 to vary in size depending on the position of the wheel and thus the output of the encoder. This effect is visible on the absolute component as well, but there it simply works in an additive manner.

Signal Rounding

Similar as before, signal rounding occurs.
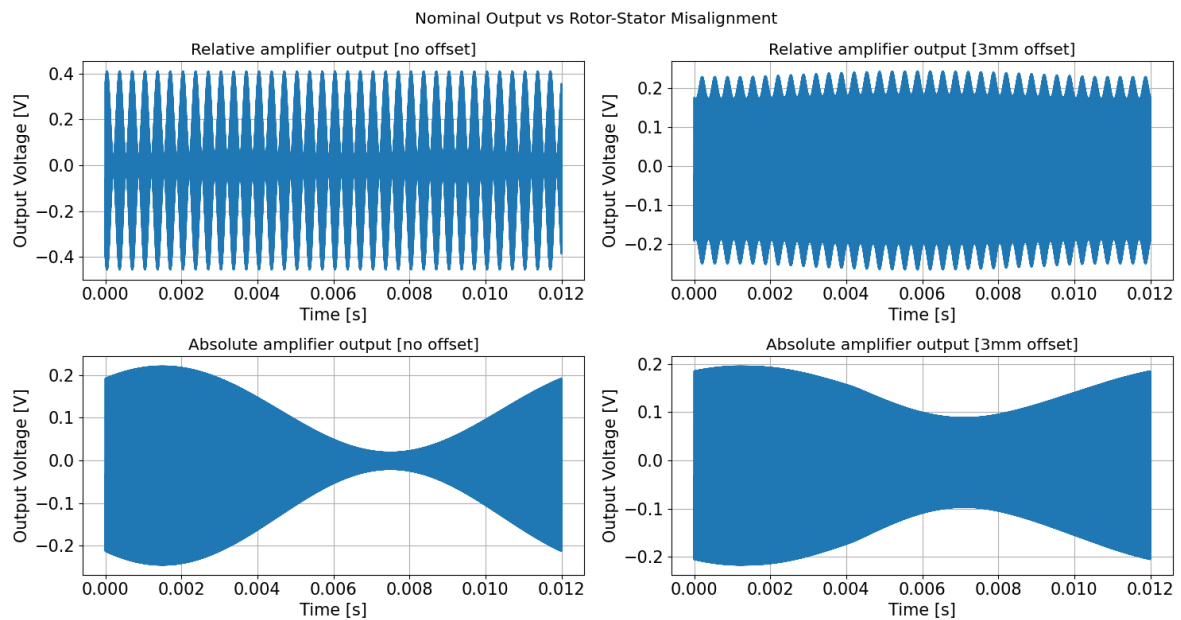
Figure 4.41: Capacitive sensing amplifier output for a rotor - stator misalignment of 3mm

Variance in electrode gap

In the case of a crooked bearing or any other type of misalignment it is possible that there is a variance in the gaps between PCBs over a single rotation. In order to model the effects of this a variance of 0.2mm on a gap of 1mm is simulated. This gap is applied based on wheel position θ.

$$\delta_{elec} = 1 + 0.1sin(\theta)$$

The results can be seen in Figure 4.42. The only effect observed here is a variation in gain over a single rotation, which is expected based on Equation (3.1).
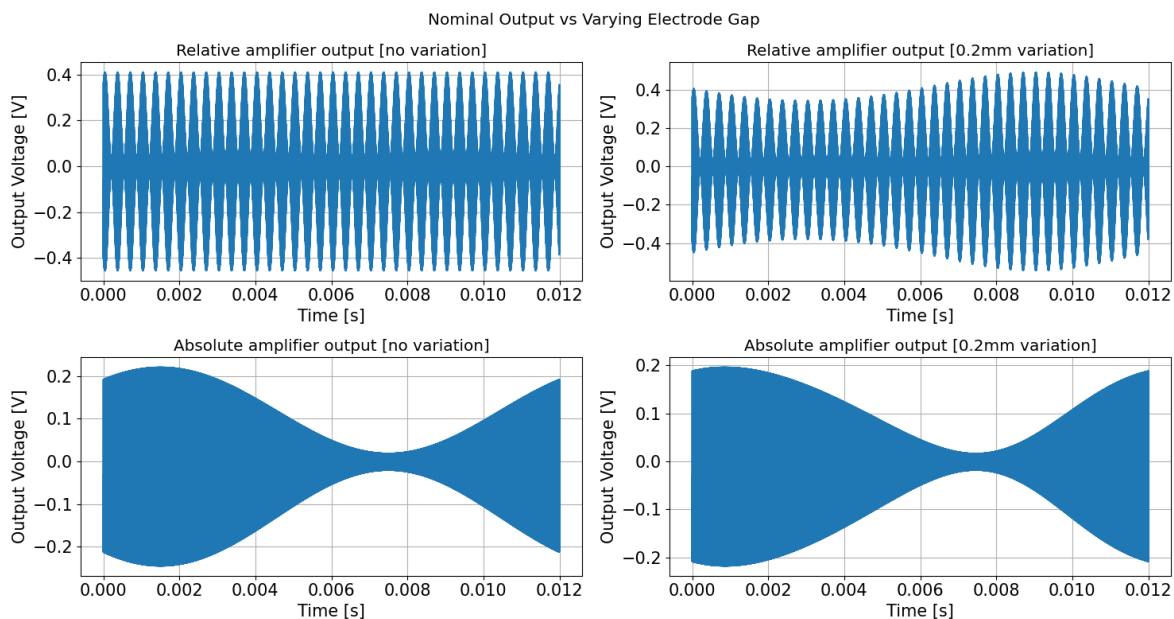
Figure 4.42: Capacitive sensing amplifier output for sinusoidal variance of pcb gap of 0.2mm

4.9. RQ4: What would a design of sensor feedback on the reaction wheel entail?

In this chapter the design of a capacitive sensing encoder fit for reaction wheels has been shown. This encoder will improve state estimation of the reaction wheel and allow for the implementation of a more advanced controller. The over-all design concept can be seen in Figure 4.4. The design consists of three distinct stages: capacitive sensing, AM demodulation and post-processing. In order to allow for power-cycle tolerance, the design elaborated below is used twice, in order to provide a coarse absolute measurement and a finer relative measurement.

The capacitive sensing part of the encoder chain takes the excitation signal, passes it through varying plate capacitors and converts this to a differential output voltage which scales with the amount of overlap. This encodes the position of the reaction wheel into a quadrature signal, representing the real and imaginary components in a rotating phasor diagram. By feeding this signal through a pair of differential amplifiers an AM signal is generated containing these quadrature components.

The signals exiting the two differential amplifiers contain a high-frequency component (excitation signal) and modulated upon it a low-frequency component (amplitude variations due to a varying location of the rotor). The excitation signal is filtered out by multiplying the output signal of the encoder with a square wave at the same frequency as the excitation signal, utilising a SPDT switching device. This signal is then filtered to remove any of the high frequency components, yielding two signals that encode the reaction wheel position.

This signal is digitized through the utilisation of an ADC. The digital signals are then normalised to a range of (-1,1) and Eq. (4.24) is then utilised to convert the output to the reaction wheel angle θ_{rw}.

5

Prototype Development

In the previous Chapter an amplifier topology was selected, encoder wheel shape was optimised and a general design was presented. This chapter contains the development of a real-life prototype to verify the research performed up to this point. Section 5.1 contains a selection of real-life components which can be used. Section 5.2 contains an early prototype which was produced to validate the concept, followed by Section 5.3 presenting the final prototype which was used for the verification campaign.

5.1. Component Selection & Operating Frequency

The amplifier model shown in Figure 4.12 has three components that will need to be selected: R_a, C_a and the amplifier.

Bias Resistor R_a

The bias resistor R_a allows the input bias current of the amplifier to flow. The greater the value, the greater Z_a in equation (4.8), thus the higher the gain of the amplifier. A higher value is preferable, *until* it is no longer capable of supplying the amplifier bias current.

$$R_{a,max} \approx \frac{V_{sig,rms} - V^-}{I_{bias}} \tag{5.1}$$

The maximum value for R_a is given by equation (5.1). V^- can be assumed to be 0. Bias currents are in the *pico* Ampere range (10^{-12}) and $V_{sig,rms}$ will be in the 0-1V range. Concluding from this the value for $R_{a,max}$ is not limited by the bias current, but rather the availability of components. Selecting a practical, readily available resistor yields a maximum resistor value of 10M.

Amplifier Capacitor C_a

Capacitor C_a, similar to resistor R_a sets the gain of the amplifier, however for C_a the lower the value, the higher the gain of the amplifier. The most limiting factor here will be the stray capacitances from the PCB defining a lower limit for the capacitance value. Due to the fact that this is near-impossible to determine in advance, for now a value of $1pF$ is assumed, which provides an output gain that is measurable (500 mV p-p) and can be purchased.

Operating Frequency

The operating frequency is the frequency at which the input signal V_{sig} is generated. The Bode plot in Figure 4.14 indicates that the combined system has a cut-off frequency around 50 kHz, causing the gain to 'taper off' around 250 kHz. In order to perform AM Demodulation further down the chain, two signals will need to be generated very precisely, which is simpler to do at lower frequencies. As such an operating frequency of 250 kHz is selected.

Amplifier Selection

In Section 4.4 it was established that the design will be performed with a single-ended amplifier setup in order to simplify the design, and then a differential setup will be used in the final design. For more information, see Section 7.2.8. In order to accomplish this a differential amplifier must be selected.

Selecting the amplifier is done by determining which specifications of the amplifier are important and utilising those to perform a trade-off. Due to the fact that the operating frequency is 250 kHz, which is a relatively low frequency, factors such as gain-bandwidth product and slew rate are not limiting when comparing amplifiers. Most amplifiers available on the market have gain bandwidth products and slew rates that are sufficient for this design. One distinguishing factor that *does* influence performance of encoder is the noise generated by the amplifier.

Equation (4.13) contains two noise components related to the amplifier, $I_{n,op}$ and $V_{n,op}$. Contributions of both components follow the same relation, with one exception, the voltage noise components is divided by Z_{d2}. Because $Z_{d2} = 0 + \frac{1}{sC_2}$ the contribution is related to the value of capacitance C_{d2}, which is in the pF range. From this it can be concluded that the input-referred current noise contributes more than the input-referred voltage noise.

Utilising the simulation set up in this Section various amplifiers were considered. Given that the selection of differential amplifiers is rather limited, only two amplifiers have a sufficiently low $I_{n,op}$: the LTC1992 from Analog Devices and the THS413x from Texas Instruments. Both amplifiers are very similar in specifications and are even pin-compatible with one another. Whilst the THS413x has a lower input-referred voltage noise ($1.3\ nV/\sqrt{Hz}$ vs $35\ nV/\sqrt{Hz}$) [25, 42], after initial testing it was discovered that its limited output range makes it non-suitable for this type of encoder due to the output clipping. For that reason the LTC1992 will be utilised, which has a rail-to-rail output.

GBP	3.2	MHz
Slew Rate	1.5	$V/\mu S$
Input Referred Voltage Noise	35	$nV/\sqrt{Hz}$
Input Referred Current Noise	1	$fA/\sqrt{Hz}$

Table 5.1: LTC1992 Specifications [25]

5.2. Early prototype

In order to verify the amplifier topology and provide an early proof of concept before developing the full PCB an early prototype of a single channel was produced, which can be seen in Figure 5.1.
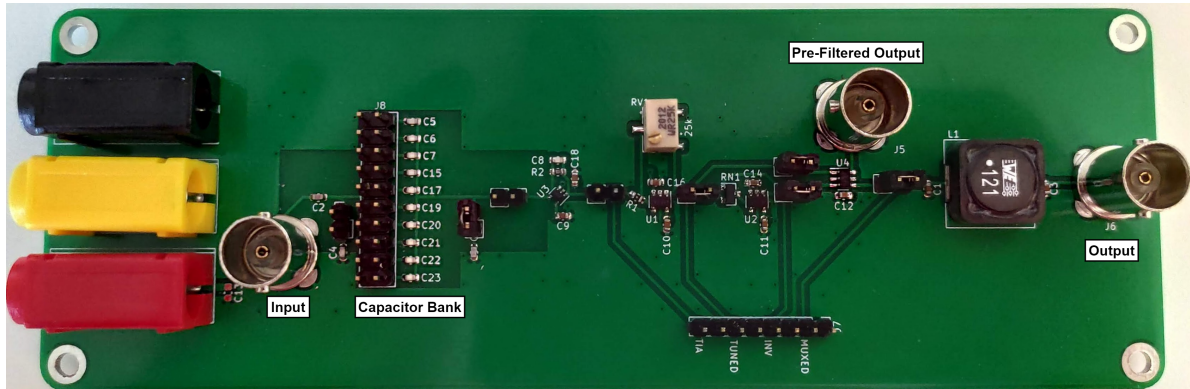
Figure 5.1: Full Chain Test PCB

In order to test the trans-impedance amplifier a sine-wave was injected into the input and the capacitance was varied by making use of the bank of jumpers which can be seen on the left of the board.

The capacitor values of C5-C23 are 0.1 pF, in practice the capacitance varied per capacitor due to the physical placement and stray capacitances. Due to this fact the verification of the amplifier topology is qualitative, not quantitative.

Figure 5.2 shows the output of the TIA for a varying number of jumpers. The plot shows that the amplitude of the sin wave is correlated with the capacitance inserted by the jumpers.
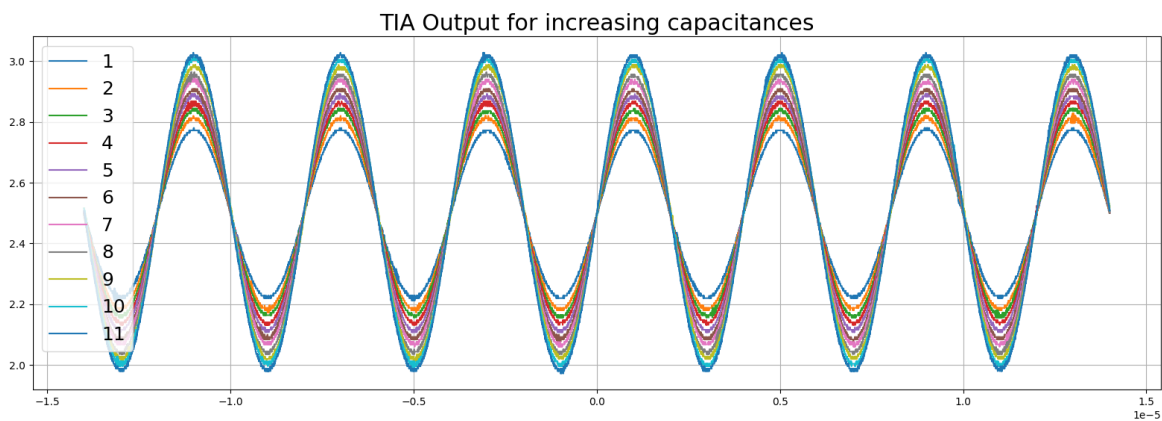
Figure 5.2: Measurement results of the TIA Verification (in Volt) $V_{in} = 5Vsin(250k)$, $V_{offset} = 2.5V$, measured with a Siglent SDS1104X-U Oscilloscope

From the development, production and testing of this prototype three main lessons were learned, which are taken into account for the design of the final prototype:

1. **Coupled in Noise**
   The capacitance at the input of the TIA was very susceptible to the location of the PCB w.r.t. the ESD mat and any touching of the components by hand. Part of this was due to the fact that the design omitted (on purpose) a ground plane underneath the capacitor bank, which allowed external noise to couple in more easily.

2. **Stray Capacitance**
   When none of the capacitor jumpers were connected, there was still a signal coming through, which can be attributed to stray capacitances on the board. Whilst this does not seem to affect the functionality of the board greatly, it could come with a performance penalty in the final board. The manifestation of this problem is in a non-zero output of the TIA when none of the jumpers are connected.

3. **Bias Resistor**
   Bias resistor R_a has an influence on the operation of the amplifier. In the initial design 10M was selected, however in reality this value was too high, since the output of the amplifier was clipped to a single value. By lowering the resistor value step-by-step a point was found where the amplifier no longer clipped, whilst simultaneously not losing a great deal of output gain. The final value of this resistor is $1M\Omega$.

5.3. Final Prototype

The design of the final prototype is the same as the design presented in Chapter 4, with the lessons taken from the early prototype taken into account. The stator PCB can be seen in Figures 5.3 and 5.4. Due to the fact that the collection electrodes of the relative component surround the center and the fact that four layers are required to provide the connections between the collection electrodes and the amplifiers, a separate spreader PCB is used as a bridge. The spreader (Figure 5.5) connects to the absolute encoder components and provides the excitation signal, demodulation signal, power and ground connections.
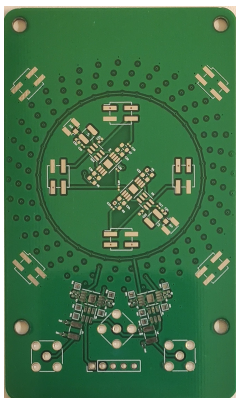
Figure 5.3: Stator PCB top side   Figure 5.4: Stator PCB bottom side   Figure 5.5: Spreader PCB
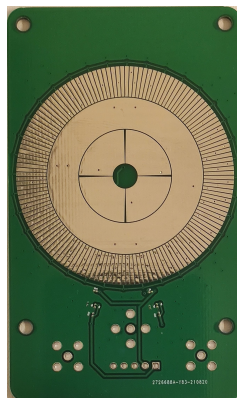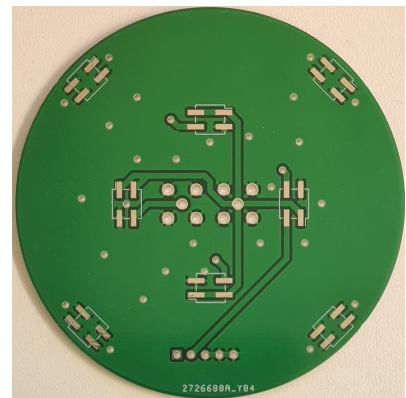
The final stator prototype with all components populated and external connections can be seen in Figure 5.6, along with the rotor PCB prototype in Figure 5.7. These PCBs together form the final prototype, which is used in combination with a test setup to test and verify the design of the capacitive encoder.
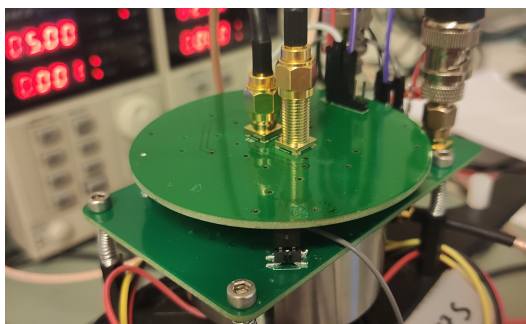
Figure 5.6: Final stator prototype with all connections   Figure 5.7: Final rotor prototype

6

Testing & Verification

Testing the final prototype presented in Section 5.3 will allow for verification of the design and testing of the encoder performance. Sections 6.1 and 6.2 will present the testing plan and setup respectively, followed by Section 6.3 which characterises the test setup and will aid in tuning encoder performance in Section 6.4. Finally the results are presented in Section 6.5, followed up with an answer to the final research question, RQ5 in Section 6.6.

6.1. Test Plan

The test plan for the reaction wheel encoder is described below:

1. **Tuning the System**
   Given that many of the calculations in Chapter 4 were based on a single-ended amplifier topology, combined with the fact that models are not the same as reality, the input parameters of the encoder will require tuning. The parameters that are tuned:

   - Excitation Frequency
   - Excitation Voltage
   - Demodulation square wave phase shift

2. **Verifying the Accuracy Requirement**
   Verifying requirement HT_ENC_01 by stepping the encoder wheel with a stepper motor and measuring the change in output.

6.2. Test Setup

In order to verify proper operation of the reaction wheel encoder and tune the settings an automated test setup is created. Figure 6.1 contains a block-diagram explaining the test setup.
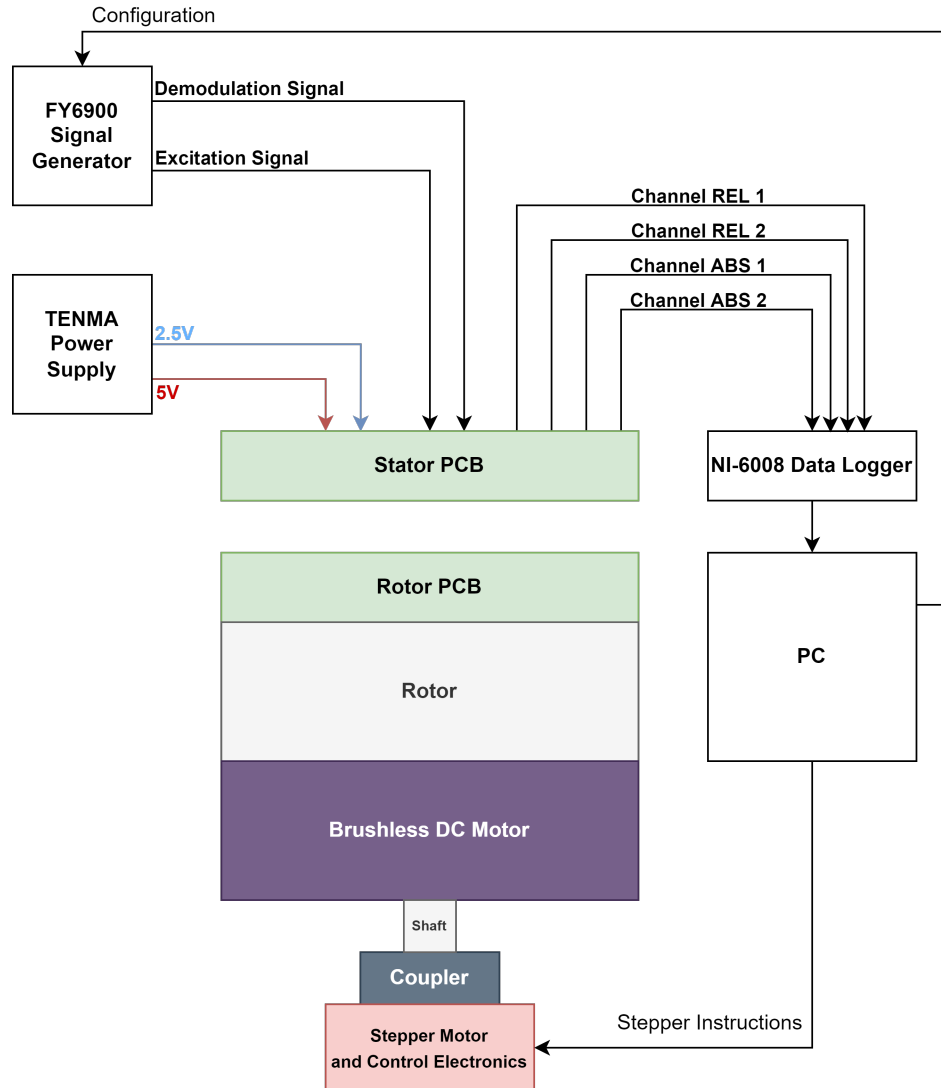
Figure 6.1: Test setup for the reaction wheel encoder

The FY6900, NI-6008 data logger and stepper motor electronics are all connected to a PC through USB. The PC will run a script that configures the testing conditions on the FY6900, tells the stepper electronics to step and then logs the output using the NI-6008 data logger. The stepper motor utilised is a NEMA 17 with a $(5 + \frac{2}{11})to1$ gearbox. The NEMA17 by default has a resolution of 200 steps/revolution. Utilising micro-stepping (1/16th) on an A4988 board will give a minimum step size of:

$$\delta\Theta = \frac{360°}{200 * (5 + 2/11) * 16} = 0.0217°$$

This is sufficient to validate the accuracy requirement *HT_ENC_01*.

6.3. Setup Characterisation

No test setup is perfect and as such neither will the one described in the previous section. The test setup contains 3D printed components and is driven using a stepper driver without feedback. Furthermore, the encoder itself might have inherent biases based on assembly accuracy and/or design.

Given that in an integrated encoder any biases and offsets can be corrected for in software, this process can be applied to the gathered data from the testing setup as well. Section 4.8 has highlighted some of the offsets that can be introduced due to incorrect assembly and/or component variation. To get a deeper understanding into what is occurring in the test setup, Appendix A will contain more information on characterising these biases/offsets.

Figure 6.2 contains the output of the encoder for a large sample size of rotations (25). The first two rows contain the ac-coupled output of the encoder. The error plot on the third row highlights the deviation of the encoder output with respect to an assumed perfect stepper motor after the post-processing from Section 4.7 is applied. The fourth row contains this same error plot, but with any detectable bias removed.

Please note that while the relative component plots here look similar to those in the simulations like Figure 4.37 for example, these represent something different. That plot contained the amplitude modulated signal for a single rotation, Figure 6.2 contains the demodulated signal for 25 repetitions. Due to the variations in gain over a single rotation however, these plots end up looking similar.
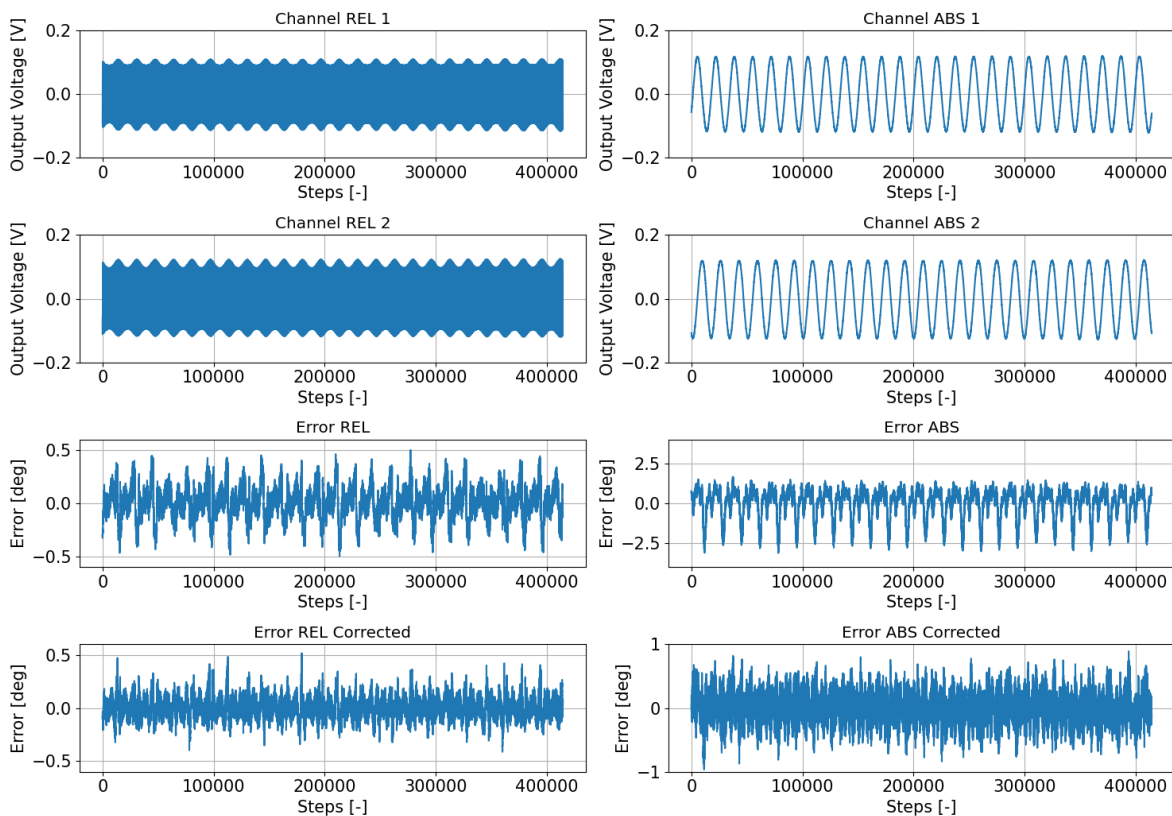
Figure 6.2: Initial run of the encoder, 25 repetitions.

The removal of the output bias is achieved through determination of the bias, interpolation, and correction. Figure 6.3 plots the errors (δ) with respect to the encoder positions (θ). Corrections can be performed in many ways, such as for example a polynomial fit (visible here) or a Look-Up Table (LUT), this is further covered in Section 7.2.3. Table 6.1 presents the Standard Deviation (STD) of the error pre- and post correction.

The first plot contains the absolute component error vs the absolute component position. There is a clear correlation between the encoder error and the encoder position. Determining this correlation and subtracting the result from the absolute encoder yields an improvement in STD by 0.728°.

The second plot contains the relative component error vs the *corrected* absolute component position. Once again, a correlation exists. Determining it and subtracting the results yields an improvement in STD for the relative encoder of 0.048°.

The third plot contains the *corrected* relative component error vs the *corrected* relative position. This final correlation removes any offsets that are only present in the relative component and not the absolute. Whilst a small correlation seems to exist, at this point diminishing returns are reached and the improvement in STD is negligible (presented in the final plot). Because this improvement is negligible **this step is not used in future data processing**.
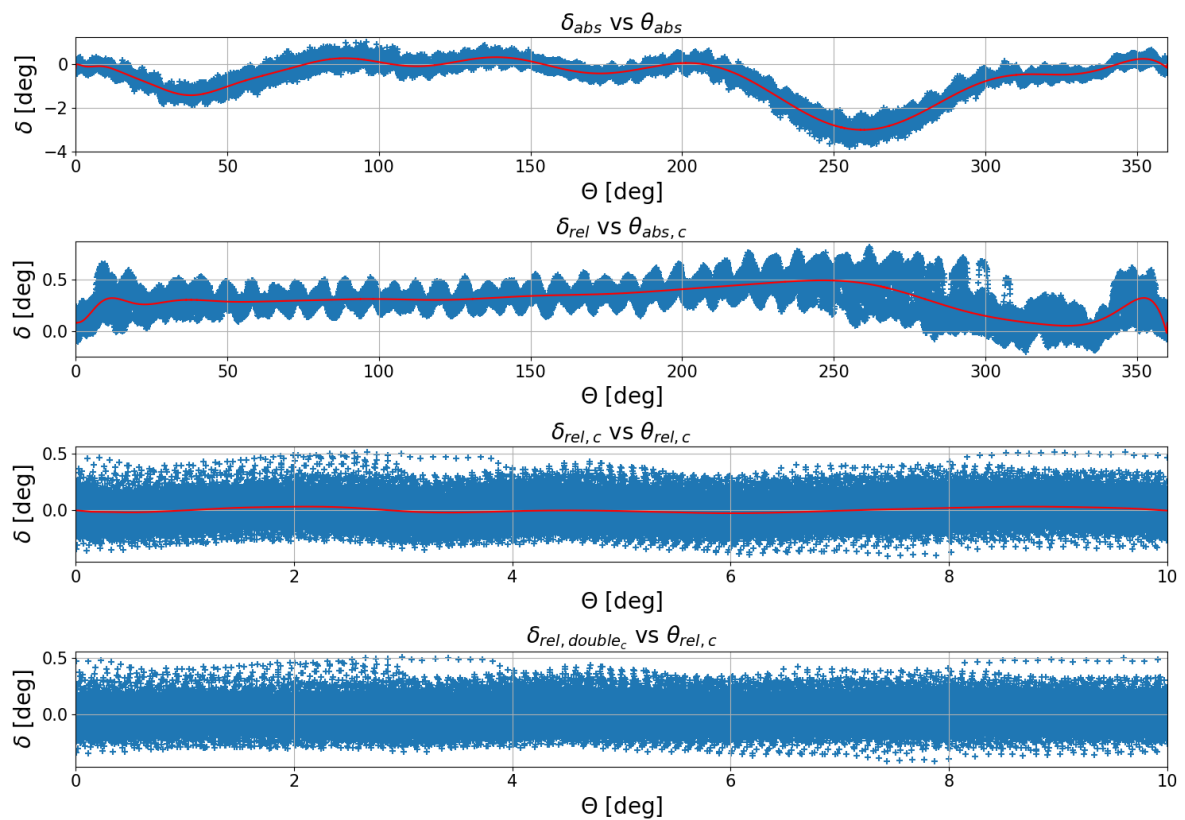
Figure 6.3: Correlation between encoder position and encoder error

Error	Initial STD [°]	Post-Correction STD [°]
δ_{abs}	0.927	0.199
δ_{rel}	0.152	0.104
$\delta_{rel,c}$	0.104	0.102

Table 6.1: Error standard deviations pre- and post-correction

6.4. Tuning

In order to optimise the operating conditions of the prototype and verify the theoretically determined operating conditions in Section 5.1, the prototype is sequenced through a sweep of tests. There are three parameters that can be tuned:

1. Excitation signal frequency (operating frequency)
2. Excitation signal voltage
3. Demodulation signal phase shift

This section will contain the tuning process for all three. For the tuning process it is assumed that the three parameters can be tuned individually and iteration is used to verify this. It should be noted that because this is an iterative process, the figures should be interpreted for comparison between various settings, not for absolute reference. The corrections described in Section 6.3 are applied here.

Excitation signal frequency

Figure 6.4 presents the output of the full encoder system for a range of excitation signal frequencies. The left column contains the ac-components of the two relative encoder channels, followed up by the error between the calculated position and real position. The right column contains the same information but for the absolute encoder channels. Based on the results presented in Table 6.2 250 kHz appears to be the optimal frequency, here the combined (added) STD of the deviation w.r.t. the stepper motor position is minimal.
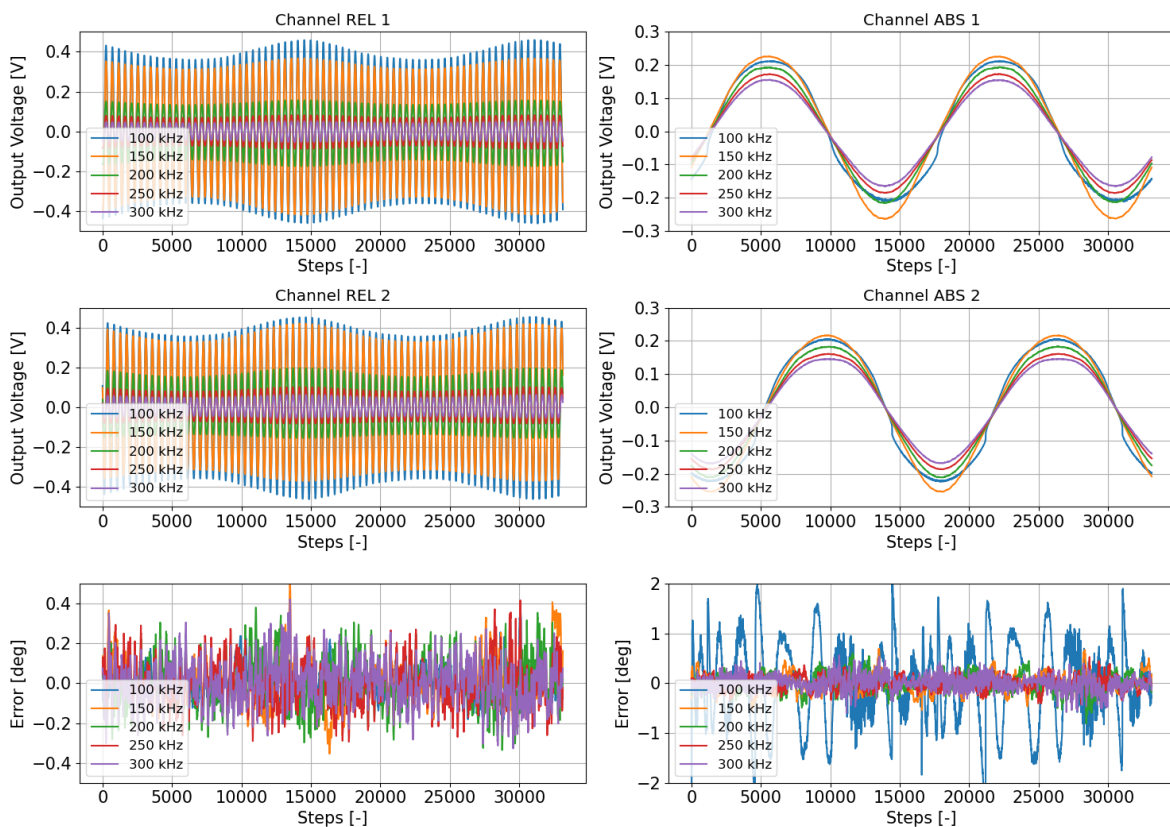
Figure 6.4: Two rotation encoder output for f_{exci} in the range of 100-350 kHz

Excitation Freq.		Excitation Amp.		Phase Shift		Relative Error STD		Absolute Error STD	
100	kHz	5.0	V	0	deg	0.079	deg	0.827	deg
150	kHz	5.0	V	0	deg	0.118	deg	0.183	deg
200	kHz	5.0	V	0	deg	0.121	deg	0.165	deg
250	kHz	5.0	V	0	deg	0.112	deg	0.127	deg
300	kHz	5.0	V	0	deg	0.110	deg	0.143	deg

Table 6.2: Encoder frequency sweep results for f_{exci} in the range of 100-350 kHz

Excitation signal voltage

Figure 6.5 presents the output for various excitation signal amplitudes and Table 6.3 tabulates the results. Two sweeps were performed, from a 1-5V sweep it was concluded that the optimal is between 2-4V, however the results were inconclusive, so a more precise run was executed. The lowest combined STD occurs for the excitation voltage of 3.5V.
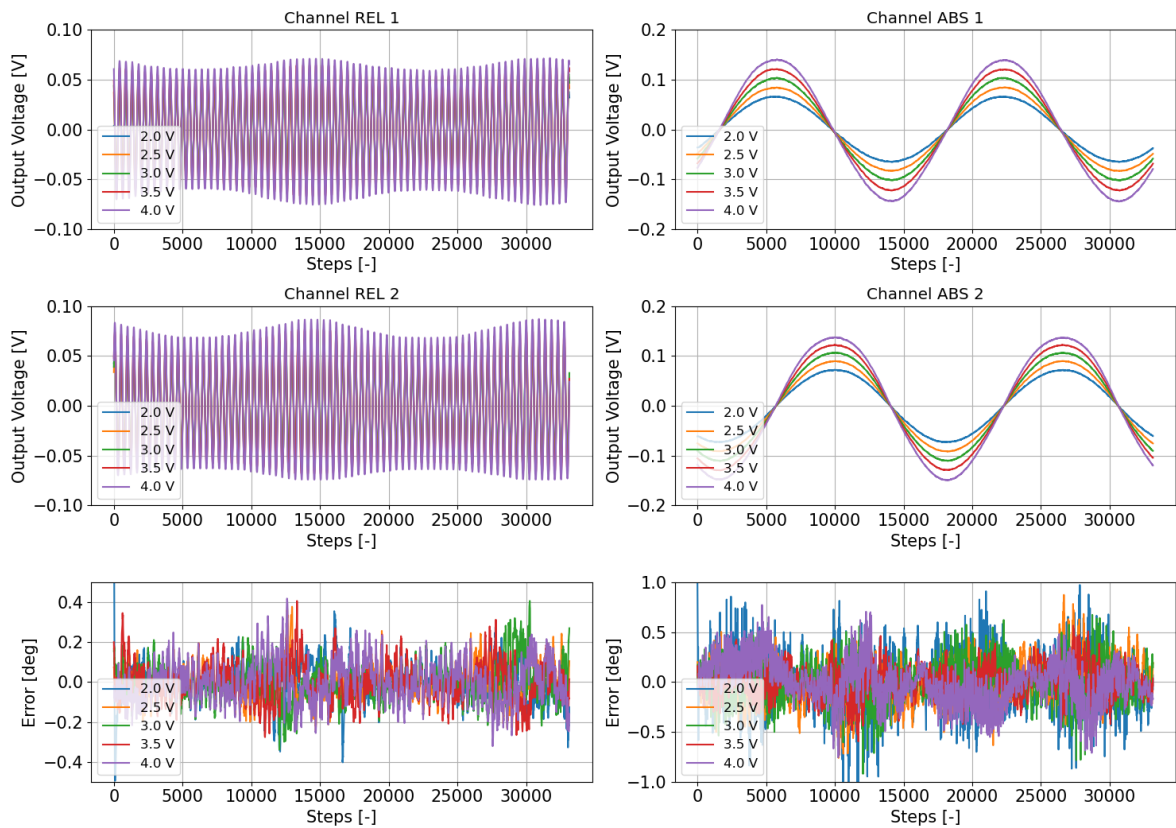
Figure 6.5: Two rotation encoder output for V_{exci} in the range of 2-4 V

Excitation Freq.		Excitation Amp.		Phase Shift		Relative Error STD		Absolute Error STD	
250	kHz	2.0	V	0	deg	0.103	deg	0.260	deg
250	kHz	2.5	V	0	deg	0.089	deg	0.201	deg
250	kHz	3.0	V	0	deg	0.098	deg	0.185	deg
250	kHz	3.5	V	0	deg	0.097	deg	0.158	deg
250	kHz	4.0	V	0	deg	0.104	deg	0.208	deg

Table 6.3: Encoder frequency sweep results for V_{exci} in the range of 2-4 V

Demodulation signal phase shift

The final parameter to be tuned is the phase shift between the excitation signal and the demodulation signal. Similar to previous tests, a sweep was performed, which can be seen in Figure 6.6. The results are also tabulated in Table 6.4. Due to time constraints (it takes about 1 hr to obtain one of these datasets) the sweep was performed in increments of 30 °. From these results it is concluded that the results are optimal for a phase shift of 30 °. Given that both 0 °and 60 °are worse performers than 30

°it is probably close to the optimum. In reality the optimum might be between 30 and 60 °, however the improvements are marginal (as seen by the value at 60 °).
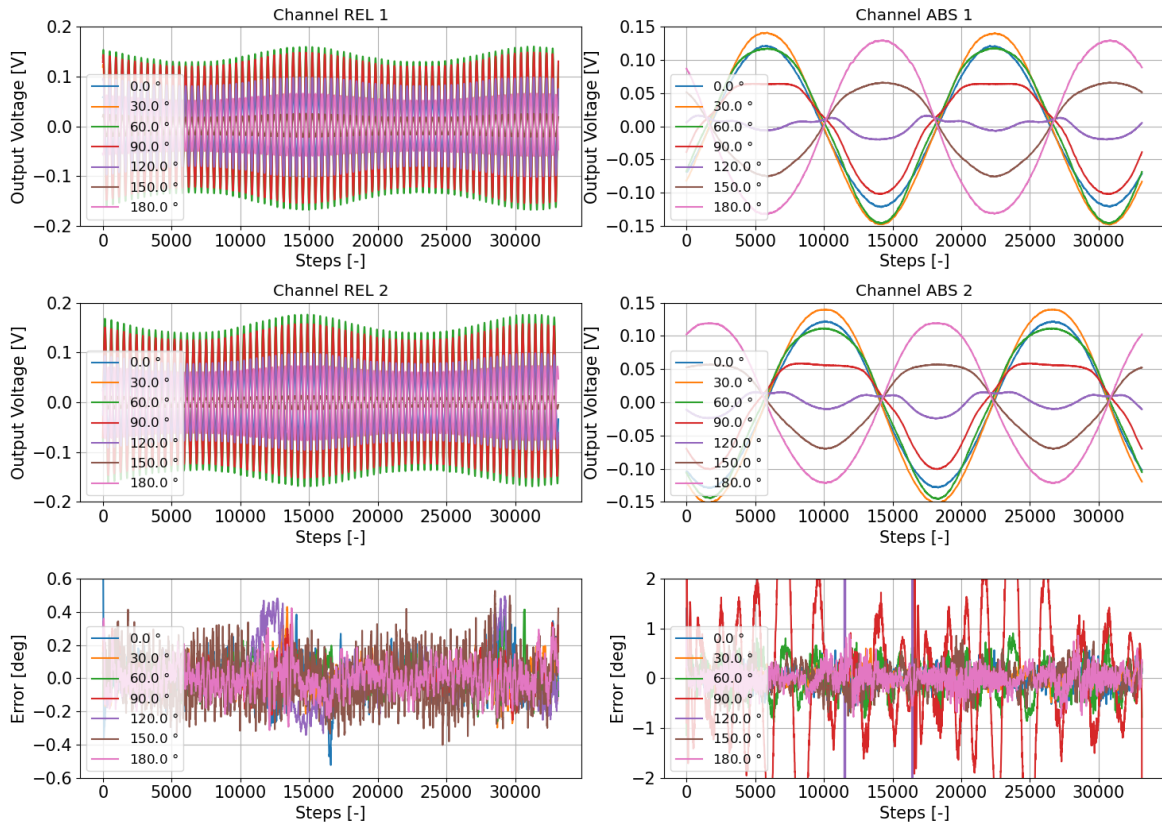
Figure 6.6: Two rotation encoder output for δ_{phase} in the range of 0-180 °

Excitation Freq.		Excitation Amp.		Phase Shift		Relative Error STD		Absolute Error STD	
250	kHz	3.5	V	0	deg	0.121	deg	0.177	deg
250	kHz	3.5	V	30	deg	0.093	deg	0.140	deg
250	kHz	3.5	V	60	deg	0.082	deg	0.341	deg
250	kHz	3.5	V	90	deg	0.097	deg	1.648	deg
250	kHz	3.5	V	120	deg	0.147	deg	186.443	deg
250	kHz	3.5	V	150	deg	0.143	deg	0.227	deg
250	kHz	3.5	V	180	deg	0.094	deg	0.194	deg

Table 6.4: Encoder frequency sweep results for δ_{phase} in the range of 0-180 °

6.4.1. Conclusion

In this section, through testing and iteration the optimal setting were found for the encoder, these settings are presented in Table 6.5.

Excitation Frequency	250 kHz
Excitation Amplitude	3.5 V
Modulation Phase Shift	30°

Table 6.5: Optimal encoder settings

The excitation frequency is exactly as determined previously, however it should be noted that performance of the relative component seems to be similar for almost any frequency between 100-300 kHz. The absolute channel does seem to have an optimum at 250 kHz.

The excitation amplitude optimum seems to be at 3.5V, rather than the expected 5V (which would max-imise SNR). The reason for this appears to be a non-linearity in the amplifier circuit, which behaves like soft clipping, where the output is rounded near the edges of the amplifier range. This effect looks similar to the rounding in Section 4.8, however that effect should not be dependant on the excitation amplitude (since it causes an inherent shape change on the encoder). The effect is demonstrated in Figure 6.7 and appears on all four (2x incremental, 2x absolute) channels of the amplifier.

Whilst it appears like soft clipping, the amplifier is not being operated near its limits (which is rail-to-rail, 0-5V). This subject is further discussed in Section 7.2.1.
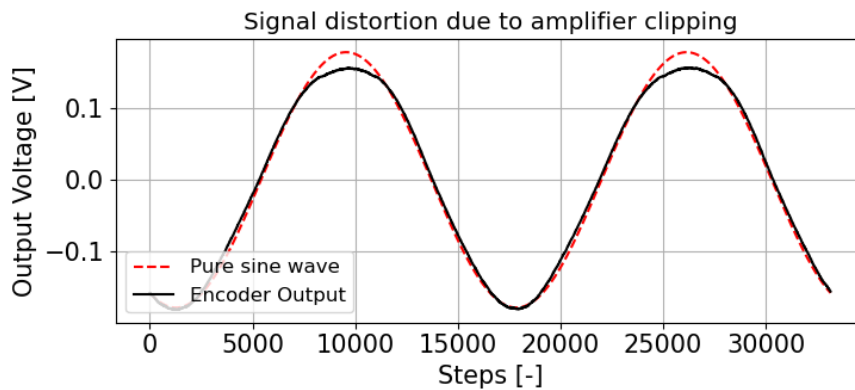
Figure 6.7: Clipping of the amplifier output

The modulation phase shift was a difficult to predict parameter beforehand, given that it is a combination of both the capacitive sensing and AM demodulation phase shift. However, it does appear like an optimal phase shift can be found where both amplifiers (absolute and relative) are performing well.

6.5. Final Results

In the previous sections the performance of the encoder has been tuned to optimise the accuracy. In order to verify whether the accuracy requirement is met a long run using the minimal step size is performed. The results of this run can be seen in Figure 6.8.
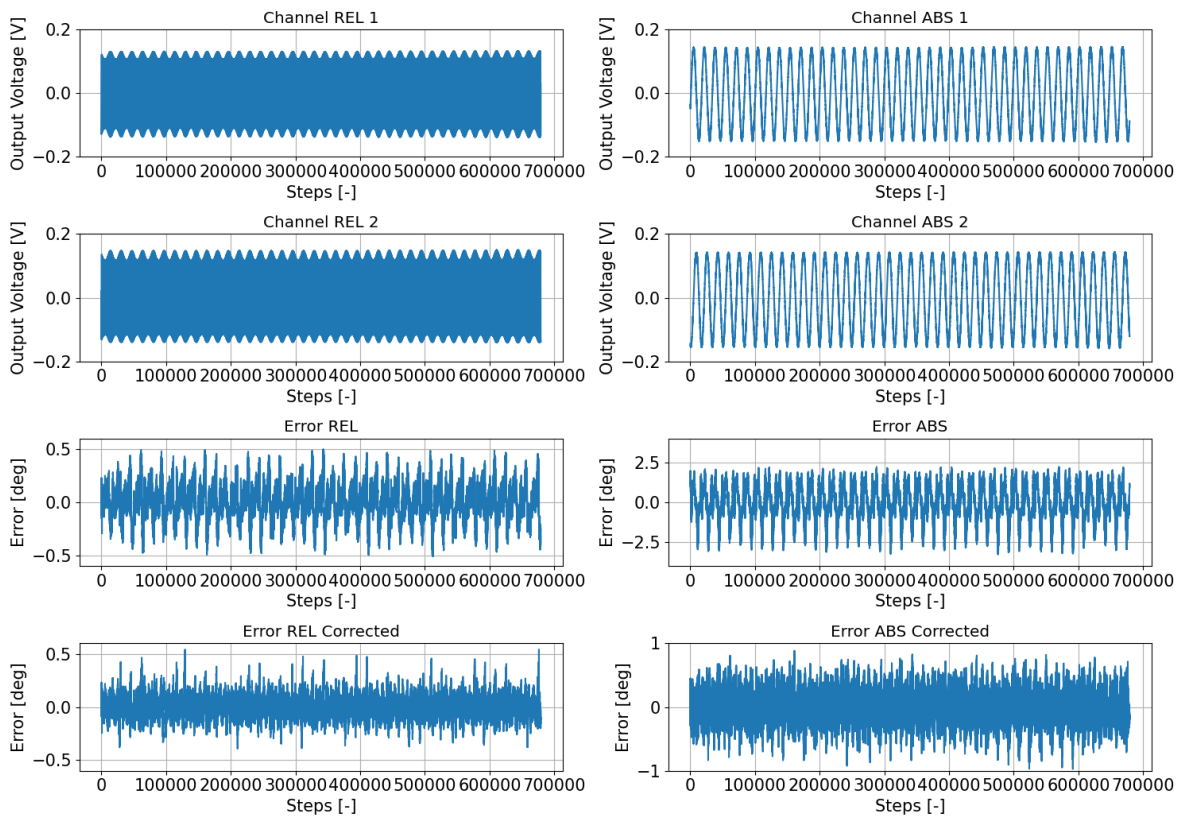
Figure 6.8: Encoder run with optimised settings.

Statistical analysis of the final results is presented in Figure 6.9. From this analysis, it can be concluded that the error of the relative component has a one-sigma deviation of 0.101 °and the absolute component has a one-sigma deviation of 0.195 °.
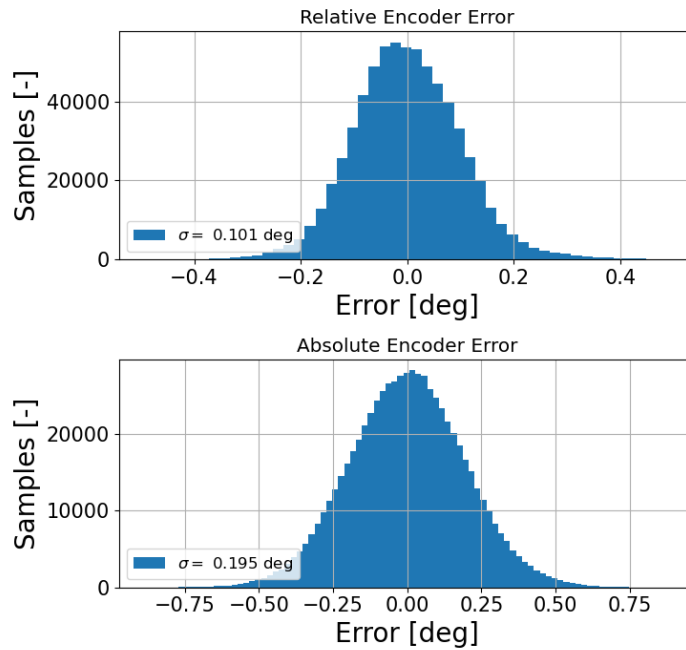
Figure 6.9: Error histogram for the relative and absolute encoder components

The original requirement HT_ENC_01 asked for a 0.087 °error in order to reach 12-bit. This accuracy was *nearly* met. The question is what kind of improvements can be made to the design of the encoder to finally meet the accuracy requirement. This will be treated in Section 7.2.1.

6.6. RQ5: What is the resulting improvement of state estimation?

This chapter has tested the prototype developed for the reaction wheel encoder. The testing was performed utilising a stepper motor, stepping the encoder through a series of positions. The result from this testing places the accuracy of the encoder at $0.101°$. Compared to the previous method of state estimation utilising hall sensors (which yields results every 30°) this is a performance improvement of a factor 300.

7

Conclusions, Discussion & Recommendations

The purpose of this chapter is to conclude the work performed in this thesis, discuss the results and make recommendations for future work. Section 7.1 will conclude the report by answering the five research questions, concluding in answering the main research question. Continuing from this conclusion, Section 7.2 will discuss the results of the research and suggest potential improvements. Finally, Section 7.3 will present a series of recommendations for future research/work to be performed based on the results of this thesis.

7.1. Conclusions

In this thesis a functioning design for sensor feedback for reaction wheels was developed, which can be used for the improvement of reaction wheel performance. This conclusion is separated into five components by answering all of the research questions postulated in Section 1.2.

In Chapter 2 a brief background on electric motors was given, concluding two main factors that that influence reaction wheel performance: commutation torque ripple and low-velocity operation. From this chapter it was concluded that a reduction in commutation torque ripple and improved low-velocity operation can be achieved through the implementation of sensor feedback. Increasing the positional awareness of the rotor will allow for the implementation of more complex control algorithms such as field-oriented control, which depend on a known rotor position. Low-velocity operation is improved due to the fact that external sensor feedback is independent of reaction wheel velocity, allowing for the controller to always have up-to-date knowledge of the rotor position. Furthermore it was highlighted why sensor feedback is an improvement over other sensor-less methods of state estimation. With this **RQ1** and **RQ2** were answered.

Chapter 3 presented a series of requirements set by Hyperion Technologies, followed by a trade-off between the various methods of sensor feedback that exist for electrical motors. The conclusion from this research was that capacitive sensing provides the best trade-off between accuracy, update frequency, power cycle tolerance and space environment tolerance. This answered **RQ3**.

Chapter 4 presented a design for a capacitive sensing amplifier that is suitable for use in the RW400 reaction wheel of Hyperion Technologies. The encoder design presented here consists of an absolute position component, combined with a relative component for higher accuracy and greater tolerance to external disturbances. Mechanically the design consists of two PCBs, one attached to the reaction wheel housing (stator) and the other to the reaction wheel rotor. Electrically, each of the two components consists of the diagram presented in Figure 4.4.

The varying parallel plate capacitor's capacitance is converted to an analog output signal through injection of an excitation signal, differentially amplified and demodulated using AM demodulation techniques.

The design for this parallel plate capacitor and components have been optimised for the given size of the reaction wheel and available components. This answered **RQ4**.

A prototype of this encoder was built in two stages, the design of these is presented in Chapter 5. The final prototype was used to verify the design in Chapter 6. Resulting from this testing is a capacitive sensing encoder with a (1σ) accuracy of $0.101°$. This performance is close to the desired performance, but unfortunately barely fails to meet the requirements. This state estimation however is still an improvement over the accuracy of the old method utilising just hall effect sensors, which only updated the position of the reaction wheel every $30°$. This finally answers **RQ5**.

Concluding, the main research question can now be answered:

> **MQ**: How can reaction wheel state estimation be improved in order to improve reaction wheel performance?

Reaction wheel state estimation can be improved through the implementation of a capacitive sensing amplifier fit for RW400 reaction wheels. This will improve reaction wheel performance by providing the controller with better state knowledge of the rotor. This research has presented a design for such a capacitive sensing amplifier which has the potential of meeting the requirements set by Hyperion Technologies. The current prototype will require further development and testing, but is shown to be functional and improve the state estimation of the rotor by a factor of 300.

7.2. Discussion

Chapter 6 has presented provided test results of the encoder prototype. Based on these test results it can be concluded that the design of the prototype is close to the requirements set out by Hyperion Technologies, however currently fails to meet them. The purpose of this section is to discuss the test results, link them back to the requirements and evaluate whether the goals set out by this research were met. This section is constructed from the perspective of each of the requirements, some of the will be discussed briefly, others in length.

Following this discussion on the requirements, three more topics are discussed that are required to evaluate the validity of the work performed. First, a discussion on the relative component and its necessity is presented, followed up by a discusson on integrating the design into the RW400 reaction wheel. Finally, this section is wrapped up with a discussion on the topic of differential amplifier topologies vs single ended amplifier topologies.

7.2.1. HT_ENC_01: Accuracy

The accuracy requirement set out in collaboration with Hyperion Technologies was not met. The current design has an accuracy of $0.101°(1\sigma)$, whilst the requirement asked for $0.087°(1\sigma)$. In order to account for any non-linearities, quantisation noise and other measurement errors, this requirement had an engineering margin of 2-bit. Due to the fact that the final design to be implemented on the reaction wheel has not yet been developed, it is not possible to make a verdict on whether the current design is sufficient for the RW400 reaction wheel. However, given that the test setup made use of some form of analog-to-digital conversion, one *can* conclude that currently the encoder *is* capable of providing high accuracy position feedback of the reaction wheel rotor.

Given that this requirement cannot be ticked off as met, this section will discuss some improvements which can be made to the design of the encoder based on observations made. Below some of the parameters influencing encoder performance are discussed, along with potential sources of improvement.

Noise coupling
Section 4.6 highlighted that in the design of the amplifier circuitry external noise sources will need to be taken into account. In order to determine whether noise is introduced into the system from an external source, a sample was taken of the output of one of the differential amplifiers (before AM demodulation). This sample can be seen in Figure 7.1. The major contributor to this noise is the stepper motor itself,

it is driven with sharp signals at high (12V) voltages. By touching the stepper motor with a ground wire the noise on the output can be visibly affected, meaning it has an influence on the encoder accuracy.
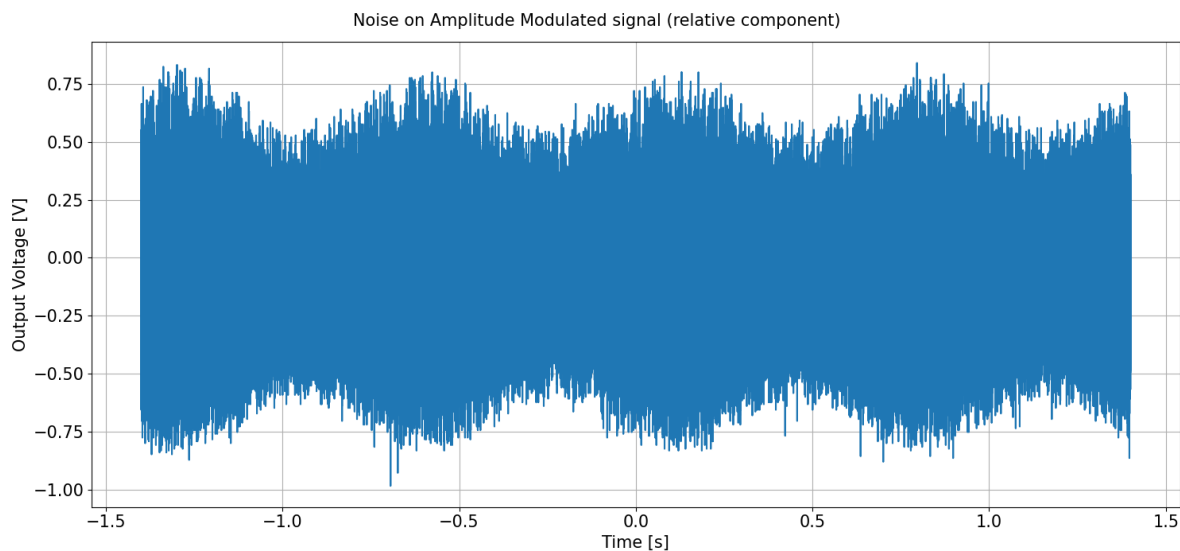
Figure 7.1: Noise in relative output channel

Mitigation of this noise is possible through ensuring that the rotor is properly grounded to the stator. Whilst this is difficult to achieve, it is possible, for example through the utilisation of a conducting lubricant and/or metallic bearings. Another method of ensuring that the impact of coupling in noise is minimal is by implementing a band-pass filter in-between the capacitive sensing amplifier and the AM demodulation. This will filter out any higher/lower frequency noise, increasing system performance.

Modulation depth reduction
The output shown in Figure 7.1 demonstrates that the modulation depth of the encoder is not near 100%, as one would expect based on the ideal model (See Section 4.8). The source of this can be traced back to crosstalk/fringe effects. Even when the rotor PCB is completely omitted, part of the signal can still be measured on the input of the capacitive sensing amplifiers, meaning that there is an alternate path for the signal to take, not present in Figure 4.11. By increasing the modulation depth of the signal a higher SNR can be achieved, which would increase the accuracy of the encoder.

Mitigation of this reduction in modulation depth is possible through the placement of a 'guard rail' at ground potential in between the excitation electrode and sensitive electrodes on the stator. This will reduce the amount of signal that passes sideways through the pcb, increasing modulation depth. One other factor that can contribute to a reduction in modulation depth is fringe capacitance. This was assumed to be negligible in Section 4.3, however based on the results this assumption will require further studying. This can be done through utilisation of electric field simulators such as for example ANSYS.

Signal rounding
When comparing the output of the encoder to the ideal case (see Figure 6.7) one can see distortion of the output signal in the form of rounding of one side of the curve. This effect causes a loss of information on the output, reducing the accuracy of the encoder. This effect was also observed in Section 4.8, however in section 6.4.1 it was elaborated that this effect must be an amplifier limit because otherwise it would not depend on the input voltage.

The cause for this effect requires further investigation, but two potential sources are the slew rate limit and the output current limit. The data in Figure 7.1 was taken with an excitation amplitude of 3.5V. The output of the amplifier slews from the maximum (0.75V) to the minimum (-0.75V) in $2\mu s$ (half the period), making the slew rate $\frac{0.75 - -0.75}{(1/250)/2} = 0.75 V/\mu s$. The amplifier specifies the limit of the slew rate as $2V/\mu s$. While there is some margin here, with a higher excitation amplitude one approaches this limit.

Furthermore, the datasheet [25, p.9] specifies that the gain of the amplifier at high output capacitances suffers greatly at 250 kHz. These factors combined could mean the encoder is operating near its limits when it comes to driving the output.

Mitigating this requires further tuning the design of the encoder in such a way that that the output impedance of the amplifier increases. The reason the current design is the way it is is due to the limitations on available components for the pi filter (for a smaller C one would require a larger L). If a more complex filtering topology were implemented, or a buffer amplifier is used it is possible that the encoder output improves.

Output Distortion

In the test results presented in Chapter 6, the output of the encoder is not the same as expected based on the ideal model created in Chapter 4. Most notable, the gain of the relative component seems to vary over a single rotation, causing the output to "wobble". Section 4.8 demonstrated the sensitivities of the system to various misalignments. One of the observed effects here was a change in relative gain over a single rotation. This was caused under two simulation circumstances: variation in electrode gap and a radial offset between the rotor and stator center of rotation.

In order to determine the influence of an offset on the system, a large rotor-rotor offset was artificially created (by sliding the rotor pcb on the rotor) and compared to a 'zero-ed' measurement. The results are plotted in Figure 7.2. The results of this test are plotted in Table 7.1. From this test one can observe two effects:

1. The distortion is more complex than a simple sinusoidal pattern
2. The accuracy of the encoder is not greatly affected

Given that in reality the offsets provided in Section 4.8 probably do not occur each on their own, but more likely a combination of them will present themselves it is likely that Figure 7.2 represents a complex case where multiple effects are occuring at once. One of the more interesting cases of this effect can be seen in Appendix A, where an older less accurate test setup was used and multiple hand-placed wheels were compared. The distortion on the relative output is visible in this case, but here it was proven to be irrespective of different orientations of the rotor PCB (rotationally speaking). Thus from this test it is concluded that variation in electrode gap must be one of the factors affecting the measurements.

In conclusion, by investigating the above sources further and improving the design, it is no unforeseeable that the accuracy target can still be met. In Section 7.3.1 a path forward for increasing the accuracy of the encoder is presented.
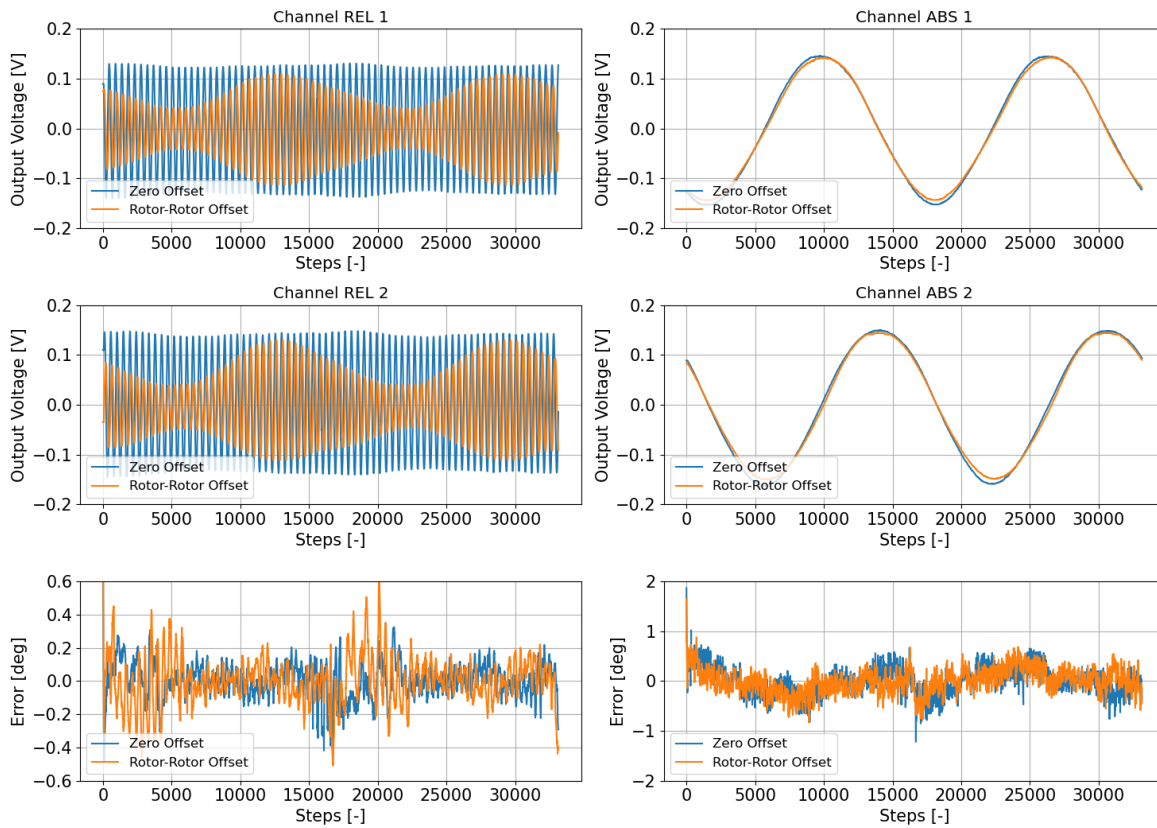
Figure 7.2: Rotor-Rotor Offset vs Nominal

Label	Excitation Freq.		Excitation Amp.		Phase Shift		Relative Error STD		Absolute Error STD	
Zero Offset	250	kHz	3.5	V	30	deg	0.111	deg	0.279	deg
Rotor-Rotor Offset	250	kHz	3.5	V	30	deg	0.145	deg	0.249	deg

Table 7.1: Comparison between a nominal measurement and a measurement with a large rotor-rotor offset

7.2.2. HT_ENC_02: Update Frequency

Due to the nature of the measurement setup utilising a slow USB connection it is not possible to currently measure the position of the reaction wheel quickly. This can, in the future be solved through the utilisation of analog-to-digital ICs. Due to the fact that 12-bits of resolution are required this can be performed through the built-in ADC of a microcontroller, which can sample up to 300,000 samples per second

The research to be performed in order to verify this requirement also contains an investigation into the noise bandwidth of the encoder output. In the previous section it was already elaborated that there is noise introduced into the encoder, part of which will be filtered by the output filter, however some of it might affect performance. In the current test setup a large amount of samples are taken over a longer period of time. If the encoder has to operate at higher speeds, more of the higher frequency noise on the measurement might be introduced into the encoder output, affecting performance.

Section 7.3.2 will provide a path forward for verifying this requirement.

7.2.3. HT_ENC_03: Output Signal

The current output signal is in the form of an analog value. By utilising a microcontroller solution, as mentioned in the previous section, any digital output format can be configured. In this microcontroller, the methods for readout and bias correction presented in Section 6.3 will need to be integrated. The corrections presented in Section 6.3 are proven to be consistent over many runs of the encoder but

vary each time the prototype is reassembled. Given that a reaction wheel will only be assembled once and is much more rigid than the prototype, it should be possible to predetermine these corrections and store them in the form of a LUT or parameters for a polynomial fit which can be calculated in real time on the final system.

7.2.4. HT_ENC_04: Power Cycle Tolerant
This requirement is inherently met through the design of the encoder itself. The encoder is fully analog and is designed to provide an absolute position reference. These factors combined mean that aside from a short startup time, the output of the encoder is power cycle tolerant.

7.2.5. HT_ENC_05: Space Components
The design currently makes use of untested components. Hyperion Technologies can provide a list of components that will work in a space environment, however dual amplifiers do not seem to be in this list. In order to determine whether the current design of the encoder is space-worthy a radiation test campaign will be required where the performance of the encoder is monitored whilst the components are tested. This radiation test campaign is unfortunately not part of the scope of this thesis and will need to be conducted as future work.

7.2.6. Omitting the relative component
In the results found in Section 6.8 it is visible that the relative component has an accuracy of 0.101 °, which is not much greater than the accuracy of the absolute component (0.195 °). Thus a logical question to ask is whether the relative component even adds a great deal of accuracy to the system. Omitting the relative component would yield an increase in the SNR of the absolute component because more of the input signal makes it through to the amplifier (through an increase of C_0 and C_s). Hence a discussion is warranted.

Given that this subject will require further research and testing, a list of pros and cons are presented below, however no final conclusion can be drawn.

Pros

1. **Increased SNR due to larger areas**
   When the relative component is removed a larger area is available for the absolute sensing electrode and excitation electrode.

2. **Reduced component count**
   By removing one of the two encoder wheels, the amount of components gets cut in half.

3. **Simplified sensing algorithm**
   In the current design the absolute and relative components are sampled simultaneously and absolute component will be used to quantify in 'which' of the relative waves the relative signal is located, further increasing the accuracy of the original absolute measurement. By removing the relative signal (under the constraint that this actually increased the absolute encoder accuracy) this process can be simplified.

Cons

1. **Increased noise susceptibility**
   In the design of the encoder the susceptibility of noise coupling from external sources in the encoder was discussed and mitigated through the use of the relative component. This component averages many smaller areas around the circle, vs a large chunk in the middle of the absolute encoder. This averaging effect would be removed if the relative component is removed.

2. **Increased susceptibility to offsets**
   In Section 4.8 some of the mechanisms impacting encoder performance due to shape changes

were presented. Most of these offsets can be counteracted through the compensation mecha-
nisms discussed in this report, however some of them can not. For example the rotor-rotor PCB
misalignment shown in Figure 4.37, where one of the encoder channels has the same output for
two different positions.

7.2.7. Integration into a reaction wheel

The current design has the correct dimensions to be fitted onto an RW400 reaction wheel, but not
without creating the next generation of RW400 reaction with a taller housing and reworked/more inte-
grated electronics. The next generation of reaction wheels is currently under development at Hyperion
Technologies and integration of the encoder into the reaction wheel will be one of the options that are
considered. However before this step is taken, a second prototype will need to be made which can be
retrofitted to a prototype RW400 such that development can begin. Section 7.3.3 will cover this subject
further.

7.2.8. Differential vs Single Ended Amplifiers

In Section 4.4 a model for the encoder was presented. This model made use of a single-ended ampli-
fier topology, whilst in reality a differential amplifier topology was used. Reasons behind this decision
are two-fold. Both reasons will be discussed below.

Modelling a single-ended circuit is simpler. In Section 7.2.8 the main purpose was to develop a model
for trading off different amplifier *topologies* and perform an analysis into the noise generated by these
topologies to determine whether the concept was feasible. Whilst it is possible to model differential
amplifiers, it proved to be difficult within the time-frame of this thesis. Given that Figure 4.23 proves
that the signal level of the amplifier stays well clear of the noise floor of the amplification circuits, the
risk of such a design change can be considered mitigated. The design was not 'on the edge'.

Given that the design of the circuit was such that subtraction was always part of the design, a differen-
tial amplifier is a natural fit, in fact, utilising differential amplifiers yields a 50% reduction in the number
of components, simplifying the design.

The reaction wheel is a noisy environment where noise coupled in from the electric motors and the rest
of the ADCS, will affect encoder performance. However, many of these disturbances, along with Power
Supply (PSU) noise will affect the encoder in the form of common-mode noise. Differential amplifiers
have a higher noise immunity to common-mode noise sources versus single-ended topologies due
to the fact that any common factors are 'subtracted' out[23] at the input, and do not affect the output
(See Figure 7.3). Therefore utilising a differential amplifier topology is considered an improvement over
separate single-ended amplifiers.
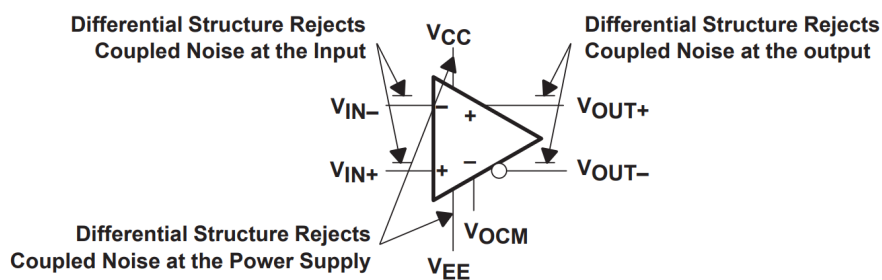
Figure 7.3: Full-Differential Amplifier Noise Immunity [23]

7.3. Recommendations

Based on the conclusions and the discussion, improvements and optimisations can be made to the current encoder design. The purpose of this section is to provide a path forward to verify the remaining three requirements, improve the design, and finally validate the concept.

7.3.1. Increasing Accuracy

Section 7.2.1 has discussed the subject of encoder accuracy and highlighted some of the flaws of the current design, reasoning why HT_ENC_01 is not met. In order to improve the design, a guard rail can be added, the (intermediate) filtering can be improved, as well as making sure that the filter design matches the specifications of the differential amplifier better. The first step in improving the filters would be to take the filter requirements presented in Section 4.7 and the specifications of the LTC1992[25] and trade-off various filter topologies based on a set of to be determined criteria.

7.3.2. Testing at higher wheel velocities

The current test setup, as described before relies on a slow sampling device over USB to obtain the output of the encoder, meaning compliance with requirement HT_ENC_2 cannot be verified. The encoder accuracy has been determined at these low speeds, however in practice, the reaction wheel will rotate up to 5000 rpm. In order to test the encoder at higher wheel velocities a faster sampling method will need to be created. Section 7.2.3 has already mentioned that some kind of microcontroller solution can be implemented. In an initial development phase, the current prototype can be used, in combination with a microcontroller development kit. To present a path forward, the following things will need to be considered:

1. **Utilise short and shielded wires**
   The environment surrounding a motor is noisy, if unshielded wires are used, the signal to noise ratio of the output signal is degraded after it leaves the encoder. By utilising properly shielded wires and keeping the wires as short as possible, this effect is minimised.
2. **Properly configure the ADC**
   Analog to Digital converters have various reference inputs with which incoming signals are compared. In order to ensure that the effects of quantisation errors/noise are minimised, the selected references will need to be optimised for the incoming encoder signals. For example, ABS Channel 1 in Figure 6.8 is biased around 2.5V and varies by ±0.175 V. Ideally, the ADC range is tuned to exactly this range.

3. **Install a reference encoder**
   The current test setup is based upon the utilisation of a stepper motor with known, fixed step sizes, which allows a *sample-step-sample* cycle to be run where the difference between the samples is always known. When spinning the wheel at higher speeds one cannot do this any more. Thus, in order to determine the encoder performance at higher velocities, a second, commercially available encoder will need to be used to serve as a reference.

7.3.3. Integrate Design

The current design does not comply with requirement HT_ENC_3. It utilises analog output signals, which aid in testing, but cannot be used as input for the RW400 controller. In order to verify this requirement, and further validate the concept, an integrated design will need to be developed. This design will need to incorporate both signal generation and sampling onto the stator PCB. The following steps will need to be performed to produce a first prototype which will fit within the dimensions and comply with all requirements:

1. Develop signal generation circuitry
2. Develop signal acquisition circuitry & write post-processing software
3. Strip the current design from all debug connections
4. Fit the design within 50 x 50 mm
5. Modify the RW400 top lid to allow for integration of the encoder PCBs

Signal Generation
Currently, the test setup makes use of a bench-top signal generator to generate the excitation and de-

modulation signals. In order to integrate this solution more tightly another method of signal generation will need to be developed. Two options are to be considered:

1. Generating square waves using a microcontroller
2. Generating two signals with a controllable phase shift using Direct Digital Synthesis (DDS)

The advantage of option 1 is its simplicity, microcontrollers are setup to generate square waves through internal systems such as Atmel's Wex timer counter extensions. This will allow for the generation of two square waves with a known offset, one of which can be filtered into a pure sine wave. The disadvantage is the requirement of this filter, which will need to be designed carefully as to provide an as pure sine wave as possible.

Second, a separate Integrated Circuit (IC) can be utilised that can do DDS. DDS is a method of generating arbitrary signals in an integrated circuit. The advantage is the level of control over the output signal, the ICs are made to perform specifically this function. The downside is that it is more difficult to align the two signals with one another and have phase shift control. That, however can be solved by utilising the clock output of one of the ICs as the input of the next, such as demonstrated by [26].

Signal Acquisition
Section 7.3.2 has already laid out a path for integration of signal acquisition utilising a microcontroller. Once this functions with an external development board, this design can be modified to function on the stator PCB and as such, integrate the design.

Remove debug connections
To allow for easy access during testing, the current design contains large through-hole connections for both the power input, in the form of 2.54 mm pin headers, as well as the output, in the form of SMA and UFL connections. If the design becomes fully integrated, all these components can be removed and/or reduced to a smaller sized interface.

Fit the design within 50x50mm
The current sensing circuitry of the absolute component already fits within these constraints, however for debugging purposes the relative component sensing is currently located on the outside of the wheel. Based on the image in Figure 5.3 however, one can deduce that there is space within the middle section of the PCB to allow for full integration of all sensing circuitry.

Modify the RW400 lid
Currently, the top side of the RW400 contains a solid lid, which perfectly aligns with the reaction wheel rotor and provides one of the anchor points for the reaction wheel shaft. In the fully integrated design, this lid will need to be modified to house all the sensing electronics.

7.3.4. Component Testing
The components utilised in the current design have not been tested for the space environment, meaning HT_ENC_05 cannot be verified. During the design, space worthiness was taken into account (for example by not selecting LEDs), however the radiation performance of the selected components is unknown. Table 7.2 contains the operating temperature conditions of the active components in the circuit, which show that temperature wise at least, the components are sufficient to operate within the constraints of a satellite. In order to determine whether the radiation specifications are also met, a radiation test campaign will need to be set up by Hyperion Technologies.

Component	Min. Temp [°C]	Max. Temp [°C]
LTC1922	-40	125
771-74LVC1G3157GVQ10	-40	125

Table 7.2: Temperature range of used active components

7.3.5. Validation

The research presented in this thesis has mostly focussed on the development of state estimation for RW400 reaction wheels. The reasoning behind requiring this state estimation was based on previous research performed at Hyperion and presented in Chapter 2. Once the design of the encoder has been completed, the next step in the process is to validate this reasoning and determine whether improved low-speed performance and reduction in torque ripple are actually achieved. Once an integrated, functioning design (with new control algorithm) has been completed, the following steps will need to be taken to validate the new RW400 design:

1. **Perform vibration measurements**
   Figure 1.1 contained a series of measurements of the RW400 reaction wheel Z axis vibrations for a constant acceleration ramp. This same testing will need to be performed once again, to confirm the reduction in torque ripple.

2. **Generate torque box**
   Figure 1.2 presented the torque box (maximum available reaction wheel torque at a given velocity/momentum) for a similar reaction wheel to the RW400. In order determine whether the low-velocity characteristics of the reaction wheel have improved, a similar diagram can be made for the RW400 pre- and post encoder. The contents of this diagram will demonstrate whether the performance at low velocities has improved.

With these recommendations the work presented in this thesis is concluded. The path forward has been presented and Hyperion Technologies has been provided with a baseline prototype to be used for future development of their RW400 line of reaction wheels.

A
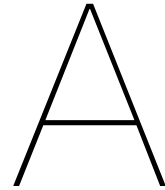
Test Setup Repeatability

In Chapter 6 the repeatability of the test setup was drawn into question. In order to counteract for any offsets and/or biases in the test setup a characterisation was performed and corrected. However this does not mean that it is not desirable to know the effect of encoder bias vs test setup bias. That is what will be covered in this appendix.

During earlier testing performed a different test setup was utilised. This test setup used a low cost 28BYJ-48 stepper motor, which is normally used for air-conditioning unit's air spreaders. The stepping accuracy of this motor was much less than the NEMA17 eventually used, but does provide valuable insight when it comes to splitting encoder and test setup accuracy.

During characterisation of this test setup five different rotor PCBs were manually (by hand) placed on the metal rotor, without moving it. The result of five runs can be seen in Figure A.1.
Based on these results the following observations can be made:

1. **Backlash**
   There is backlash in the system, evident by the jumps in Error at the beginning of the test run. Due to the fact that backlash is a real effect visible in any geared system this is not a problem. In fact, it highlights the ability of the encoder to detect small positional changes.

2. **Independence of wheel position**
   Because the wheels are placed manually onto the rotor, they are not placed in the exact same manner each time. This is confirmed by the relative components in the first two plots not overlapping, but having phase offsets. Nonetheless the error in the system is correlated with position, pointing at test-setup introduced biases.

3. **Independence of rotor PCB**
   Five different rotor PCBs were used. The offset followed the same pattern for all of them. This rules out any specific manufacturing problems with a single pcb.

Due to these results it can be assumed that a great deal of the offsets measured in the encoder stem from the test setup and not the encoder itself. In reality the reaction wheel will also not be perfect, but by proving it can be compensated for through software the real performance of the encoder itself is presented.
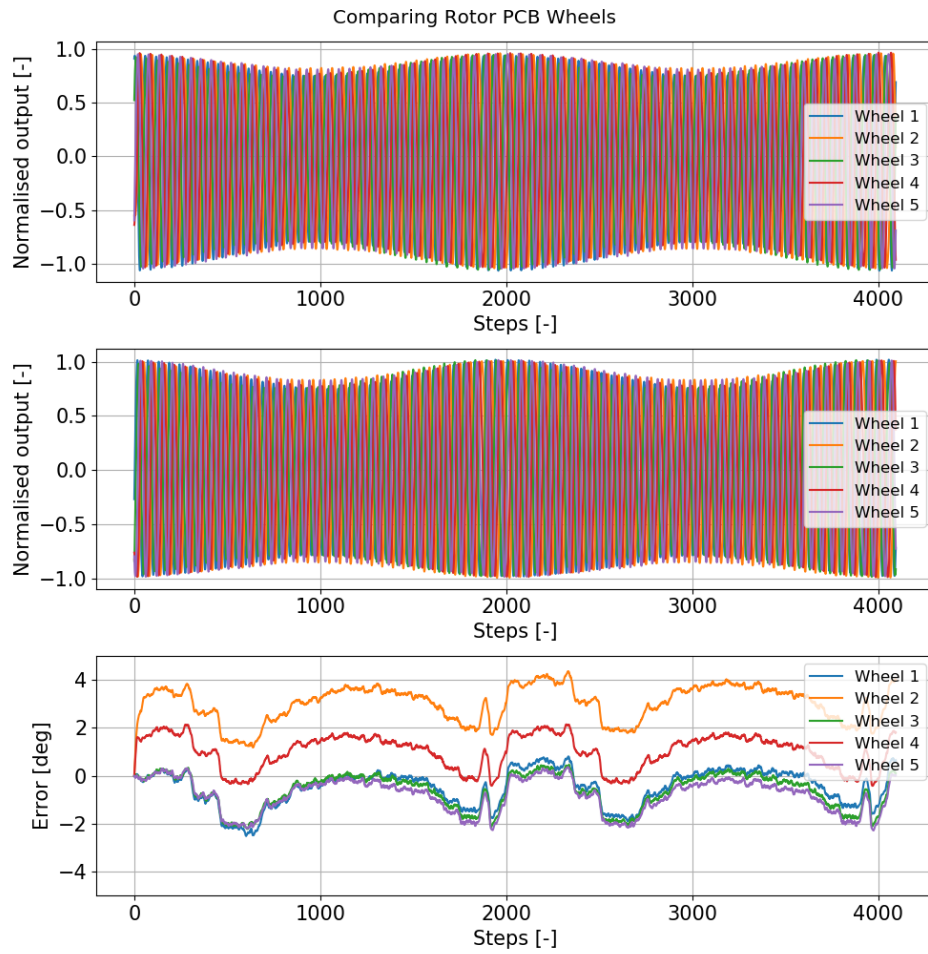
Figure A.1: Comparing five wheels placed in a random location on the test rotor (two rotations each)

Bibliography

[1] Anaheim Automation. Encoder Guide, 2019. URL `https://www.anaheimautomation.com/manuals/forms/encoder-guide.php`.

[2] Steve Arar. Synchronous Demodulation Using Analog Multipliers vs. Switch-based Multipliers, 2020. URL `https://www.allaboutcircuits.com/technical-articles/synchronous-demodulation-analog-multiplier\-switch-based-multiplier-sinusoid-or-square-wave/`.

[3] ATMEL. AVR447 - Sinusoidal driving of three-phase permanent magnet motor using ATmega48/88/168 Features. pages 1–26, 2006.

[4] David S. Bayard. High-Precision Three-Axis Pointing and Control. *Encyclopedia of Aerospace Engineering*, (November), 2010. doi: 10.1002/9780470686652.eae300.

[5] Manuele Bertoluzzo, Giuseppe Buja, Ritesh Kumar Keshri, and Roberto Menis. Sinusoidal Versus Square-Wave Current Supply of PM Brushless DC Drives: A Convenience Analysis. *IEEE Transactions on Industrial Electronics*, 62(12):7339–7349, 2015. ISSN 02780046. doi: 10.1109/TIE.2015.2455518.

[6] Bruce Carter and Ron Mancini. *Op Amps for Everyone*. 5 edition, 2003. ISBN 9780750677011. doi: 10.1016/B978-0-7506-7701-1.X5000-7.

[7] Celera Motion. How does a capacitive encoder work?, 2022. URL `https://www.celeramotion.com/zettlex/how-does-a-capacitive-encoder-work/`.

[8] Xu Chen, Zhe Zhang, Shengbao Yu, and Tiberiu Gabriel Zsurzsan. Fringing Effect Analysis of Parallel Plate Capacitors for Capacitive Power Transfer Application. *2019 IEEE 4th International Future Energy Electronics Conference, IFEEC 2019*, 2019. doi: 10.1109/IFEEC47410.2019.9015111.

[9] Danielle Collins. What are capacitive encoders and where are they suitable?, 2015. URL `https://www.motioncontroltips.com/faq-what-are-capacitive-encoders-and-where-are-they-suitable/`.

[10] Copley Controls Corp. What is 'Field Oriented Control' and what good is it? URL `https://actronic-solutions.de/files/actronic/FTPROOT/Field-Oriented-Control.pdf`.

[11] Cypress. Coordinate Transform in Motor Control. (002):1–12, 2016.

[12] Subir Das, Tuhin Subhra Sarkar, and Badal Chakraborty. Simple approach to design a capacitive rotary encoder. *IET Science, Measurement and Technology*, 12(4):500–506, 2018. ISSN 17518822. doi: 10.1049/iet-smt.2017.0376.

[13] Mathieu Boutillier Dct. Protons effects on commercial european light emitting diodes. pages 9–10, 2015.

[14] DesignSpark. Different types of motors and their use, 2016. URL `https://www.rs-online.com/designspark/different-types-of-motors-and-their-use`.

[15] Dynamics Research Corp. Techniques For Digitizing Rotary and Linear Motion. pages 10–11, 1980.

[16] ECSS. ECSS-E-HH-32-26A, Spacecraft mechanical loads analysis handbook. *ESA Requirements and Standards Division*, (February):34–36, 2013.

[17] Radu Florea. *State Estimation for Nanosatellite-Class Reaction Wheels*. Master thesis, Delft University of Technology, 2018.

[18] José Carlos Gamazo-Real, Ernesto Vázquez-Sánchez, and Jaime Gómez-Gil. Position and speed control of brushless dc motors using sensorless techniques and application trends. *Sensors*, 10 (7):6901–6947, 2010. ISSN 14248220. doi: 10.3390/s100706901.

[19] Paul R. Gray. *Analysis and Design of Analog Integrated Circuits*. Wiley Publishing, 4th edition, 2009. ISBN 0470245999.

[20] Bo Hou, Chao Li, Zhenyi Gao, Qi Wei, Bin Zhou, and Rong Zhang. Design, optimization, and compensation of a high-precision single-excitation absolute capacitance angular encoder up to 4". *IEEE Transactions on Industrial Electronics*, 66(10):8161–8171, 2019. ISSN 15579948. doi: 10.1109/TIE.2018.2886762.

[21] V Hutson. The circular plate condenser at small separations. *Mathematical Proceedings of the Cambridge Philosophical Society*, 59:211–224, 1963. doi: 10.1017/S0305004100002152.

[22] JLCPCB. JLCPCB Capabilities, may 2022. URL `https://jlcpcb.com/capabilities/Capabilities`.

[23] James Karki. Fully-Differential Amplifiers. Technical report, 2016.

[24] Erik Kulu. Nanosatellite and CubeSat Database, aug 2021. URL `https://www.nanosats.eu/`.

[25] Linear Technology Corporation. LTC1992 Family - Low Power, Fully Differential Input/Output Amplifier/Driver Family. Technical report, 2011. URL `http://www.linear.com/leadfree/`.

[26] Chris Lott. LOW-COST, TWO-CHANNEL SCRIPTABLE WAVEFORM GENERATOR, mar 2022. URL `https://hackaday.com/2022/03/05/low-cost-two-channel-scriptable-waveform-generator/`.

[27] Tom McInally. *The Sixth Scottish University: The scots colleges Abroad: 1575 to 1799*, volume 24. Leiden, 2012. ISBN 9789004214262.

[28] Microchip. Sensorless Field Oriented Control (FOC) for Permanent Magnet Synchronous Motors (PMSM) Welcome to the Sensorless Field Oriented Control for Permanent Magnet Synchronous Motors web seminar. Technical report, 2007.

[29] Youhei Miyaoka, ; Minoru, and Kuribayashi Kurosawa. Measurement of Current Noise and Distortion in Resistors. (September):3120–3125, 2019.

[30] Giovanna Monari. Understanding Resolution In Optical And Magnetic Encoders, 2013. URL `https://www.electronicdesign.com/technologies/components/article/21798142/understanding-resolution-in-optical-and-magnetic-encoders`.

[31] Anton J.M. Montagne. *Electronics Amplifier Design 1*. 2015.

[32] Rajesh Nalli, K Subbarao, M Ramamoorthy, and M Kiran. Sensorless Control of BLDC Motor using Flux Linkage Based Algorithm. *International Journal of Engineering and Advanced Technology*, 8 (6):1549–1556, 2019. doi: 10.35940/ijeat.f8158.088619.

[33] R Nave. Commutator and Brushes on DC Motor - HyperPhysics (Web Page), 2020. URL `http://hyperphysics.phy-astr.gsu.edu/hbase/magnetic/comtat.html`.

[34] Le Minh Phu'ó'c. *Micro-disturbances in Reaction Wheels*. Phd thesis, TU Eindhoven, 2017.

[35] Art Pini. *How to Use Rotary Encoders to Quickly Convert Mechanical Rotation into Digital Signals*. PhD thesis. URL `https://www.digikey.nl/en/articles/techzone/2018/dec/how-to-use-rotary-encoders-convert-mechanical-rotation-digital-signals`.

[36] Paresh Sen. *Principles of Electric Machines and Power Electronics*. 2014. ISBN 9788578110796. doi: 10.1017/CBO9781107415324.004.

[37] Sinclair Interplanetary. Microsatellite Reaction Wheels (RW3-1.0), 2017.

[38] G Sloggett, N Barton, and Steven Spencer. Fringing fields in disc capacitors. *Journal of Physics A: Mathematical and General*, 19:2725, 1999. doi: 10.1088/0305-4470/19/14/012.

[39] Jeff Smoot. Capacitive, Magnetic, and Optical Encoders – Comparing the Technologies, 2020. URL https://www.cuidevices.com/blog/capacitive-magnetic-and-optical-encoders-comparing-the-technologies.

[40] Neil Storey. *Electronics: A Systems Approach Sixth Edition*. 2017. ISBN 9781292114064.

[41] Martin Sumega, Šimon Zoššák, Patrik Varecha, and Pavol Rafajdus. Sources of torque ripple and their influence in BLDC motor drives. *Transportation Research Procedia*, 40:519–526, 2019. ISSN 23521465. doi: 10.1016/j.trpro.2019.07.075. URL https://doi.org/10.1016/j.trpro.2019.07.075.

[42] Texas Instruments. THS413x High-Speed, Low-Noise, Fully-Differential I/O Amplifiers. Technical report, 2015. URL www.ti.com.

[43] Paridhi Wadhani and Shivam Joshi. Trapezoidal & Sinusoidal: Two BLDC Motor Controls, 2021. URL https://www.bacancytechnology.com/blog/trapezoidal-and-sinusoidal-bldc-motors.

[44] Ian Williams and Art Kay. Noise - 8 TIPL 1318. Technical report.

[45] Chen Zhao, Marko Tanaskovic, and Federico Percacci. Sensorless position estimation for slotless surface mounted permanent magnet synchronous motors in full speed range. *Conference Proceedings - 2017 8th International Symposium on Sensorless Control for Electrical Drives, SLED 2017*, 34(12):193–198, 2017. ISSN 0885-8993. doi: 10.1109/SLED.2017.8078423.

[46] Dezhi Zheng, Shaobo Zhang, Shuai Wang, Chun Hu, and Xiaomeng Zhao. A capacitive rotary encoder based on quadrature modulation and demodulation. *IEEE Transactions on Instrumentation and Measurement*, 64(1):143–153, 2015. ISSN 00189456. doi: 10.1109/TIM.2014.2328456.